STABILITY OF NANOSTRUCTURED/AMORPHOUS ALUMINUM-MANGANESE ALLOYS

BY

TING-YUN SASHA HUANG

B.S. in Materials Science and Engineering
National Taiwan University, Taipei, Taiwan, 2011

SUBMITTED TO THE DEPARTMENT OF MATERIALS SCIENCE & ENGINEERING
IN PARTIAL FULFILLMENT OF THE REQUIREMENTS FOR THE DEGREE OF

DOCTOR OF PHILOSOPHY IN MATERIALS SCIENCE AND ENGINEERING
AT THE
MASSACHUSETTS INSTITUTE OF TECHNOLOGY

JUNE 2016

Signature of Author: _____

Ting-Yun Sasha Huang
Department of Materials Science and Engineering
May 16, 2016

Certified by: _____

Christopher A. Schuh
Department Head and Danae and Vasilis Salapatas Professor of Metallurgy
Thesis Supervisor

Accepted by: _____

Donald R. Sadoway
John F. Elliott Professor of Materials Chemistry
Chair, Departmental Committee on Graduate Students

ABSTRACT

Nanocrystalline alloys have attracted interest for decades because of their improved mechanical strength without sacrificing ductility, but structural stability has always been an issue. In this work, bulk aluminum-manganese (Al-Mn) nanocrystalline alloys have been synthesized using room temperature ionic liquid electrodeposition, by which various nanostructures and dual-phase structures can be created by controlling the Mn solute incorporation level. The manganese exhibits grain boundary segregation in the Al-Mn solid solution in the as-deposited condition, which contributes to enhanced stability of the nanostructure. The grain boundary properties of the nanostructured alloys were studied via three dimensional atom probe tomography and aberration-corrected scanning electron microscopy. The segregation energies were calculated based on the experimental results and compared with the values calculated from a thermodynamic-based segregation model. Upon heating of the nanostructured and dual-phase alloys, a variety of complex phase transformations occur. A combination of X-ray diffraction, transmission electron microscopy, as well as differential scanning calorimetry were employed to understand the phase transformation mechanisms and grain growth processes. A Johnson-Mehl-Avrami-Kolmogorov analytical model was proposed as a descriptive method to explain the phase transformation sequence. Using the parameters extracted from the analytical model, predictive time-temperature transformation diagrams were constructed. The stability region of the alloy in time-temperature space is thus established, providing a simple way to evaluate nanostructure stability.

ACKNOWLEDGMENTS

To begin with, I would like to thank the members of my thesis committee, Professor Silvija Gradecak and Professor Antoine Allanore, for their insightful comments and advice. I truly appreciate their time in evaluating my thesis work and their support and encouragements.

I would also like to appreciate the staff members of the MIT Center for Materials Science and Engineering (CMSE), especially Dr. Shiahn Chen, Dr. Yong Zhang, and Dr. Scott Speakman, are greatly acknowledge. Dr. Andrew Magyar, Mr. Adam Graham, and Prof. David Bell in Harvard University are acknowledged for their help in atom probe tomography. Especially Andrew, who has helped me a lot not only in the experiments, but also the sample preparation process. The discussion is invaluable and I cordially appreciate your help.

The past and current Schuh research group members have been very helpful and kind during my time in the group. I treasure every moment we have spent together. I especially want to thank Dr. Tongjai Chookajorn and Dr. Lin Li, who helped me a lot at the start of my Ph.D life both academically and non-academically, we have explored Boston together and those are the memories I will forever treasure. Dr. Hyon-Jee Voigt and Dr. Sam Cross have been tremendous help in simulation and data-fitting. Hyon-Jee has always looked after me to make sure I adapt well in MIT, encouraged me in difficult moments. Members of the MIT department of Materials Science and Engineering have also been really kind to me and I really appreciate your support through times (Thank you, Angelita, Elissa, Diane).

And of course, I would like to thank my advisor, Professor Chris Schuh for the invaluable training and advice in my Ph.D time at MIT. Chris has always been kind, positive, and always encourages me to do a better job. I have learned a lot from Chris not just in problem solving, but also in how to be a better person. Thank you again for your guidance and mentoring.

I appreciate the Warehouse community, where I spent my whole PhD life staying in. John and Anne, you guys are the best housemaster ever. It was nice to have a really supportive and warm community to live in for these 5 years.

I am grateful for the friendship I have made during my years at MIT. Yvonne Su, Pan-Yu Chen, Alina Rwei, Chris Lai, Tony Wu, Marcus Chuang, Wenting Xing, Kevin T. Chen, Shu-Heng Shao, Grace Gu, you guys have made life in Boston enjoyable, I enjoyed every minute we spent together. I would also like to thank those who are not in Boston but remotely support me in Taiwan, your encouragement and faith in me keep me moving forward. Special thanks to Yu-Hsin Chen, for the moments we share together, you are the best!

Last but not the least, thank you, Mom and Sis, without you guys, none of these could happen, you guys are my greatest supporters of all times.

CONTENTS

1 INTRODUCTION 21
1.1 Nanocrystalline and Amorphous Metals . . . 21
1.2 Aluminum-Manganese Alloy System . . . 22
1.2.1 Electrodeposition of the Al-Mn Alloy System . . . 24
1.3 Thermal Stability . . . 27
1.4 Problem Statement and Structure of Thesis . . . 29
2 THERMAL STABILITY OF NANOSTRUCTURED AL-MN ALLOYS 31
2.1 Basics of Al-Mn Nanostructured Alloys . . . 31
2.1.1 Materials Synthesis . . . 31
2.1.2 Materials Characterization . . . 33
2.1.3 Annealing Studies . . . 33
2.2 Grain Size with respect to Different Mn Concentration . . . 34
2.3 Microstructure Evolution . . . 35
2.4 Phase Transformation Kinetics . . . 37
2.4.1 Data Fitting Model . . . 39
2.4.2 Data Fitting Results . . . 42
2.4.3 Construction of a TTT Diagram . . . 44
2.5 Extended Annealing . . . 46
2.6 Conclusions . . . 47
3 NANOSTRUCTURE STABILIZATION MECHANISM 49
3.1 Grain Boundary Characterization . . . 49
3.2 Grain Boundary Structures . . . 50
3.2.1 Basic Characterization . . . 50
3.2.2 Aberration-corrected STEM . . . 51
3.2.3 Three Dimensional APT . . . 55
3.3 Discussion . . . 59
3.3.1 Grain Boundary Segregation Energy Calculation . . . 60
3.3.2 Segregation Energy from Thermodynamic-Based Model . . . 61
3.4 Conclusions . . . 65

4 THERMAL STABILITY OF DUAL-PHASE AL-MN ELECTRODEPOSITS - MODEL DEVELOPMENT 67
4.1 Experimental Procedures . . . 67
4.2 Phase Transformation Study . . . 70
4.3 Modification of Kinetic Models . . . 73
4.4 Data Fitting and TTT Diagram Construction . . . 77
4.4.1 Data Fitting Results . . . 78
4.4.2 The Implication of Kinetic Parameters . . . 81
4.4.3 TTT diagram . . . 82
4.5 Conclusions . . . 83
5 CASE STUDY - THERMAL STABILITY OF DUAL-PHASE AL-MN ALLOYS 85
5.1 Phase Transformation of Amorphous Al-Mn . . . 85
5.2 Phase Transformation in High Mn Concentration Al-Mn Alloys . . . 86
5.3 Data Fitting and TTT Diagram Construction . . . 87
5.4 Expansion of Kinetic Models . . . 90
5.4.1 Kinetic Model Development . . . 90
5.4.2 Data Fitting . . . 93
5.4.3 The Impact of Mn Concentration . . . 93
5.5 Conclusions . . . 95
6 CONCLUSIONS 99
7 DIRECTIONS FOR FUTURE RESEARCH 103
A EQUATIONS AND DERIVATIONS 105
A.1 Derivations . . . 105
A.2 Heat flow equation of two reaction process for Al-Mn dual phase alloy . . . 107
A.3 Heat flow equation of four reaction process for Al-Mn dual phase alloy . . . 109
B SUPPLEMENTAL MATERIALS AND OTHER REFERENCES 111
BIBLIOGRAPHY 113

LIST OF FIGURES

Figure 1 Schematic diagram showing the strength as a function of grain size[1]. Note that after critical grain size d_c, in general around 10nm, the Hall-Petch relationship will breakdown in most cases. 22

Figure 2 Real life application examples of Al-based nanocrystalline alloys, from sporting goods(a,b), fishing reel (c), to bicycle gears(d)[2]. 23

Figure 3 Volume-weighted average grain size and microstrain change of nanocrystalline Pd at room temperature. The grain size changed from 10 nm to 60 nm at room temperature in 24 hours[3]. 24

Figure 4 The phase diagram of Al-Mn system[4]. 25

Figure 5 Pilot scale of Al-Mn nanocrystalline electrodeposit in the form of (a) sheet and (b) hemisphere. Images from Dr. Shiyun Ruan at Xtalic Corporation. 26

Figure 6 Phases observed in molten salt electrodeposited Al-Mn alloys, with the Mn concentration ranges from 0 to 50 wt.%(25at.%). By varying the deposition and Mn composition, various structures can be achieved, showing the system is temperature and composition sensitive[5]. 27

Figure 7 Pseudo-binary Fe-Cr-Ni phase diagram at 70 wt.% of Fe[6]. 29

Figure 8 The relationship between grain size and Mn concentration under the same deposition current waveform. (a) is the grain size measured by XRD and TEM versus the concentration. (b) to (g) are the micrographs of the corresponding structures, with a range from 3 at.% Mn to 14 at.% Mn sample. 36

Figure 9 The as-deposited state of the sample studied here, with XRD in (a) showing 100% crystallinity and TEM micrograph in (b) showing an average grain size of 66nm. 37

Figure 10 The TEM micrographs of Al-Mn electrodeposits annealed at different conditions. (a) to (d) are samples annealed at 200°C for 30 minutes, 1 hour, 2 hours, and 4 hour. (e)(f)(g) are sample annealed at 300°C for 30 minutes, 1 hour, and 2 hours. (h) is the sample annealed at 400°C for 30 minutes. All the micrographs are at same scale, it's worth noting that the samples annealed at 200°C doesn't show a significant grain growth, nor does it show evidence of phase transformation. However, for samples annealed at 300 and 400 °C, the intermetallic forms within 30 minutes of annealing. Interesting, for the 300°C samples annealed at 2 hour, the microstructure doesn't change as well. 38

Figure 11 The XRD results of Al-Mn monocrystalline nanostructure annealed at 200°C at different time, showing there is no significant formation of intermetallic phase even at 4 hours of annealing. 39

Figure 12 The average grain size measured using the set of micrographs in Figure 10, with the grain size for the samples annealed at 200°C stabilized at around 100 nm. For the 300° sample, the grain size stabilized at around 110 nm. 40

Figure 13 The XRD pattern showing that for samples annealed at 300 and 400 °C, the intermetallic forms within 30 minutes. 41

Figure 14 The DSC data was fitted with JMAK analytical solution. The experimental results of three different ramping rates from 5 to 15 °C/min were shown here. From this fitting, the activation energy, reaction constant, and growth index can be calculated. 43

Figure 15 In the time and temperature space, for each heating profile, a reaction start and a reaction finish time can be calculated. By changing the heating rate, different reaction start and finish points can be acquired. Connecting the start/finish points at various heating rates, the TTT diagram is constructed. 44

Figure 16 The TTT diagram constructed using the parameters acquired from the DSC fitting in Figure 14. F is the notation for FCC and O is the notation for Al_6Mn. The start and finish of the reaction are marked. Note that at T = 400°C, the intermetallic formation starts within 30 minutes as suggested in the experiments. At 200°C (T = $0.5T_H$), the system is free from transformation for at least 3 months from the TTT diagram. 45

Figure 17 The (a)XRD and (b)TEM of monocrystalline 6.5 at.% Mn sample annealed at 200°C for one month. The TEM graph shows that the grain size is still able to maintain nanometer range and the XRD shows there are no siginificant formation of Al_6Mn intermetallic phase. 46

Figure 18 The (a)XRD and (b)TEM of monocrystalline 6.5 at.% Mn sample annealed at 300°C for one month. Unlike the structure in Figure 17, the sample shows large amount of Al_6Mn intermetallic phase, and the TEM also supports the XRD result. 47

Figure 19 (a) The half Mo grid used as APT experiment posts in FIB (b) The wedge of sample cut out by FIB welded using pyramid milling (c) The initial milling of the sample and (d) The final APT tip for experiment 51

Figure 20 Structural characterization of the as-deposited Al-Mn alloy film by (a) XRD and (b) bright field TEM. (a) shows that the material is Al FCC crystalline phase. (b) shows the grain size (in plan view) is about 162 nm on average, and the inset selected area diffraction (SAD) pattern conforms to a single phase FCC structure. 52

Figure 21 The grain size statistic of this particular sample for the grain boundary property studies. 52

Figure 22 Images of typical grain boundaries under Cs-corrected STEM. The low magnification BF image (a) depicts two adjacent grains and low magnification HAADF (b) shows the two grain boundaries exhibit Mn segregation. Images (c) and (d) are high magnification BF and HAADF, respectively. 53

Figure 23 An EDS composition line scan in Cs-corrected HAADF STEM (a) shows an increase in Mn concentration (at.%) at a grain boundary, which is imaged in (b). The start and finish direction of the scan is marked with the yellow arrow in (b). The average concentration of the line scan is 6.9 at.%, and the concentration at the boundary is about 10.5 at.% on average. (c) shows the scan at the same grain boundary using the area density method, with the Mn counts for right grain, left grain, and grain boundary plotted. By overlaying the curves, one can see that at the grain boundary, the Mn counts are higher. 55

Figure 24 (a) TEM picture of an APT sample. Green arrows mark the position of three individual grain boundaries. (b) The atom dot maps of Al and Mn and (c) Mn and Ga for the same sample. 56

Figure 25 Ladder diagram analysis of an individual grain boundary on the atom probe sample. Each line here represents a one dimensional 30 nm scan across the marked grain boundary, with an 1.8×1.8 nm^2 cross sectional area. The x axis is the cumulative total (Al+Mn) number of atoms while the y axis is the accumulated number of Mn atoms encountered in a one-dimensional traverse across the boundary. The slopes marked here represent the Mn concentration for each scan. The slopes all change across the grain boundary. (The blue dashed line and green dashed line show the concentrations for grain interiors, and the red dashed line denotes the region of higher slope that corresponds to the grain boundary.) The grain boundary is enriched by about 6.92 at.% Mn in line (a), 6.06 at.% in line (b), 4.77 at.% in line (c), and 3.68 at.% in line (d) as compared with the background level in the grains. 57

Figure 26 A schematic of how sample was divided was shown in (a), and the concentration distributions for regions in the grain boundary and grain interior of an APT sample are shown in (b). The average grain boundary concentration is 10.5 at.% Mn and the average concentration of the grain interior is 7.3 at.%. The degree of segregation (concentration difference between grain boundary and grain interior) is also plotted with a cumulative probability plot and histogram are shown in (c). The average degree of segregation is 3.1 at.% Mn for this grain boundary. 58

Figure 27 Frequency distribution for one of the atom probe samples with a volume of $36 \times 16 \times 234$ nm^3, divided up into blocks containing n = 200 atoms each, and compared with single binomial fitting and binomial-binomial fitting. The black dots show the experimental data frequency distribution. The single binomial fitting (red) significantly deviates from the experimental data, which is broader; suggesting the distribution of solute is not random. The data is further fitted with a dual-binomial function (solid blue line), with sub-distributions shown with dashed lines 60

Figure 28 The corresponding iso-concentration surface at c = 10.5% Mn for the volume analyzed in Figure 27 61

Figure 29 The average, maximum, and minimum segregation energy of the experimental values and the values calculated based on the Miedema segregation model. As is shown here, the averages in both cases are slightly postive, however, due to the variance in data sources, the calculated value has a range across +5 to -5 kJ/mol. 64

Figure 30 The as-deposited structures with different Mn concentration of Al-Mn alloys from chloraluminate ionic liquid bath under room temperature, with (a) 8.9 at.% Mn, which you can see a side peak at 38° 2θ embedded in the amorphous hump, which correspond to the Al (111) peak marked. Same for (b) with Mn concentration of 10.1 at.%. For higher concentration (c), (d) and (e), we see there is no Al (111) peak presented. There are some features emerging inside the amorphous hump (marked with upper triangle), which we believed is the indication of formation of icosahedral phase. 68

Figure 31 Three different kinds of DSC experimental results observed in Al-Mn alloy system with a ramping rate of 10 °C/min. The result shown in (a) shows a single asymmetric peak, and (b) shows a complex four-peak structure, and (c) shows a two-peak process. Besides the differences in the number of peaks, we can also see that as Mn increases, the transformation temperature increases. 69

Figure 32 TEM micrographs of (a) as-deposited 8.9 at.% Mn Al-Mn alloys and (b) (c) alloys annealed at 290°C for 1 hour. The annealed structure shows a region of Al FCC solid solution nanocrystalline diffraction rings in (b) and a mix of Al_6Mn orthorhombic structure and Al FCC rings in (c). In (c), the blue index and arrow show the diffraction spots which belong to the Al_6Mn structure; the diffraction rings for the Al FCC structure are marked by the green arc in both (b) and (c). 70

Figure 33 The XRD pattern of Mn 8.9 at.% sample (a) isothermally annealed at 290°C for 1 hour in DSC, which the DSC signal drops down to background suggesting the reaction process has completed. (b) shows the XRD of a sample ramped up to 550°C with a ramp rate of 5 °C/min. The Al FCC solid solution phase is marked with a down triangle. The fraction of Al FCC solid solution phase and Al_6Mn orthorhombic phase is acquired by Reitveld refinement. It is worth noting that neither phase has an amorphous hump, suggesting that at low temperature the Al_6Mn transformation is not completed. At high temperature, the Mn diffuses out from the Al-FCC solid solution sites to form Al_6Mn. The final fraction of the two phases in (b) is in good agreement with the value calculated from the phase diagram, which is 60.5% of Al_6Mn and 39.5% of Al FCC solid solution. 72

Figure 34 An example of the impact of different heating rates on the isochronal analysis process. The sample shown here were heated at 5, 20, and 50 °C/min. As heating rate increases, the peak becomes broader and the asymmetry becomes more significant. 73

Figure 35 The DSC peaks for Mn 8.9 at.% (a) and 10.1 at.% (d) samples. (b) (c) and (e) (f) are its corresponding first and second derivatives. The samples were both ramped from room temperature to 550°C with a ramp rate of 50 °C/min. The peak shows asymmetry. The first derivative and second derivative combined with the XRD results shown in Figure 33 suggests that there were two reactions in the annealing process. It is worth noting that for 10.1 at.% sample, the reactions are shifted to higher temperature and the two reaction temperatures are closer, thus it is harder to distinguish the two peaks. However, we still found a slight peak at in the second derivative in (f), suggesting the two samples follow the similar reaction route. 74

Figure 36 The schematics of transformation mechanism for the two reaction process. A stands for amorphous phase, F is for FCC, and O is for orthorhombic Al_6Mn. The reaction starts with nano-scale FCC crystals embedded in amorphous matrix, in which crystallization of amorphous phase started first and then eventually reached the equilibrium FCC-Al_6Mn mixture. The black lines are the grain boundaries. 75

Figure 37 The experimental data (dots) and corresponding fitting results (lines) for 8.9 at.% Mn of Al-Mn alloys with DSC heating rates from 5 °C/min to 50 °C/min from room temperature to 550°C. The fitting was done with non-linear least square fit with 5000 iterations. The activation energy Q and the growth index n are set as equal across different heating rates. The fitted curves capture the asymmetric traits in the experimental data. 80

Figure 38 The same Q fitted for a 10.1 at.% Mn sample, the fittings was able to capture the temperature shift due to the concentration difference in Figure 37 and at the same time gives a reasonable fit, suggesting that the assumption that the activation Q for a reaction doesn't change with Mn concentration is reasonable. 81

Figure 39 (a)The TTT digram constructed using parameters acquired in DSC data fitting in Figure 37. The region in red shows the time and temperature for amorphous to FCC crystallidzation process and blue shows the FCC crystallites futher transforms into Al_6Mn intermetallic. At higher temperature, the crystallization reaction is really fast and no overlap with the precipitation process, i.e. the reaction steps are distinct two steps process. However, at lower temperature, the two reactions overlap together, which agrees with the DSC data.(b)shows the TTT for 10.1 at.% Mn, which is nearly the same as in (a), but can retain the amorphous structure longer during annealing. 83

Figure 40 (a) Shows a diffraction ring for the as-deposited state and (b) After annealing at 350°C for 1 hour, the diffraction pattern shows extra diffraction rings, which is an indication of icosahedral phase formation. 87

Figure 41 (a)The isothermal annealing for 10.1 at.% sample, showing a peak for a typical nucleation and growth process and (b) For 13.7 at.%, the monotonically decreasing signal suggests a growth process. The initial rise is from the instrument to reach equilibrium condition. 88

Figure 42 The dataset and fitting result of 13.7 at.% Mn sample, using the exact same fitting equation as the fitting for the low concentration dual-phase alloys. 89

Figure 43 The corresponding TTT diagram for 13.7 at.% Mn sample, which shows the first transformation process finishes before the starting of the second reaction. 90

Figure 44 The schematics for the proposed reaction in the middle range concentration dual-phase system. In which the sample is originally composed of FCC, amorphous, and icosahedral phase. Following two different reaction routes $A \rightarrow F \rightarrow O$ and $I \rightarrow O$), the final structure is composed of FCC and Al_6Mn intermetallic phase. 91

Figure 45 12.5 at.% Mn DSC data with ramping rate of 15 °C/min with fitted curve, the model captures the middle peak in between the two major reactions, however, the position is not exact due to the complexity of the peak sets. 94

Figure 46 (a)The TTT diagram for the 12.5 at.% Mn sample, in which two reaction routes compete with each other. The first route is the A(amorphous) $\rightarrow$ F(FCC) $\rightarrow$ O(Al_6Mn) phase (isolated out to plot at (b)) and the second route is the A(amorphous) $\rightarrow$ I(icosahedral) $\rightarrow$ O(Al_6Mn) process (isolated out to plot at (c)). The reaction time and temperature for the low temperature (A to I or A to F) are also compared in (d) and high temperature reactions I to O and F to O are compared at (e). One can see that at lower temperature, the amorphous to FCC phase happens faster compared to the amorphous to icosahedral phase, the F to O reaction also happens faster than the I to O phase. However, at temperature above 400°C, it is easy for the icosahedral phase to rapidly transform into the intermetallic phase. 97

Figure 47 Time and temperature relationship for the starting reaction of (a) FCC(F) to Al_6Mn(O) (b) amorphous(A) to FCC(F) (c) amorphous(A) to icosahedral(I) and (d) icosahedral(I) to Al_6Mn(O) reaction compared at different Mn concentrations. 98

LIST OF TABLES

Table 1 The relationship between the concentration of the deposition bath and the concentration of the deposited alloys. The concentration for the deposited alloy (Mn in at.%) is with a ±0.4 at.% error and measured with SEM-EDS; the concentration of electrolyte was calculated in the sample preparation process. 32

Table 2 The meaning of growth index n in 3 dimensional process (d=3). . 43

Table 3 Results of effective heat of segregation H_{seg} extracted from experimental data at room temperature using McLean isotherm analysis. Here, the grain boundary thickness used to calculate the heat of segregation using area density from STEM line scan is assumed as 1 nm. . . . 62

Table 4 Results of effective heat of segregation H_{seg} calculated using Equation 12, the $\Delta H^{int}_{Bin_A}$ are from two different sources: Miedema data and CALPHAD data. The subscript 1 and 2 showing the different sources of the elastic term in Eqaution 13. The calculated values used here including the bulk and shear modulus are shown in Table 9 63

Table 5 The fitted values for 8.9 and 10.1 at.% Mn, as mentioned in the context, the activation energies fall within literature values and aligns well in the value found in Chapter 2. It is worth noting that the growth index n also changes in the fitting, due to the fact that if more pre-existing nuclei presented, the growth index will be larger. 78

Table 6 Upper and lower limit of literature values of activation energies from amorphous Al crystallization as well as Al_6Mn precipitation. The data is compared and collected with Reference [7, 8, 9, 10]. 79

Table 7 Diffusion activation energy of Mn in Al[11, 12, 13, 14] 88

Table 8 Summary of reaction mechanisms at various concentrations at elevated temperature. "D" is a diffusion-controlled process, "I" is an interface-controlled process, and "/" is not applicable. A→F is for the amorphous crystallization, F→O is for the Al_6Mn precipitation in FCC, A→I is for the amorphous to icosahedral phase transformation, and I→O is the icosahedral to Al_6Mn phase transformation. 95
Table 9 The data used for H_{seg} calculation using Equation 12. The subscript 1 and 2 showing the differenct sources of the elastic term in Equation 13. 1 is from the Miedema source and 2 is from online database. . . . 111

ACRONYMS

APT Atom Probe Tomography

BF Bright Field

Cs-STEM Aberration-corrected Scanning Transmission Electron Microscopy

DSC Differential Scanning Calorimetry

EDS Energy Dispersive Spectroscopy

EMIMCl 1-Ethyl-3-Methylimidazolium Chloride

FIB Focused Ion Beam

HAADF High Angle Annular Dark Field

JMAK Johnson-Mehl-Avrami-Kolmogorov

SAD Selected Area Diffraction

SEM Scanning Electron Microscopy

TEM Transmission Electron Microscopy

TGA Thermogravimetric Analysis

TTT Time-Temperature-Transformation

XRD X-Ray Diffraction

1

INTRODUCTION

This chapter aims to provide the background information about the recent advancement in processing methods for nanocrystalline/amorphous metals, and also highlights the importance of microstructure control. A discussion on the stability associated with the targeted microstructure, which is the core of this thesis, is also presented.

1.1 NANOCRYSTALLINE AND AMORPHOUS METALS

Nanostructuring has been known to effectively increase the hardness of a metal without significantly compromising the ductility[1, 15, 16]. A famous example is the improvement in mechanical properties expected based upon the Hall-Petch relationship shown in Equation 1, which states that the yield stress (σ_y) is inversely proportional with the square root of grain size (d), i.e. the strength or hardness should increase with decreasing grain size[1, 15, 17, 18, 19], as shown in Figure 1.

$$\sigma_y = \sigma_0 + \frac{k_y}{\sqrt{d}} \tag{1}$$

Such improvements in lightweight metals such as Al, can be beneficial for applications that require higher specific strength, high specific modulus, high fatigue limit, good wear resistance, and high corrosion resistance such as sporting goods, fishing reels, and bicycles gears etc., which are already currently used in practice[2], as shown in Figure 2. However, despite the enhanced mechanical properties of nanocrystalline metals, due to their high grain boundary area densities, pure nanostructured metals generally coarsen rapidly even at low temperatures. For example, room temperature grain coarsening has been observed in nanocrystalline Pd in 24 hours, where the grain size changes from 10 to 60 nm overnight and then subsequently explodes to the micrometer scale in two months[3]. It has also been shown that for a nanostructured Al-0.13%Mg alloy,

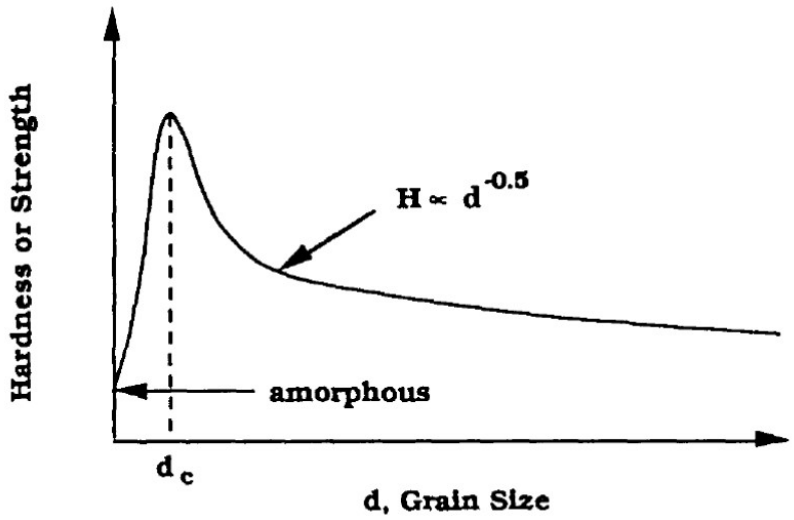

Figure 1: Schematic diagram showing the strength as a function of grain size[1]. Note that after critical grain size d_c, in general around 10nm, the Hall-Petch relationship will breakdown in most cases.

when the sample is heated above 170°C, the average grain size can increase to the microscale within an hour[20].

Aside from single-phase nanocrystalline alloys, the dual-phase structures with nanocrystals embedded in amorphous matrix have also received a lot of attention. Besides the enhanced mechanical properties such as wear resistance and the potential soft magnet application for iron-based alloys[21, 22], amorphous alloys has been extensively used as precursors for producing nanocrystalline alloys[23, 24, 25, 26]. However, due to the usually complicated compositions of amorphous alloys and the multiple reactions involved in their crystallization, there is no existing kinetic model that can expand from descriptive methods to a more predictive model for these phase transformations. If a more predictive model can be developed, a more efficient way to evaluate the stability of nanocrystalline/amorphous structures can be delivered.

1.2 ALUMINUM-MANGANESE ALLOY SYSTEM

Aluminum-Manganese (Al-Mn) is a complicated system with various intermetallic phases presented on the phase diagram[4]. It is also the first system discov-

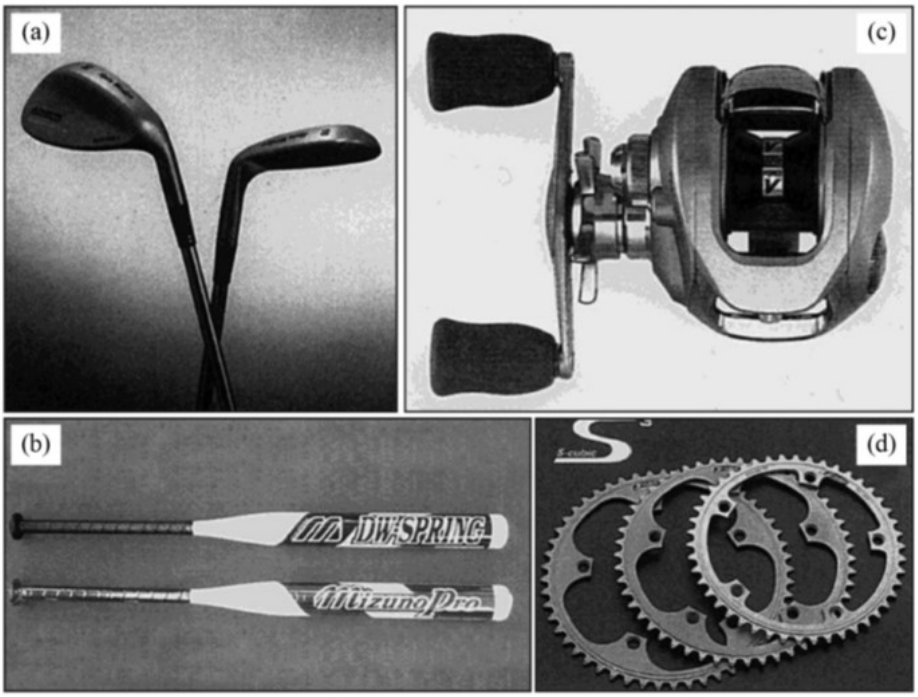

Figure 2: Real life application examples of Al-based nanocrystalline alloys, from sporting goods(a,b), fishing reel (c), to bicycle gears(d)[2].

ered with the short-range ordered icosahedral phase[27], in which the nanoscale icosahedral phase dispersion in amorphous matrix has shown superior mechanical properties and potentially can be used to create a new set of Al alloys[28]. Through different processing methods, the binary Al-Mn system has shown a wide variety of equilibrium and metastable phases including solid solutions, several intermetallic phases, and the quasicrystalline icosahedral structure across temperatures from 150 to 330°C and in the a narrow range between 0 to 50 wt.% of Mn (25 at.%)[29, 30], showing the system is very temperature and composition sensitive.

Mn is also a common alloying element in commercial Al alloys. For example, the non-heat treatable 3xxx series of Al alloy use Mn as a major alloying element from 0.3 to 1.5 %, which has moderate mechanical strength, high ductility, and excellent corrosion resistance. The applications are manufacturing foil, roof sheets, and cooking utensils etc. The binary Al-Mn 3003 alloy has been used in rigid containers. Another example is the 6xxx heat treatable Al alloy, which contains a trace

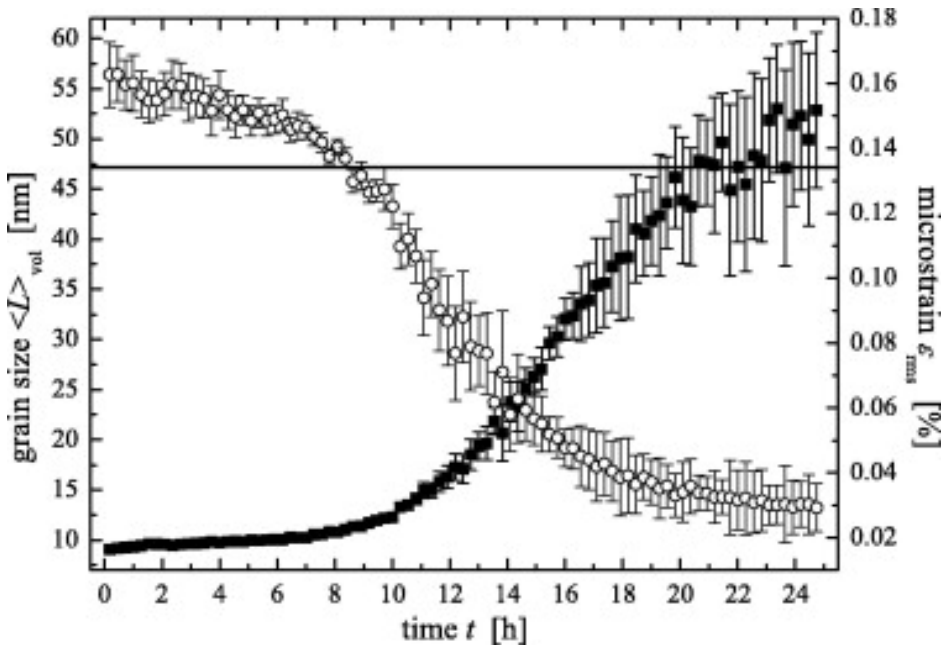

Figure 3: Volume-weighted average grain size and microstrain change of nanocrystalline Pd at room temperature. The grain size changed from 10 nm to 60 nm at room temperature in 24 hours[3].

amount of Mn from 0.03 to 1.1 %. This class of alloy is precipitate hardened and commonly used in aircraft and automotive applications, as well as structural materials in architectural applications. In short, it is worthwhile to examine methods for engineering the Al-Mn alloy to a desirable microstructure.

1.2.1 *Electrodeposition of the Al-Mn Alloy System*

The wide degree of control over nucleation and growth kinetics available in electrodeposition can produce materials with a variety of internal structures, with grain sizes ranging from the micro- to the nanoscale[31, 32, 33, 34, 35, 36, 37, 38]. Among them, nanocrystalline electrodeposits are particularly interesting due to the improvements in properties such as strength and hardness that result from grain refinement[1], and the ability of this technique to modulate composition and structure to nanometer scales[39].

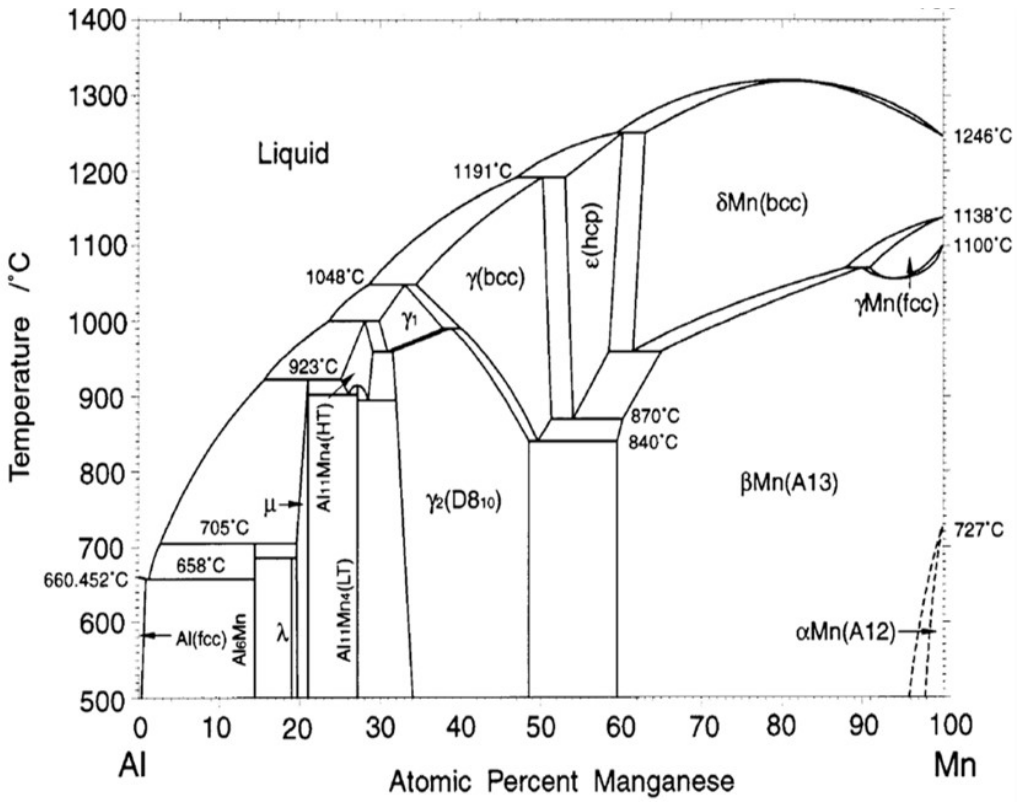

Figure 4: The phase diagram of Al-Mn system[4].

As a result, there is increasing attention on alloys produced by electrodeposition, as the addition of solute elements to a nanocrystalline deposit can result in kinetic solute drag, which slows grain boundary motion, as well as thermodynamic energy reduction caused by segregation of solute atoms to grain boundaries[40, 41, 42, 43, 44]. The use of electrochemical fabrication for nanostructured alloys has received attention due to the high production rate, low cost, low porosity (can be fully-dense structured if controlled properly), and high purity. It also has the capability to overcome shape limitations and allow the production of freestanding parts with complex shapes, as well as coatings on widely different substrates, which is shown in Figure 5.

Aside from the traditional aqueous electrodeposition process, the advancement in high temperature molten salt electrodeposition and ionic liquid electrodeposition has also enabled electrodeposition processes to be more widely used. For example, the Al-Mn system has been deposited using molten salt systems at

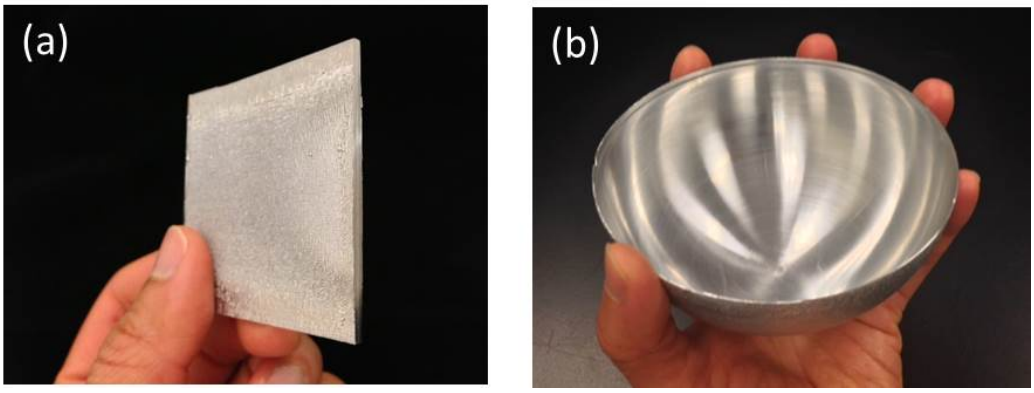

Figure 5: Pilot scale of Al-Mn nanocrystalline electrodeposit in the form of (a) sheet and (b) hemisphere. Images from Dr. Shiyun Ruan at Xtalic Corporation.

higher temperature[45, 46]. In such molten salt electrodeposition, by changing the temperature or Mn concentration, different structures can be achieved (Figure 6). However, the high temperature process in the molten salt electrodeposition process is energy intensive and at the same time the cell is prone to corrosion, and other side reactions such as deposition of unwanted phases can also happen. Ionic liquid electrodeposition, on the other hand, has proven to be safe and scalable, at the same time capable of producing various microstructures. Ionic liquid electrodepsition is also known for its low flammability, low toxicity, and wide electrochemical window, which makes it getting more and more desirable for industrial practice. As a result, in this study, the processing of Al-Mn electrodeposits will be conducted using the ionic liquid electrodeposition process[34, 47, 48, 49, 50, 51, 52].

Previous work from the Schuh group at MIT showed that Al-Mn alloys electrodeposited from acidic chloroaluminate ionic liquid at room temperature can produce many of these structures with a variety of characteristic length scales, ranging from microcrystalline to nanocrystalline, as well as dual-phase nanocrystalline/amorphous structures, and at specific concentration, icosahedral phase was also observed[34, 47]. What is more, for a duplex deposit containing both crystalline and amorphous regions, a three-dimensional atom probe tomography study of this system showed a subtle preference of Mn for the amorphous phase vis-á-vis the crystalline one[53]. Such a preference is a strong indication that Mn may perhaps also prefer the disordered regions such as grain boundaries in the

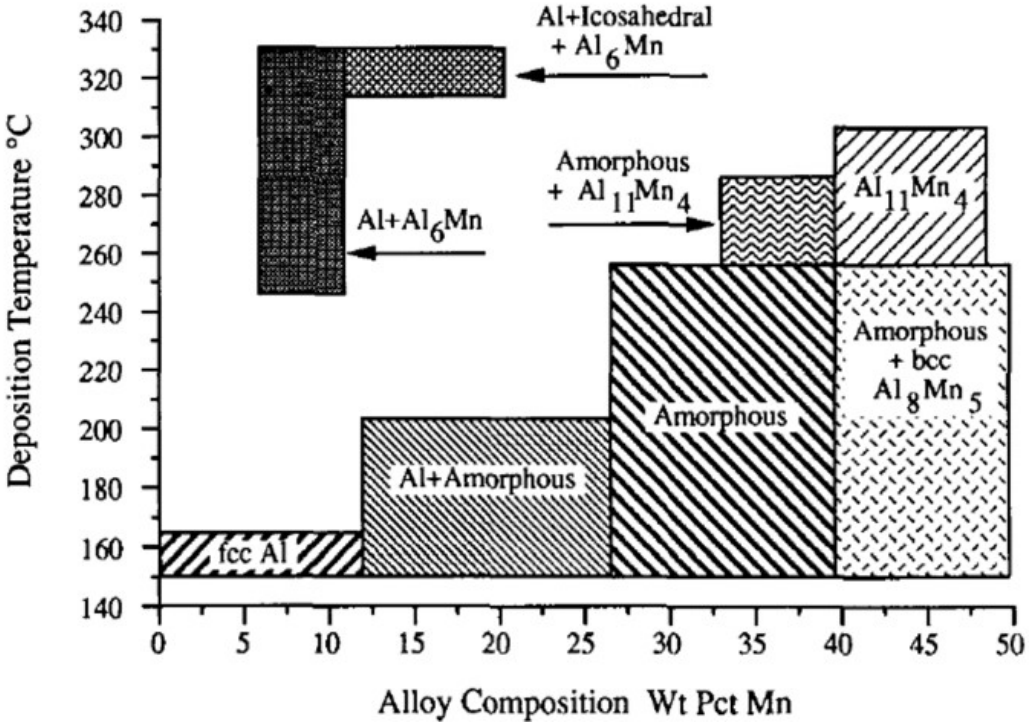

Figure 6: Phases observed in molten salt electrodeposited Al-Mn alloys, with the Mn concentration ranges from 0 to 50 wt.%(25at.%). By varying the deposition and Mn composition, various structures can be achieved, showing the system is temperature and composition sensitive[5].

Al-Mn system, however, no grain boundaries were studied in that work and the possibility of Mn segregation to grain boundaries remains speculative. To have a thorough understanding of the grain refinement mechanism as well as the stabilization study, more studies on the grain boundary structures are needed.

1.3 THERMAL STABILITY

Aside from the microstructure coarsening problems mentioned in Section 1.1, where the grain size can change from nanometer scale to micrometer scale, second phase formation at elevated temperature can compromise the performance of an alloy greatly. For metal alloys, precipitates at the grain boundary can lead to grain boundary embrittlement. Figure 7 shows a pseudo-binary Fe-Cr-Ni phase dia-

gram at 70 wt.% of Fe[6], where as the brittle phase forms at 475°C, embrittlement happens. In electrodeposited system such as Co-P, it has been shown that upon annealing, the P atoms segregate to the grain boundary and while P-saturation of the grain boundary is reached, the grain boundary sites form P-rich precipitates accompanied by rapid grain growth. Moreover, the saturation of P and precipitation occurs earlier because of the higher concentration which leads to a lower thermal stability[54]. However, in the case of electrodeposited Ni-Mn alloy, at higher temperature, the Mn segregation appears as a plausible mechanism for the thermal stability and grain boundary pinning by precipitation contributes to the improved microstructural stability above 600°C[55]. As one can see, even with similar behavior, i.e., solute segregation at grain boundary upon annealing, one of the alloy shows lower stability because of the precipitation, however, the other shows improved stability because of the pinning by precipitates. These show the complicated role of precipitation reaction in the thermal stability of the electrodeposits.

Ni-P is another well-studied electrodeposited system. Electrodeposited nanostructured Ni-P has been discovered with grain boundary segregation in the as-deposited state and upon annealing, P will segregate more to the grain boundary forming a P-rich grain boundary phase, and then subsequently form a Ni_3P precipitate[56]. The nanostructure was found to be stable up to certain temperature depending on the P concentration due to pinning of grain boundaries by the precipitates, and further heating leads to grain growth which is concurrent with Ni_3P intermetallic formation[57, 58, 59]. The formation of Ni_3P precipitates impact the fracture strength and fracture strain due to the connectivity of Ni_3P grains, where cracks are preferentially nucleated. As a result, it is important to understand not only the grain growth process, but also the phase decomposition and precipitation of the alloys.

Tremendous effort has been expended to understand the transformation process using, e.g., experimental tools which use the semi-empirical Kissinger analysis to extract the activation energy[60, 61]. However, even in systems like Ni-P, there is not yet a well-established time and temperature relationship on the phase transformation process. There has been a gap between the descriptive analysis and a more predictive model based on the experimental data. If a more predictive model can be developed, it will not only help to understand the thermal stability,

but at the same time give a better tool for microstructure control as well as better capabilities in evaluating the viability of the alloys.

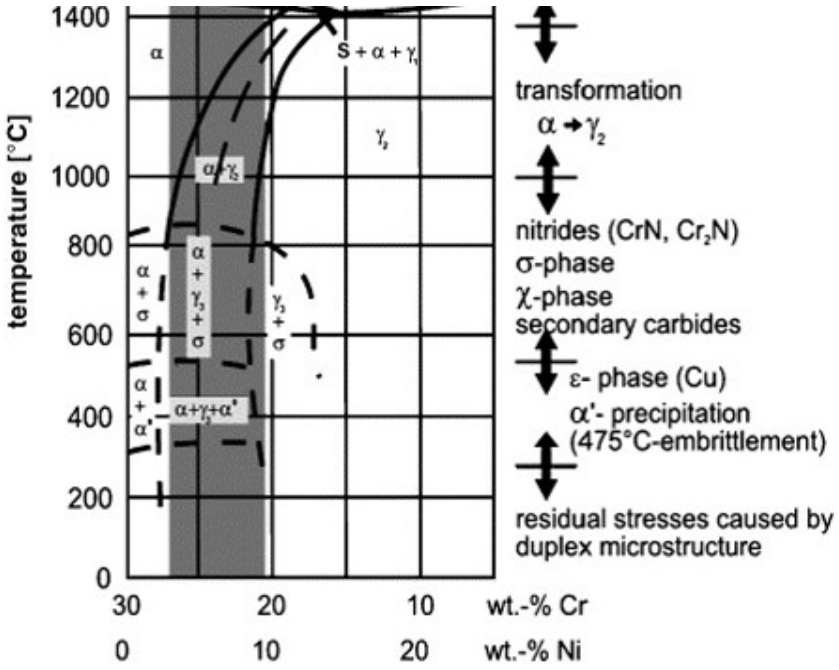

Figure 7: Pseudo-binary Fe-Cr-Ni phase diagram at 70 wt.% of Fe[6].

1.4 PROBLEM STATEMENT AND STRUCTURE OF THESIS

This thesis is aimed at investigating the stability of nanocrystalline/amorphous Al-Mn electrodeposited alloys. Because of their enhanced mechanical properties, these microstructures have received lots of attention, however, there are currently no systematic studies on how stable the structures are. In this thesis, besides simply assessing the viability of alloys at different temperature and time ranges, the stabilization mechanism of the nanocrystalline metals will also be discussed. It is believed that improved nanocrystalline stability can be provided by grain boundary segregation of solutes due to the kinetic solute drag as well as the potential of grain boundary energy minimization. However, current evidence on the Al-Mn system only shows that Mn slightly prefers the amorphous phases[53], and from some calculations[62], it has been suggested that grain boundaries should exhibit

anti-segregation of Mn. As a result, it is necessary to study the grain boundary structure for the nanocrystalline phase to understand the role of grain boundary segregation in nanocrystalline stability. A kinetic model will also be used to explain the transformation process to set an internal reference for the dual-phase/amorphous structure as that occur in these alloys, whether they are single-phase nanocrystalline solid solution, amorphous or complex structures with multiple coexisting phases in the as-deposited condition. With the information acquired from the descriptive kinetic model, a predictive set of kinetic tools will be presented. This thesis is organized into three main parts to address the posed research questions.

- Chapter 2: The structure Al-Mn electrodeposits will be studied. In this chapter, the basic properties such as grain size-concentration relationship will be explored. More importantly, the thermal stability of single phase nanostructured Al-Mn will be examined, in which not only grain growth but also the phase decomposition process will be examined experimentally. The phase transformation process will be studied using a kinetic model and expanded towards a more predictive approach with the construction of time-temperature transformation diagram. The behavior of extended annealing conditions will also be studied.

- Chapter 3: In this chapter, the stabilization of the Al-Mn alloy will be explored. The grain boundary structure, both morphologically as well as chemically, will be studied in detail using advanced experimental techniques such as aberration corrected scanning transmission electron microscopy and three dimensional atom probe tomography. The segregation energy calculated based on the experimental data will be discussed along with the segregation energy calculated using a thermodynamic based model.

- Chapter 4 and 5: The thermal stability of the dual-phase alloy at various concentration will be studied, and a kinetic model will be developed and compared with the transformation mechanism and parameters in Chapter 3. In this part, the role of Mn in the system will be discussed in detail. The developed analytical model will also be tested, showing its ability to extrapolate across time-temperature space without intensive experimental studies.

2

THERMAL STABILITY OF NANOSTRUCTURED AL-MN ALLOYS

In the literature, it has been shown that Al-Mn electrodeposits synthesized from chloroaluminate ionic liquid solution can have various structures via different solute (Mn) incorporation levels, in which an increase of Mn concentration decreases the grain size and eventually frustrates the structure into forming an amorphous phase, which improves the mechanical performance[34]. However, these enhanced mechanical properties are a direct result of microstructure refinement, and the stability of these refined structures have never been thoroughly studied. Here, similar procedures have been applied to produce a single-phase nanostructured Al-Mn alloy, and the stability of nanocrystalline materials are explored, including grain growth and phase transformation analysis.

2.1 BASICS OF AL-MN NANOSTRUCTURED ALLOYS

2.1.1 *Materials Synthesis*

Al-Mn nanocrystalline alloys were prepared by electrodeposition at room temperature from a chloroaluminate ionic liquid solution, which was prepared with 1-ethyl-3-methylimidazolium (EMIMCl) (98 %, IoLiTec) and anhydrous aluminum chloride ($AlCl_3$, 99.99%, Sigma Aldrich) with a 2:1 molar ratio in a nitrogen glovebox with water and oxygen level below 1 ppm, as described in detail in Ref.[34]. To control the concentration of the deposited alloy, anhydrous manganese chloride ($MnCl_2$, 99.99%, Alfa Aesar) was added into the ionic liquid and stirred until fully dissolved. The amount of $MnCl_2$ was varied to effect the targeted alloy composition. For the single phase nanocrystalline alloys which were used to study nanostructure stability, the Mn concentration for the as-deposited alloy was around 6.5 at.% with $MnCl_2$ concentration around 0.065 mol/L. As for the whole range of study in this thesis, the concentration of $MnCl_2$ ranged from 0.03 to 0.12

mol/L. The relationship between the $MnCl_2$ concentration in the electrolyte and the deposited alloy concentration under the deposition voltage condition used in this study is shown in Table 1. Pure aluminum foil (99.99% purity, purchased from Alfa Aesar) was used as the anode, in which the aluminum anode was first treated with an etching solution with 75% phosphoric acid, 20 % sulfuric acid, and 5% nitric acid to remove the oxidized area and impurities. Copper sheets (99% purity) cut into 2 cm by 2 cm were first connected with copper cord plastic resin wire using silver gel and embedded in a non-conductive resin. The copper sheets were then polished with 1200 grit sandpaper and used as the cathode. Prior to soaking the Cu electrode in the electrolyte bath, the Cu electrode was treated with 5 vol.% sulfuric acid to remove oxidation and impurities, and then soaked in chloroaluminate ionic liquid solution overnight to activate the electrode in order to enhance the adhesion of the deposits.

A reverse-pulse current waveform was used in the process due to its known benefits for mechanical behavior and surface finish[63, 64, 65, 66]. Pulse plating was conducted with a square current waveform composed of 6 mA/cm^2 of cathodic pulse and 3 mA/cm^2 of anodic pulse, each of 20 ms duration, following the procedure in Ref. [48]. The total deposition time was 8 to 16 hours, leading to a deposit with a thickness around 10 to 20 μm. The sample was released by dissolving the copper substrate in concentrated nitric acid($\geqslant$70% concentration). Note that the samples tested in this thesis were mainly from the center of the electrode to assure the homogeneous composition as well as the no stress induced because of the edge effect in typical electrodeposits.

Table 1: The relationship between the concentration of the deposition bath and the concentration of the deposited alloys. The concentration for the deposited alloy (Mn in at.%) is with a $\pm$0.4 at.% error and measured with SEM-EDS; the concentration of electrolyte was calculated in the sample preparation process.

$MnCl_2$ (M)	0.03	0.06	0.07	0.075	0.09	0.11	0.125
Mn (at.%)	3.0	6.5	7.0	8.3	10.1	12.5	13.7

2.1.2 *Materials Characterization*

The compositions of the electrodeposits were analyzed using a JEOL JSM-6610LV scanning electron microscope (SEM) with calibrated energy-dispersive x-ray spectroscopy (EDS) operated at 20kV before releasing them from their copper substrates. Multiple points were tested to ensure the composition of the alloy. After EDS testing, the samples were released from the substrate using concentrated nitric acid and separated into different groups based on their composition. X-ray diffraction (XRD) was carried out with a PANalytical X'Pert X-ray diffractometer operated at 45 kV and 40 mA with a Cu K_α source to study the crystallinity and phases. The data was analyzed using Rietveld refinement to ascertain grain size and crystallinity using PANalytical HighScore Plus software. The Rietveld refinement calibration was done with standard silicon powder 640b with slit size 2° and beam size 4 mm from 15 to 125 °2θ. Aside from XRD, transmission electron microscopy (TEM) was also employed to give a direct observation on the grain size and crystallographic information with a JEOL 2010F TEM operated at 200 kV. The TEM samples were prepared using both electro-jet-polishing and ion-milling, and the two preparation methods were found to yield the same results in later TEM studies. For the electro-jet-polishing procedure, 5% perchloric acid in 20% butoxyethanol and 75% methanol was used as the polishing solution, and the system was operated under a voltage of 15V at -60°C, using a Fischione model 100 twin-jet electropolisher. Ion-milled samples were polished with 5 kV first at 18°, gradually reducing to 4kV and 12°, at a temperature below -60°C; the instrument used here was Fischione 1010 ion mill.

2.1.3 *Annealing Studies*

Differential scanning calorimetry (DSC) was employed to study the annealing behavior of the experimental materials. The DSC experiments were conducted using a TA Discovery instrument. At least 1 mg of sample was placed into the Tzero Aluminum pan, which was weighed both with and without the sample with a precision of 0.0001 mg using the TA discovery thermogravimetric analysis (TGA) pre-weight function. Multiple samples were tested at a given composition. The samples were scanned over the temperature range between 50 to 550°C

at a constant heating rate ranging from 5 to 50 °C/min. The DSC tests used an empty pan as a reference and were all conducted under flowing nitrogen gas to limit sample oxidation. After the heating steps, the sample was cooled rapidly at 100°C/min to prevent further transformation. For some selected samples, DSC was conducted isothermally for different durations at different temperature set-points. Afterwards, selected heat-treated samples were studied with XRD and TEM. Rietveld refinement was used for XRD analysis to understand the phase ratio of the post-annealing structures. The data processing and template for Rietveld refinement are the same as described in Section 2.1.2. For DSC analysis, a linear background was subtracted from the raw data for kinetic analysis, and the data was then further integrated and normalized to reflect the fraction transformed as a function of temperature (note that due to the isochronal analysis here, the temperature is a function of time). The Johnson-Mehl-Avrami-Kolmogorov (JMAK) model was then used to analyze the transformation process, for which the details will be presented in Section 2.4.

Extended annealing was done on selected samples at 200 and 300°C for one week, two weeks, and one month to study the effect of annealing time on the grain size and phase composition of the annealed alloys. Prior to annealing, the samples were ampoule-sealed in glass with an Ar atmosphere to prevent oxidation. Annealed samples were then characterized using XRD and TEM. All the characterization methods and instruments were the same as described in Section 2.1.2. The results of extended annealing were compared with the JMAK analysis to give a better understanding of the transformation process.

2.2 GRAIN SIZE WITH RESPECT TO DIFFERENT MN CONCENTRATION

The average grain sizes were calculated using both TEM dark field images as well as XRD Rietveld refinement. The results are shown in Figure 8. At 3 at.% Mn, the Al-Mn electrodeposits have a grain size on the micrometer scale. However, at around 6 at.%, the grain size decreases to around 160 nm. Further increase of Mn concentration decreases the grain size more, and at around 8 at.%, evidence of an amorphous phase starts to appear in the as-deposited structures. Up to 12.5 at.%, the increase of Mn concentration increases the fraction of the amorphous phase, beyond which the sample appears to be nearly amorphous. However, at

somewhat higher concentrations near 14 at.%, which is close to the stoichiometry of the intermetallic phase Al_6Mn, there is some localized ordering structure forming, which is believed to be an icosahedral phase and will be discussed later in Chapter 5. Note that for the specific XRD instrument used here, the sensitivity of the instrument to grain size peak broadening is only able to quantify the grain size smaller than about 80 nm accurately. Values higher than 80 nm are therefore omitted. For amorphous phase dominant situations, due to the presence of the amorphous hump in the XRD peak, the grain size could not be quantified either (for Mn concentration larger than 8 at.%), as a result, only three XRD grain sizes are shown in Figure 8.

2.3 MICROSTRUCTURE EVOLUTION

The XRD and TEM of a typical as-deposited single-phase nanocrystalline sample are shown in Figure 9(a) and Figure 9(b) individually. This sample has a composition of 6.5 at.% Mn and exhibits nanocrystalline grains around 66 nm in diameter, with the XRD showing no second phase present.

After annealing at 200, 300, or 400°C isothermally from 30 minutes to 4 hours, microstructural difference can be observed in this sample. The TEM micrographs for the annealed structures are shown in Figure 10. Within 30 minutes, the samples annealed at 300 and 400°C already show precipitates of Al_6Mn phase. At 200°C however, even at 4 hours of annealing time, the nanostructure seems to be maintained. The XRD data was further analyzed to compare with the TEM data. The XRD for samples annealed at 200°C for different duration are shown in Figure 11. The XRD further confirms that at 200°C, which is 0.5 homologous temperature (T_H), i.e., half of the melting point of pure Al, the grain size increases slightly after the first 30 minutes of annealing. However, as the time increases, the grain size stabilizes at around 100 nm, as shown in Figure 12. Furthermore, in both XRD and TEM for the post-annealing samples, there is no evidence for the formation of intermetallic phase, suggesting that at this high temperature, the single-phase Al-Mn nanostructure is essentially stable. This stability is believed to be linked to the grain boundary structure of Al-Mn nanocrystalline alloy, which is the subject of discussion in Chapter 3.

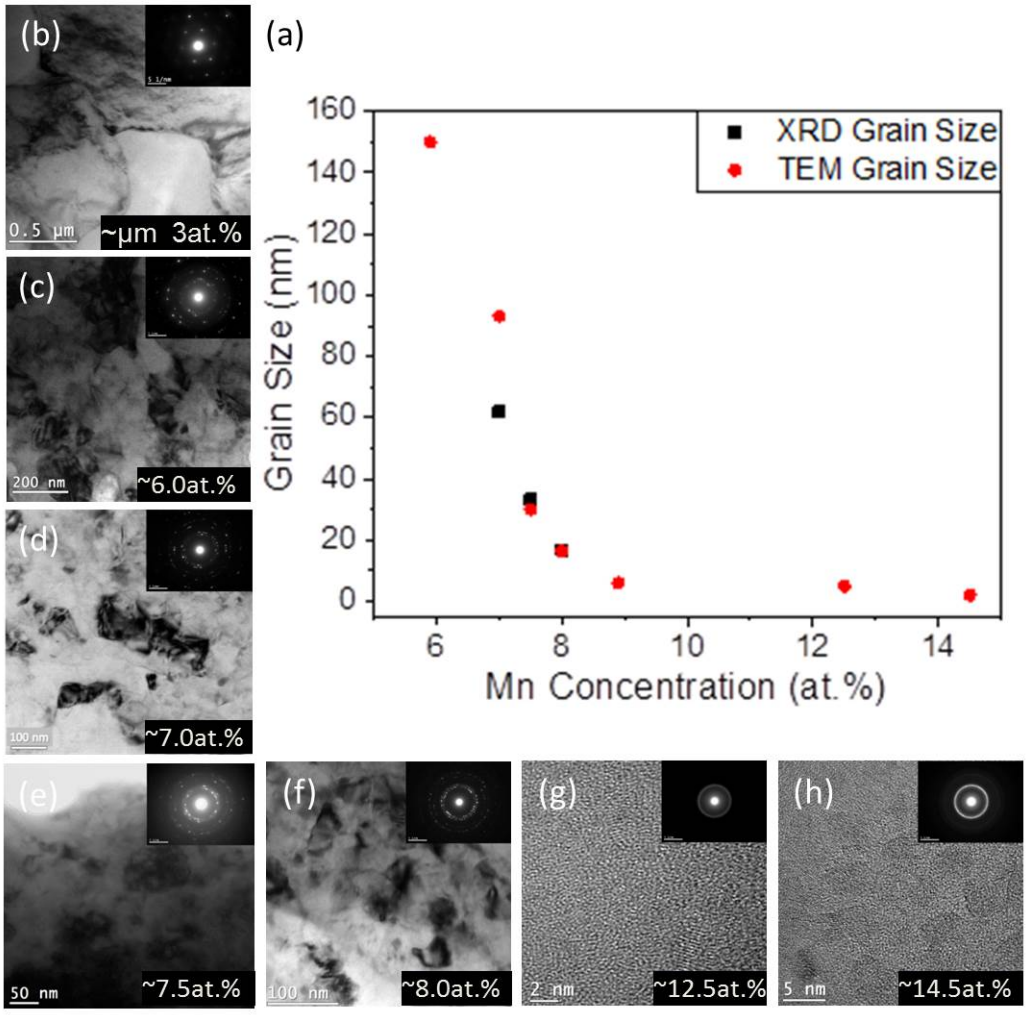

Figure 8: The relationship between grain size and Mn concentration under the same deposition current waveform. (a) is the grain size measured by XRD and TEM versus the concentration. (b) to (g) are the micrographs of the corresponding structures, with a range from 3 at.% Mn to 14 at.% Mn sample.

For samples annealed at 300 and 400°C, the XRD patterns are shown in Figure 13, revealing that after 30 min of annealing, a large amount of intermetallic phases formed. The TEM images also reveal the formation of intermetallic compounds, however, the grain size, still, after a slight relaxation during the initial annealing stage, apparently stabilized at 110 nm and 150nm for the two temperatures. It is concluded that, for all of the annealing conditions studied here, grain growth ar-

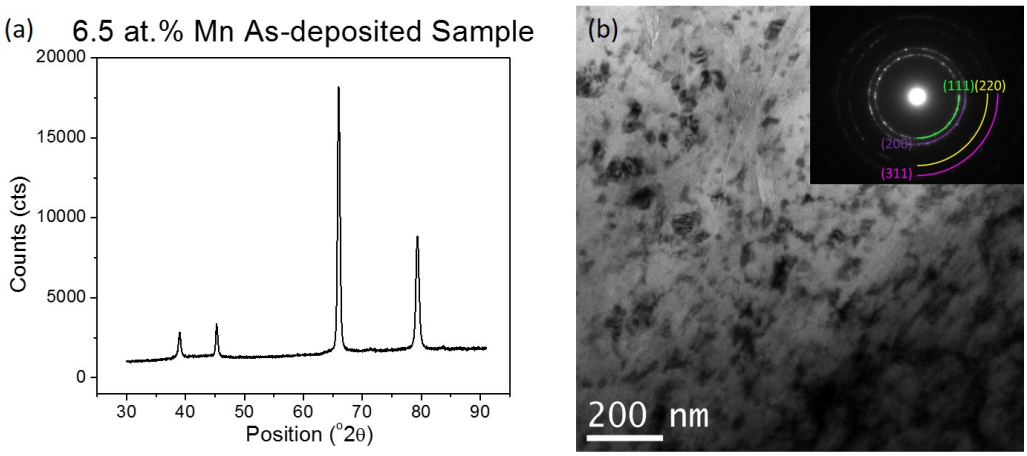

Figure 9: The as-deposited state of the sample studied here, with XRD in (a) showing 100% crystallinity and TEM micrograph in (b) showing an average grain size of 66nm.

rests quickly whether or not a second phase forms, and at lower temperature, the nanostructure can potentially be maintained. Extended annealing experiments were carried out to further explore the viability of these alloys.

2.4 PHASE TRANSFORMATION KINETICS

The phase transformation kinetics were studied in these alloys via DSC. Since the amount of grain growth is small, it is assumed that the DSC peaks here solely come from the heat released by Al_6Mn precipitation. By integrating the peak and studying the fractional heat evolution, it is possible to track the fraction transformed over time. Transformation kinetics can reveal details such as activation energy, reaction rates, reaction order, and even reaction mechanism. For example, the semi-empirical Kissenger-type analysis [60, 67, 68, 69] is widely used to extract activation energy from various reactions, and the growth equation proposed by Lifshitz *et al.* [70] has been frequently applied to diffusion controlled precipitation reactions. This kind of analysis usually requires measurement of a specific transformation temperature under different heating rates, which can be problematic when multiple reactions take place simultaneously, where the extraction of the exact reaction temperature becomes challenging. More, aside

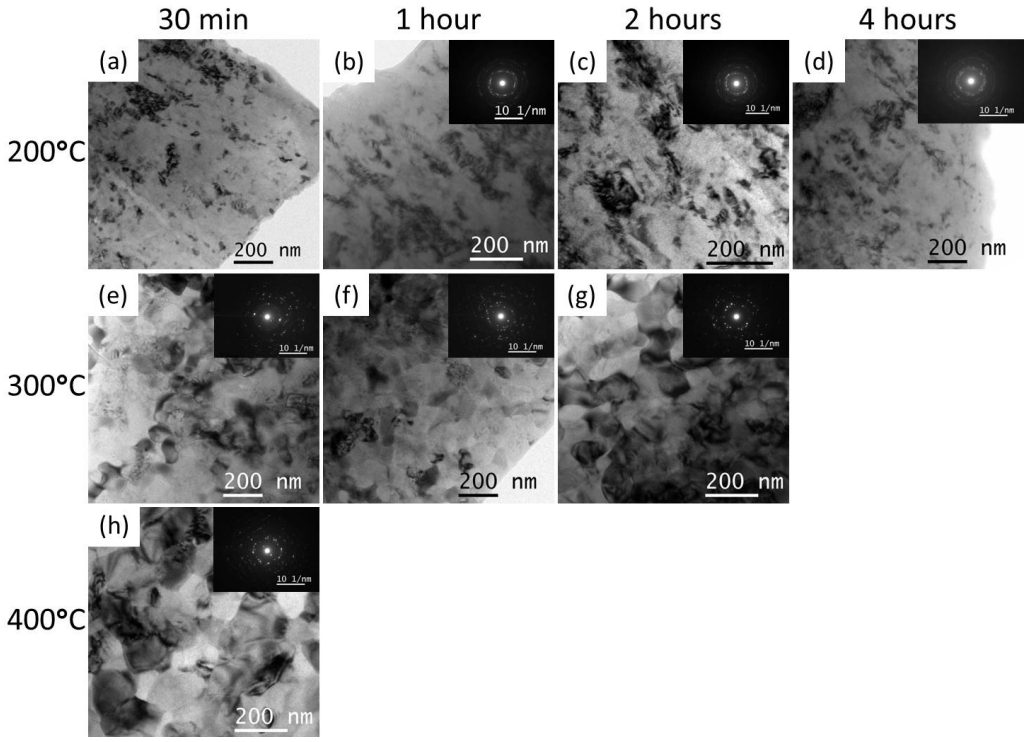

Figure 10: The TEM micrographs of Al-Mn electrodeposits annealed at different conditions. (a) to (d) are samples annealed at 200°C for 30 minutes, 1 hour, 2 hours, and 4 hour. (e)(f)(g) are sample annealed at 300°C for 30 minutes, 1 hour, and 2 hours. (h) is the sample annealed at 400°C for 30 minutes. All the micrographs are at same scale, it's worth noting that the samples annealed at 200°C doesn't show a significant grain growth, nor does it show evidence of phase transformation. However, for samples annealed at 300 and 400 °C, the intermetallic forms within 30 minutes of annealing. Interesting, for the 300°C samples annealed at 2 hour, the microstructure doesn't change as well.

from the activation energy, there are other parameters such as growth index as well as reaction rate constants, which can be valuable for kinetic analysis. Due to the complexity of the system, in which not only the activation energy but also other reaction factors are all of interest, the most general solid state reaction model, the JMAK model is used in this study. JMAK was first proposed in 1939[71, 72, 73, 74], and has become the most commonly used reaction kinetic model in solid state transitions. It has been used successfully in multiple cases such as crystallization[75, 76, 77, 78, 79, 80] and precipitation[81, 82, 83, 84,

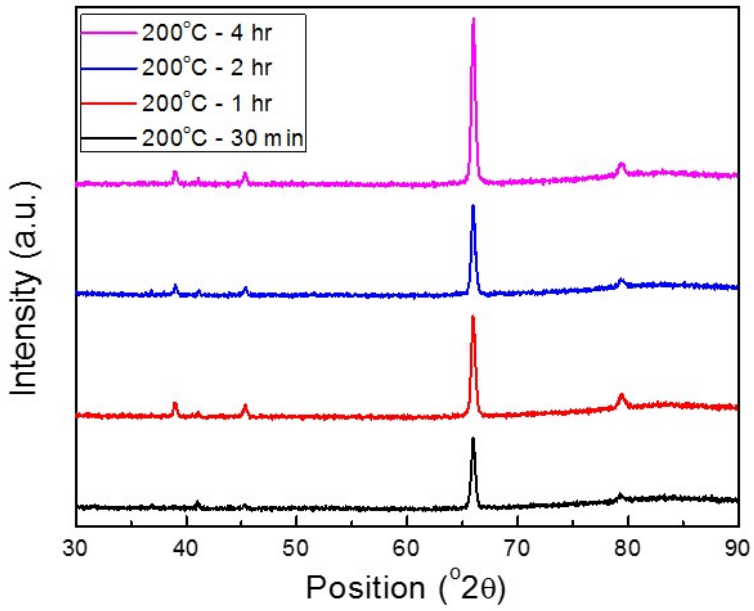

Figure 11: The XRD results of Al-Mn monocrystalline nanostructure annealed at 200°C at different time, showing there is no significant formation of intermetallic phase even at 4 hours of annealing.

85]. The JMAK equation was originally derived under simplifying assumptions: isothermal conditions, homogeneous nucleation, and a single reaction step processes. However, subsequent adaptations of the JMAK equation have enabled it to be applied to non-isothermal cases, for which both analytical and numerical methods have been developed[76, 84, 86, 87, 88]. In this study, the analytical solution developed by Mittemeijer *et al.*[88, 89, 90] is adopted to develop the reaction kinetic model for the Al-Mn system due to its simplicity and its clear physical meanings of the fitting parameters.

2.4.1 *Data Fitting Model*

For the single-phase nanocrysatlline specimen of Figure 9, the reaction is a single reaction process, and traditional JMAK methods apply. The relationship between the true transformed volume V_t, the total sample volume V, and the "extensive

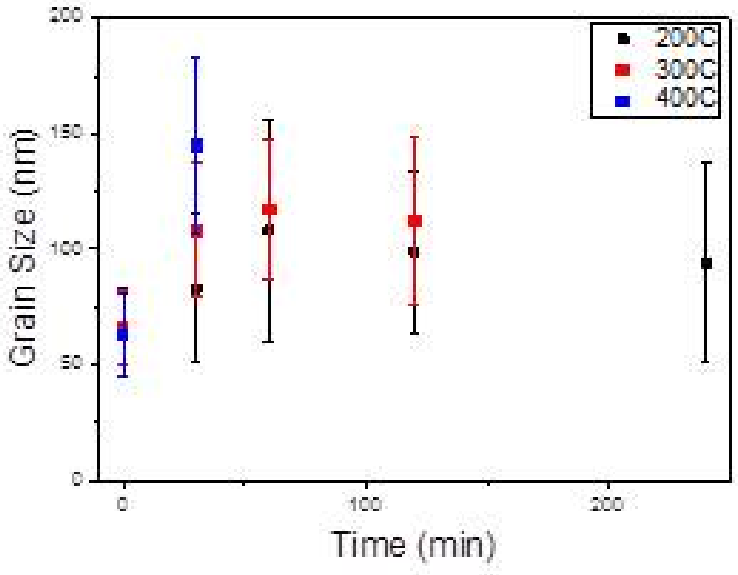

Figure 12: The average grain size measured using the set of micrographs in Figure 10, with the grain size for the samples annealed at 200°C stabilized at around 100 nm. For the 300° sample, the grain size stabilized at around 110 nm.

volume" V_e, which is the representation of the transformed volume that would exist if there were no impingement or constraints on the transformation, is described as

$$dV_t = \frac{V - V_t}{V} dV_e \tag{2}$$

Mittemeijer *et al.* presented the solution to Equation 2 for both isothermal and isochronal (constant heating rate) conditions, written respectively[88, 89, 90]:

$$f = 1 - \exp(-\frac{V_e}{V}) = 1 - \exp\left(-k^n t^n \exp(-\frac{nQ}{RT})\right) \tag{3}$$

and

$$f = 1 - \exp(-\frac{V_e}{V}) = 1 - \exp\left(-k^n (\frac{RT^2}{b})^n \exp(-\frac{nQ}{RT})\right) \tag{4}$$

where f is the fraction of the specimen that has transformed, t is the annealing time in an isothermal process, and b is the heating rate in a constant ramping rate

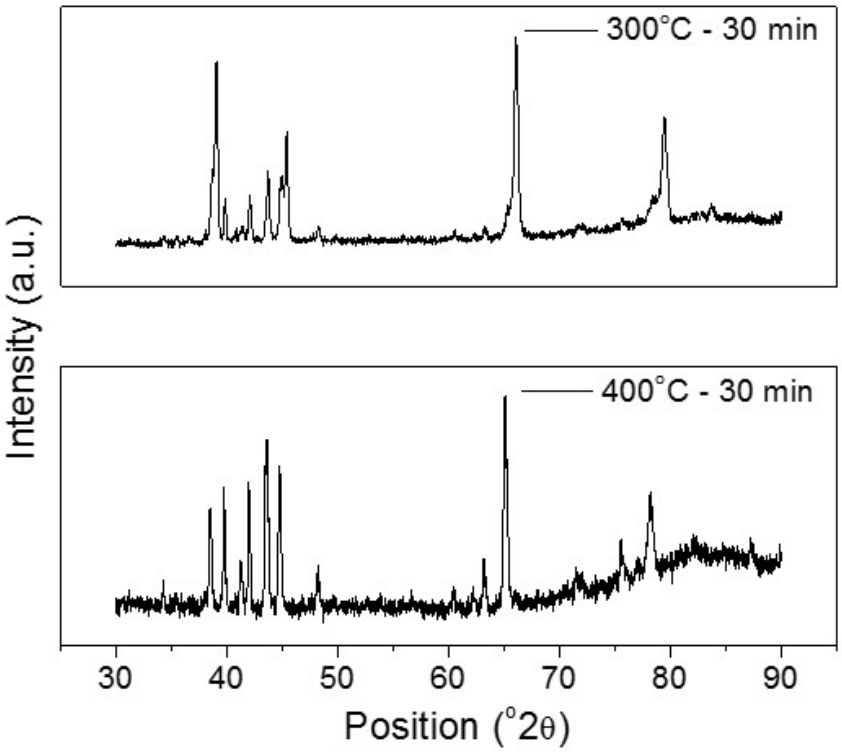

Figure 13: The XRD pattern showing that for samples annealed at 300 and 400 °C, the intermetallic forms within 30 minutes.

experiment (isochronal). In either case k is the reaction constant, n is the growth exponent, Q is the activation energy, T is temperature, and R is the gas constant. The quantities k, n, and Q are characteristic of the reaction in question, and have different effects on the transformation kinetics. For instance, an increase in Q and decrease in k suggest that the reaction is slow and usually happens at higher temperature; an increase in n shows that the peak height is increased. The DSC peak can be described as

$$\frac{dH}{dT} = \Delta H \frac{df}{dT} \tag{5}$$

where $\frac{dH}{dT}$ is the heat flow observed in the experiment under a non-isothermal condition, and ΔH is the total heat released (the area of the DSC peak) for the reaction.

2.4.2 *Data Fitting Results*

The background of DSC heat flow data was subtracted, and the remaining signal curve was interpolated using a custom MATLAB program to make sure that each dataset had the same number of data points. This step ensured that the data was weighted uniformly for unbiased fitting. A MATLAB program was then used to fit the DSC data with Equation 4 substituted into Equation 5. The fitting result is shown in Figure 14, and is quite satisfactory with $R^2 = 0.98$. Three different heating rates from 5 to 15 °C/min are shown, and the three different conditions are fitted with the same reaction kinetics, i.e. the same activation energy, reaction constant, and growth index. The activation energy is fitted as Q = 126.9 kJ/mol, which is reasonable compared with the literature values for the activation energy for Al_6Mn precipitation and the activation energy for Al diffusion, which ranges between 80 and 167 kJ/mol by Ciavagura *et al.* and Luiggi *et al.*[7, 8, 9, 10].

The extracted growth index was n = 1.6. The growth index n is defined as

$$n = \frac{d}{m} + c \tag{6}$$

in which d is the dimension. For m = 1, the reaction is governed by a interface controlled process, while m = 2 means reaction is governed by a diffusion controlled process. The nucleation constant c ranges from 0 to 1, where 0 means no pre-existing nuclei and 1 corresponds to site saturation condition. The definition of the growth index n in this model for a three dimensional case is shown in Table 2.

In the single-phase nanocrystalline Al-Mn alloy, the kinetic factor n = 1.6 suggests that the intermetallic precipitation of Al_6Mn is a 3 dimensionally diffusionally limited process. The reaction constant is k = 99.2 s^{-1}, which was treated as a constant in the analysis across different temperatures. However, k is actually a combination of different pre-factors including nucleation, growth of product phase, as well as collision between atoms, which can be temperature dependent and should be considered as temperature dependent if doing isothermal analysis.

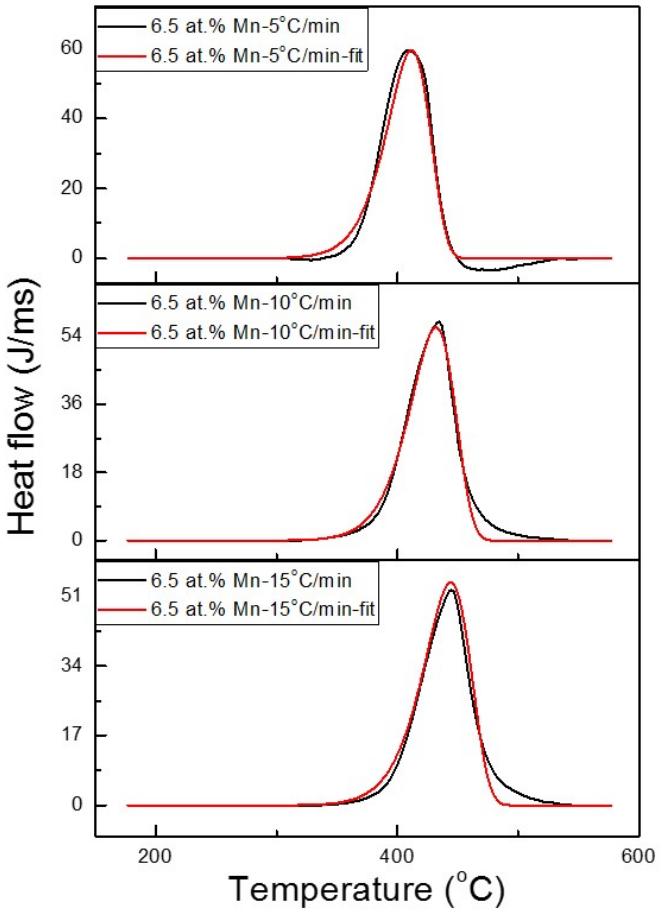

Figure 14: The DSC data was fitted with JMAK analytical solution. The experimental results of three different ramping rates from 5 to 15 °C/min were shown here. From this fitting, the activation energy, reaction constant, and growth index can be calculated.

Table 2: The meaning of growth index n in 3 dimensional process (d=3).

Mechanism	n Value
Interface Controlled Process	$3 \leqslant n \leqslant 4$
Diffusion Controlled Process	$1.5 \leqslant n \leqslant 2.5$

2.4.3 *Construction of a TTT Diagram*

With the information extracted from the DSC data fitting, a conventional time-temperature-transformation (TTT) diagram can be constructed. The exothermic peak here can be seen as a complete reaction, and at each temperature/time point, it reflects the progress of the reaction. To construct the TTT diagram, the isochronal analytical equation is used. A schematic of how the TTT diagram is constructed is shown in Figure 15.

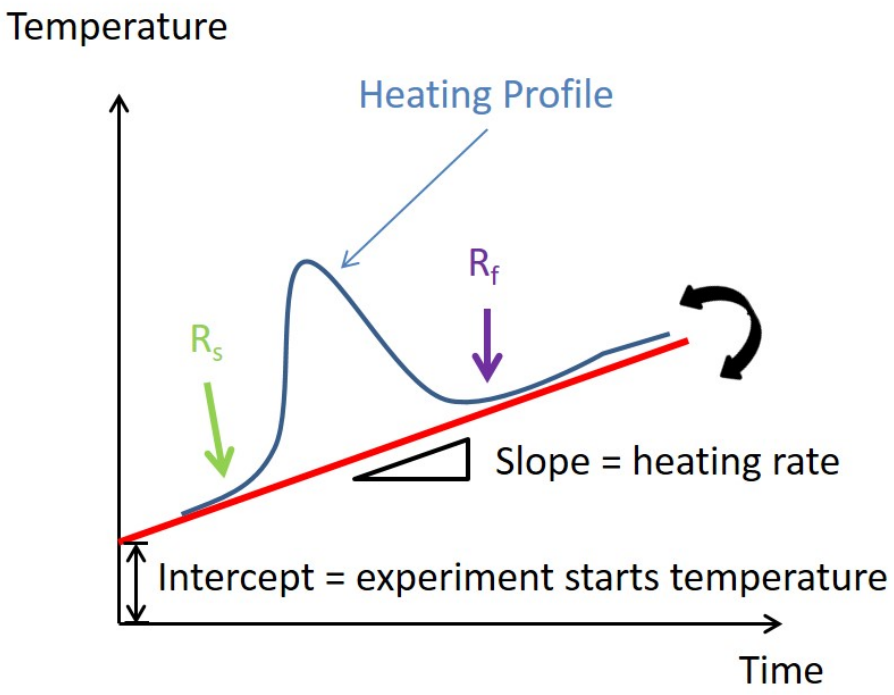

Figure 15: In the time and temperature space, for each heating profile, a reaction start and a reaction finish time can be calculated. By changing the heating rate, different reaction start and finish points can be acquired. Connecting the start/finish points at various heating rates, the TTT diagram is constructed.

The TTT diagram constructed is between 27 to 627°C (300 to 900K, note that the melting temperature for Al is 660°C, (933K)), which is mostly covered by the isochronal annealing studies. The resulting TTT diagram is shown in Figure 16.

From the calculated TTT diagram, we can see that at room temperature, the time for the precipitation reaction to start is nearly infinite, however, at a higher

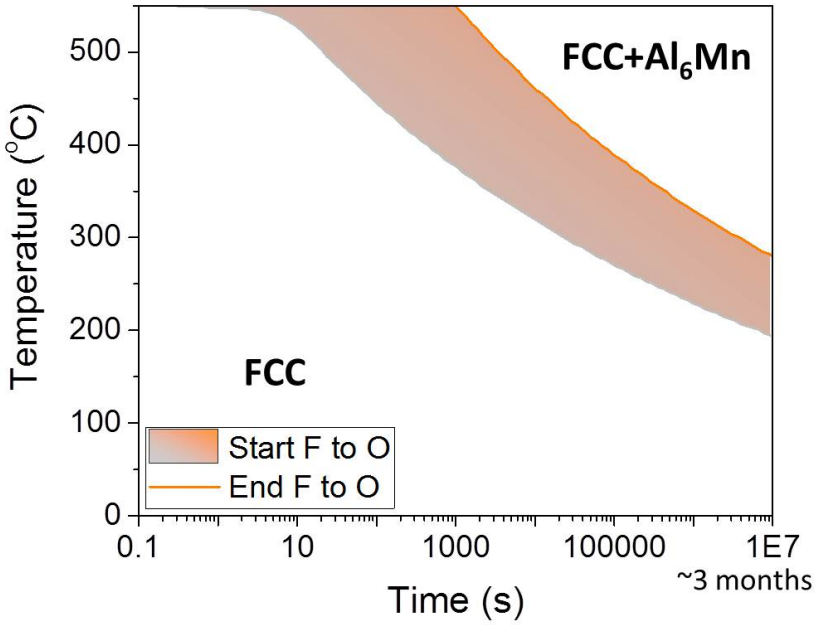

Figure 16: The TTT diagram constructed using the parameters acquired from the DSC fitting in Figure 14. F is the notation for FCC and O is the notation for Al_6Mn. The start and finish of the reaction are marked. Note that at T = 400°C, the intermetallic formation starts within 30 minutes as suggested in the experiments. At 200°C (T = $0.5T_H$), the system is free from transformation for at least 3 months from the TTT diagram.

temperature close to the melting point of the alloy, the intermetallic forms quickly when annealing starts. At around 200°C, which is half of the melting point of pure Al (473K compared to 933K, half of the homologous temperature), the TTT diagram also predicted that the formation time for the Al_6Mn phase is greater than 3 months. This study shows that at moderate temperature, the alloy might be able to have stabilized structure over a long period of time. In the following section, the accuracy of this TTT diagram will be examined.

2.5 EXTENDED ANNEALING

As mentioned before, the samples annealed at 200°C for 4 hours were able to maintain nanocrystalline structure with only a slight relaxation of grain size in the first 30 minutes of annealing, with no intermetallic formation. However, for the 300 and 400°C samples, the intermetallic formed within 30 minutes and the grain sizes were slightly larger than the samples annealed at 200°C. The dark field images were used to quantify the grain size at different annealing conditions, the average grain size for each annealing condition is shown in Figure 12. To extend these observations, additional samples were annealed at 200 and 300°C (for which the homologous temperature is 0.5 and 0.6 respectively) for one month, as shown in Figure 17 and Figure 18. In the TEM micrographs, the grain size after annealing for 1 month at 200°C is still 99 nm for the sample annealed at 200°C and 110 nm for the sample annealed at 300°C, showing that the structure can resist drastic coarsening at high temperature when the intermetallic phase forms. Especially for the sample annealed at 200°C (homologous temperature = 0.5), neither phase transformation nor grain coarsening were observed, showing that it is indeed a stabilized structure and can be of engineering use at elevated temperatures.

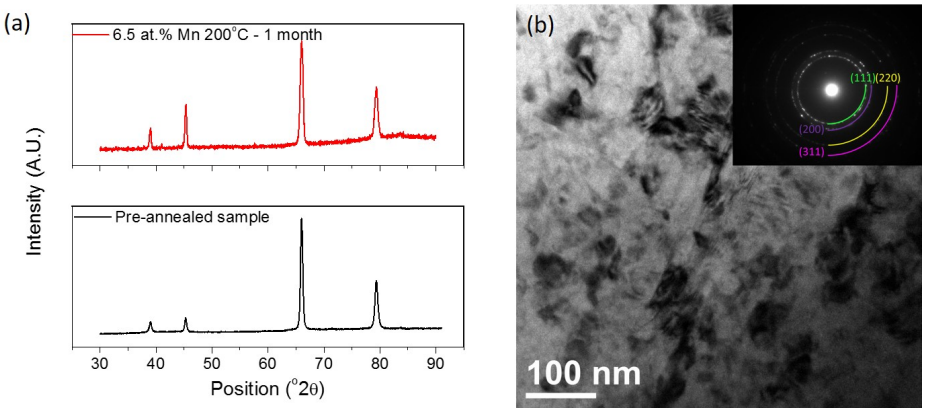

Figure 17: The (a)XRD and (b)TEM of monocrystalline 6.5 at.% Mn sample annealed at 200°C for one month. The TEM graph shows that the grain size is still able to maintain nanometer range and the XRD shows there are no siginificant formation of Al_6Mn intermetallic phase.

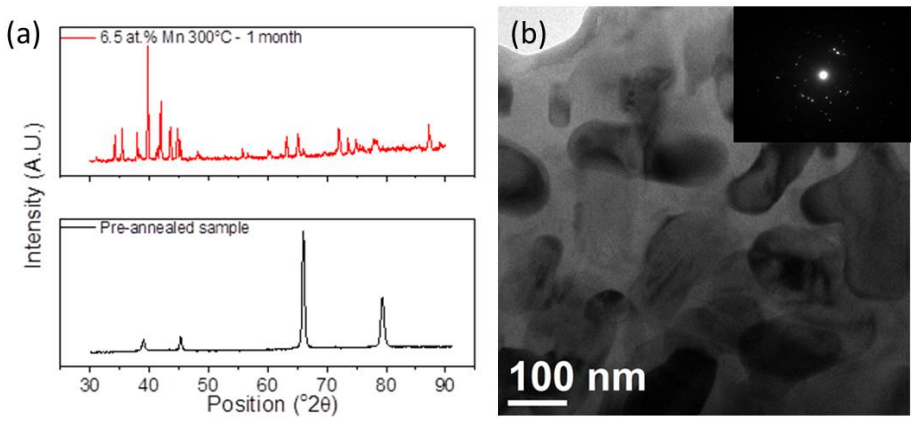

Figure 18: The (a)XRD and (b)TEM of monocrystalline 6.5 at.% Mn sample annealed at 300°C for one month. Unlike the structure in Figure 17, the sample shows large amount of Al_6Mn intermetallic phase, and the TEM also supports the XRD result.

2.6 CONCLUSIONS

In this chapter, the basic microstructures of electrodeposited Al-Mn alloys were explored. Holding all other control variables constant, the grain size has been shown to decrease with an increase in Mn concentration, eventually reaching an amorphous phase. The microstructure evolution including grain growth and phase transformation were then studied thoroughly for one specific composition namely Al-6.5at.%Mn, which is a single-phase solid solution alloy with a 65 nm grain size in the as-deposited condition. The precipitation reaction to form the intermetallic compound Al_6Mn has been identified as a three dimensional diffusion controlled process in single-phase Al-Mn nanocrystalline alloy, with an activation energy of 127 kJ/mol.

Instead of sticking to the basic analysis of qualitative studies on the kinetics, the thesis takes a step forward to using these parameters to construct the TTT diagram based on the JMAK analysis. Through extended annealing experiments, the calculated TTT diagram has been further verified and a simple and effective way to for TTT diagram construction has been demonstrated. At 200°C, which is half of the homologous temperature of pure Al, it has been shown experimentally that the structure can maintain a nanostructure after at least a month of anneal-

ing, without significant formation of intermetallic phases, which makes the alloy viable for many engineering processes. The TTT diagram further predicts that the alloy can sustain longer annealing times for at least 3 months without formation of intermetallics at 200°C.

At an even higher temperature of $0.6T_H$, intermetallics form rapidly but the grain size is still able to remain on the nanoscale even after prolonged heat exposure. Such nanostructure stability may unlock the potential of moderate temperature application of this particular nanocrystalline material.

3

NANOSTRUCTURE STABILIZATION MECHANISM

In Chapter 2, the stability of nanostructred Al-Mn has been established, and in particular the stability of single-phase FCC Al-6.5at.%Mn at 200°C is quite noteworthy with a stable grain size in the nanoscale for months. Moving forward, it would be helpful to understand the stabilization mechanism. In this chapter, by looking into the grain boundary chemistry, segregation of Mn is identified as playing a role in stabilization. Furthermore, the grain boundary segregation energy is discussed based on a thermodynamic model to compare with the experimental results.

Note: The contents of this chapter have been published in Ref. [91], with coauthors Christopher J. Marvel, Patrick Cantwell, and Martin P. Harmer who contributed the aberration corrected STEM analysis in this work.

3.1 GRAIN BOUNDARY CHARACTERIZATION

The materials synthesis was the same as described in Section 2.1.1. For this chapter, a nanocrystalline sample with 6.7 at.% Mn was selected. The basic material characterization methods are as described in Section 2.1.2.

For a more detailed analysis of grain boundary structure and solute distribution, aberration-corrected scanning transmission electron microscopy (Cs-STEM) was used in this study. STEM samples were prepared via the in-situ lift-out method in a FEI DB235 focused ion beam (FIB) and final polishing was completed to remove the amorphized damage layer in a Fischione 1040 NanoMill. STEM analysis was conducted in a JEOL JEM-ARM200CF at 200 kV using bright field (BF) and high-angle annular dark field (HAADF) imaging. EDS line scans were performed with a JEOL 100-mm^2 x-ray detector. Prior to analysis, an SPI plasma cleaner was employed to remove excess carbon from the sample surface.

The line scan experiments from Cs-STEM, provide one dimensional information of the solute concentration variation. Atom probe tomography (APT), which

provides a three dimensional information was also employed for this study. APT has been used extensively to study the interface and grain boundary properties due to its chemical and spatial sensitivity[92, 93, 94]. For instance, it has been used to study P segregation in the Ni-P system[95, 96], in Ti-Al-N thin films[97] and Nb microalloyed steel[98].

A variety of atom probe samples were prepared by FIB lift-out process with a combination of pyramid milling and annular milling as described in [97, 98, 99, 100, 101, 102, 103] to reduce the Ga implantation. In order to characterize the sample using TEM prior to destructive APT experiments, a special sample holder was prepared by cutting a 100 mesh molybdenum TEM grid in half, and etching with concentrated potassium hydroxide solution under 5 V AC to dissolve the crossing bars and allow a neck to form. Mo was chosen due to its high work function, which can sustain the high voltage pulse inside the APT. Inside the FIB, the tips were further milled to form a plateau at the top. The lift-out procedure was conducted with a FEI Helios FIB operated using a Ga ion source at 30, 16, 8, and a 5 kV final cleaning step to remove the amorphous layer. The sample tip diameters ranged from 50 to 80 nm. Tips were observed with the JEOL 2100 TEM to study the tip geometry and structure for better reconstruction. The sample preparation using FIB is shown in Figure 19.

The atom probe tips were analyzed using a CAMECA LEAP 4000X HR instrument operated under voltage mode with a pulse fraction ranging from 15 to 18% and pulse repetition rate of 200 kHz at 50K. The datasets acquired by APT ranged from 3 to 34.5 million atoms. Data analysis was conducted using IVAS software for reconstruction and the results were output for further analysis by custom algorithms coded in MATLAB.

3.2 GRAIN BOUNDARY STRUCTURES

3.2.1 *Basic Characterization*

To examine the grain boundary segregation behavior in the Al-Mn system, grain boundary structure and chemical signatures were obtained from the grain boundary and grain interiors. The single phase nanostructured sample was first studied with XRD and TEM to ensure the grain size and crystallinity. Here, the sample has

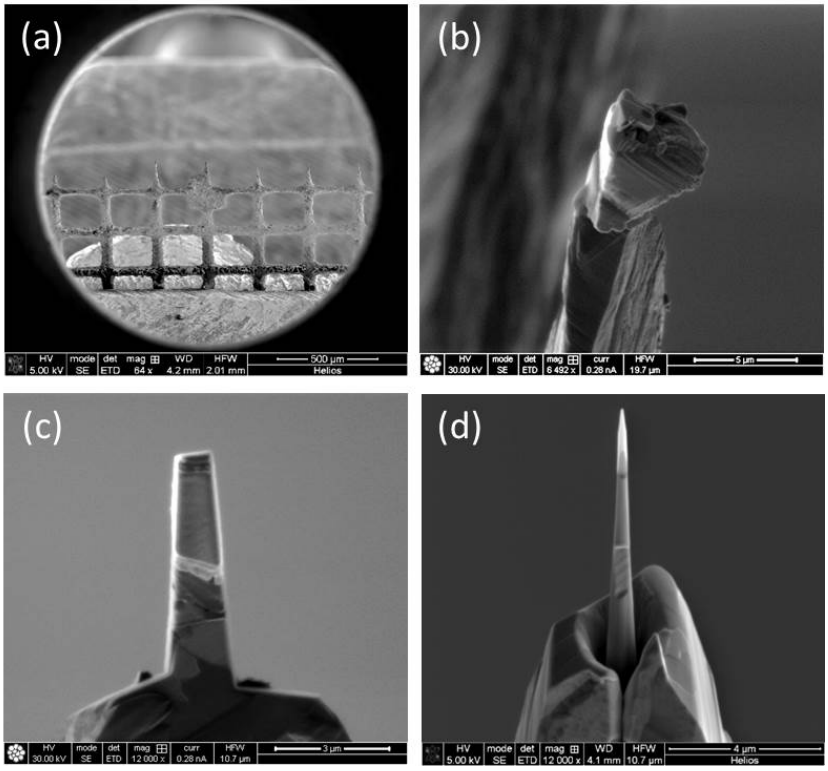

Figure 19: (a) The half Mo grid used as APT experiment posts in FIB (b) The wedge of sample cut out by FIB welded using pyramid milling (c) The initial milling of the sample and (d) The final APT tip for experiment

a grain size around 160 nm, with the microstructure and XRD diffraction pattern shown in Figure 20 and grain size statistic shown in Figure **??**. The average grain sizes were calculated with both TEM dark field images as well as XRD Rietveld refinement.

3.2.2 *Aberration-corrected STEM*

In the Cs-corrected STEM analysis, the BF and HAADF images seen in Figure 22 demonstrate the typical appearance of two adjacent grains for the as-deposited state. The grain boundaries are marked with yellow arrows. The increased intensity along two boundaries, seen in Figure 22, suggests there is a local increase of average atomic number. Thus, in this alloy, the increased intensity is likely Mn segregation because of Mn has a higher atomic weight compared to aluminum.

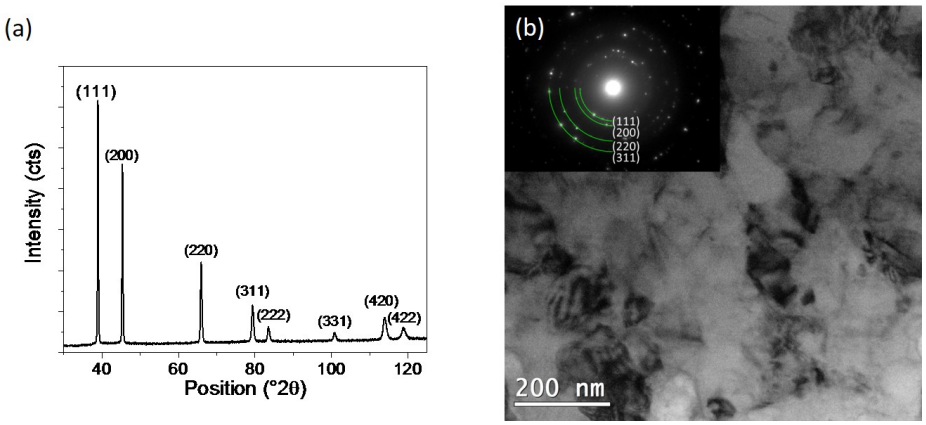

Figure 20: Structural characterization of the as-deposited Al-Mn alloy film by (a) XRD and (b) bright field TEM. (a) shows that the material is Al FCC crystalline phase. (b) shows the grain size (in plan view) is about 162 nm on average, and the inset selected area diffraction (SAD) pattern conforms to a single phase FCC structure.

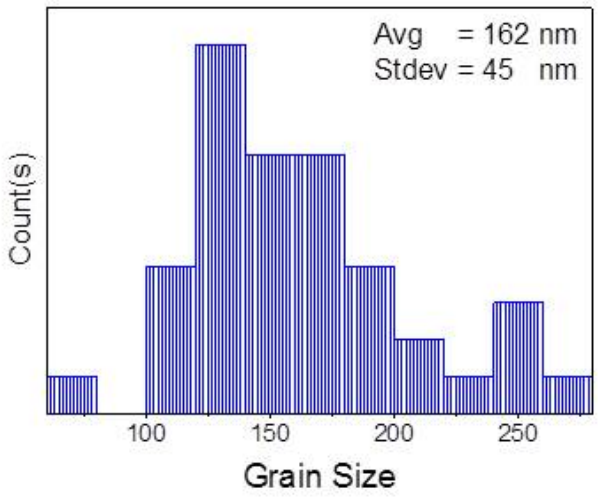

Figure 21: The grain size statistic of this particular sample for the grain boundary property studies.

Unfortunately, Mn-enrichment is typically not as evident at higher magnifications, as seen in Figure 22(c) and Figure 22(d), in which the atomic contrast is not obvious and the grain boundary is really diffuse. Note that the grain boundary

structure at higher magnification shows a high angle and diffuse grain boundary, also, the grain boundary thickness is thicker than is typical in metals (1 nm). The diffuse grain boundaries might be an indication of amorphous phase formation at higher Mn concentration.

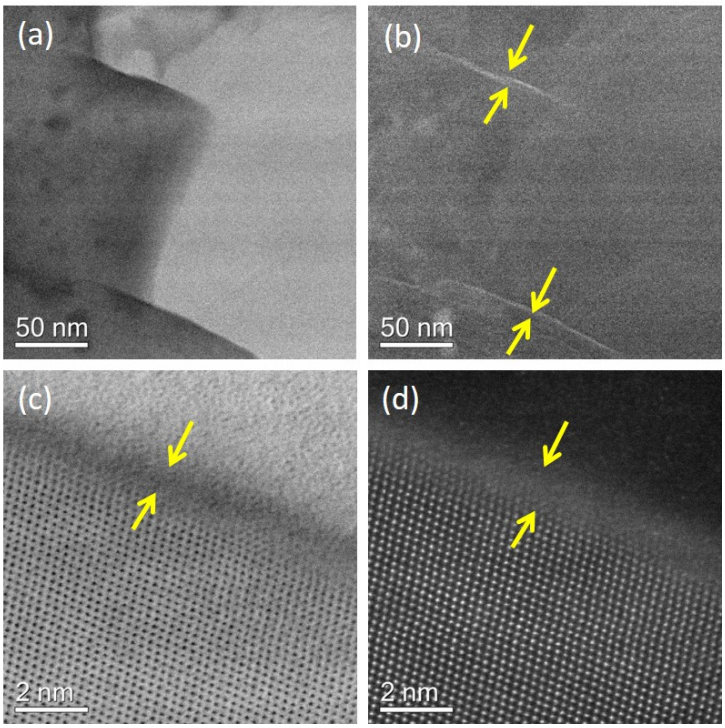

Figure 22: Images of typical grain boundaries under Cs-corrected STEM. The low magnification BF image (a) depicts two adjacent grains and low magnification HAADF (b) shows the two grain boundaries exhibit Mn segregation. Images (c) and (d) are high magnification BF and HAADF, respectively.

Because the atomic contrast was not clear in the high magnification HAADF STEM, direct chemical analysis was needed. A concentration profile across another such grain boundary is shown in Figure 23. The Mn and Al concentrations, calculated to 2σ error, are determined using the Cliff-Lorimer equation, which states that the weight ratio between the two atomic species in a thin specimen can be approximated with the intensity acquired in an EDS scan[104, 105]:

$$\frac{C_A}{C_B} = K_{AB}\frac{I_A}{I_B} \tag{7}$$

In which C_A and C_B are the weight fractions of the individual species, I_A and I_B are the peak intensities after background subtraction from EDS, and K_{AB} is the Cliff-Lorimer factor for elements A and B, which is determined experimentally using standard samples with known concentration. Here, the K_{AB} factor was determined by substituting the global concentration as the grain interior concentration. The Mn content reaches a maximum of approximately 14 at.% at the grain boundary, as compared to an average of 7 at.% in the grains, and confirms that the high intensity in HAADF is Mn segregation.

However, in normal cases, it is hard for EDS line scans to provide absolute interfacial compositions because of grain boundary inclination. To more accurately measure the Mn-enrichment, and eliminate the effect of boundary inclination, the scan-width method was used to determine extent of Mn segregation via Equation 8[106].

$$ML_{S_A} = N_B^{1/3} \times \frac{I_A}{I_B} \times w \times k_{AB} \tag{8}$$

where ML_{S_A} is the number of Mn solute atoms per monolayer, N_B is the atom number density of the Al matrix, I_A and I_B are the EDS intensities of the Mn and Al, and w is the EDS scan width perpendicular to the grain boundary[106]. $N_B^{1/3}$ is determined by taking the area density of the most densely packed plane, which is {111} for FCC Al. Equation 8 gives a Mn area density of 4.2±0.2 atoms/nm^2 and 2.6±0.1 atoms/nm^2 on the grain boundary and grain interiors based on the Mn counts in Figure 23(c). Thus, the difference of approximately 1.6 atoms/nm^2 represents the excess of Mn on the grain boundary. Because the sample thickness is unknown, an effective scan width was not utilized to eliminate the effect of beam broadening. The line profile and scan width results are in good agreement as one technique estimate 50% enrichment of Mn on the boundary and the other yields 60% at the grain boundary.

In addition to the results seen in Figure 22 and Figure 23, several more individual grain boundaries were surveyed; grain boundary segregation is clearly observed in most but not all of these. In light of the broad spectrum of different grain boundary characters that might be sampled in a polycrystal, it is reasonable that a variety of different responses are observed. This variety will be discussed further later.

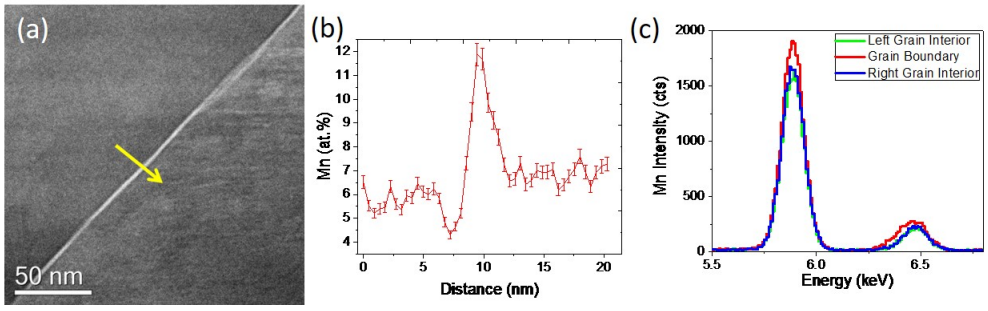

Figure 23: An EDS composition line scan in Cs-corrected HAADF STEM (a) shows an increase in Mn concentration (at.%) at a grain boundary, which is imaged in (b). The start and finish direction of the scan is marked with the yellow arrow in (b). The average concentration of the line scan is 6.9 at.%, and the concentration at the boundary is about 10.5 at.% on average. (c) shows the scan at the same grain boundary using the area density method, with the Mn counts for right grain, left grain, and grain boundary plotted. By overlaying the curves, one can see that at the grain boundary, the Mn counts are higher.

3.2.3 *Three Dimensional APT*

An atom probe tip and the corresponding reconstructed atom dot maps are shown in Figure 24, where several grain boundaries that appear to span the sample are captured. A line scan with a block size of 1.8 by 1.8 nm^2 (with $n \simeq 200$ atoms) along the axial direction (z direction) was carried out. Mn concentrations along this direction which exceeded two standard deviation of the average concentration are marked; their positions are indicated by green arrows in Figure 24. Their corresponding locations are also marked in the TEM image in Figure 24(a). The Ga distribution Figure 24(c) also aligns with the Mn distribution and coincides with the grain boundary positions in the TEM micrograph; as suggested in Ref.[53], Ga from the APT sample preparation process is an effective marker of grain boundary positions in APT of aluminum. Taken together, the above results positively identify several individual grain boundaries, and confirm that Mn is located preferentially at them.

With the knowledge of grain boundary positions, the reconstructed data was examined with line scan across grain boundary sites using the ladder diagram method[93, 107], which is similar to line scan in aberration-corrected STEM but using a cumulative calculation to give better statistics. Quantitative analysis us-

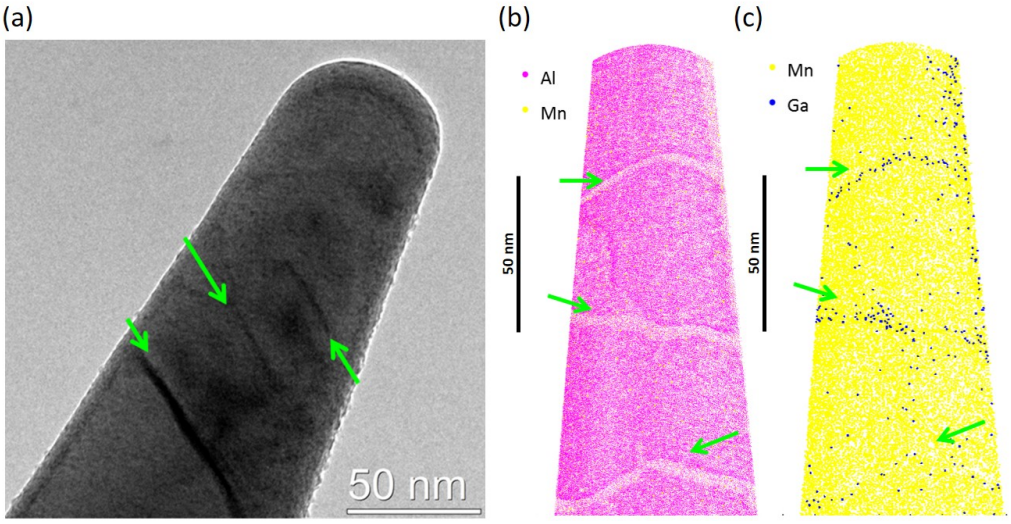

Figure 24: (a) TEM picture of an APT sample. Green arrows mark the position of three individual grain boundaries. (b) The atom dot maps of Al and Mn and (c) Mn and Ga for the same sample.

ing ladder diagram is carried out as shown in Figure 25, which includes several parallel profiles across the same grain boundary at different positions, each 1.8 by 1.8 nm^2 in cross section. A ladder diagram is a cumulative presentation of solute content along a one-dimensional line, plotting the number of solute atoms encountered as a function of the total number of atoms encountered. Such ladder diagrams have been extensively used for identifying different phases as well as clustering in APT data[93, 107, 108]. The slopes of these ladder diagrams are indicated in Figure 25, and represent the local concentration; in every case there is a clear signal of Mn segregation at the grain boundary. The amount of grain boundary segregation ranges from 3 to 6 at.% higher than the composition in the neighboring grains, which agrees with the finding in Cs-corrected STEM analysis.

To get better statistics on the grain boundary and grain compositions, 180 ladder diagrams were constructed and analyzed such as those of Figure 25, to assemble composition distributions unique to the boundaries or the grains. The result is shown in Figure 26. Figure 26(a) shows how the sampling was conducted, and (b) shows a histogram of Mn concentrations at the grain boundaries and a histogram in the grain interiors; the grain boundary is indeed enriched in Mn. Figure 26(c) shows a cumulative probability plot of the difference between grain boundary

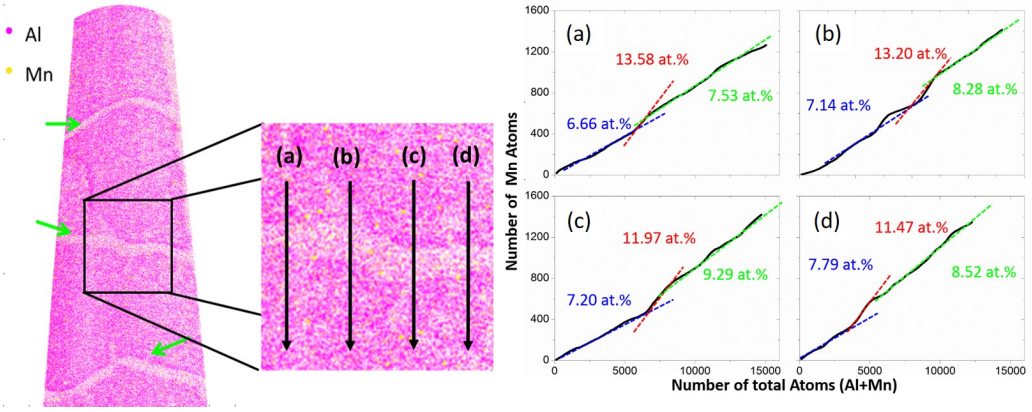

Figure 25: Ladder diagram analysis of an individual grain boundary on the atom probe sample. Each line here represents a one dimensional 30 nm scan across the marked grain boundary, with an $1.8 \times 1.8\ nm^2$ cross sectional area. The x axis is the cumulative total (Al+Mn) number of atoms while the y axis is the accumulated number of Mn atoms encountered in a one-dimensional traverse across the boundary. The slopes marked here represent the Mn concentration for each scan. The slopes all change across the grain boundary. (The blue dashed line and green dashed line show the concentrations for grain interiors, and the red dashed line denotes the region of higher slope that corresponds to the grain boundary.) The grain boundary is enriched by about 6.92 at.% Mn in line (a), 6.06 at.% in line (b), 4.77 at.% in line (c), and 3.68 at.% in line (d) as compared with the background level in the grains.

and grain interior sites on individual ladder diagrams, which suggests a median enrichment of Mn at boundaries of about 3 at.%.

The APT data can also be analyzed by dividing the sample into small blocks for statistical testing by binomial fitting. If a sample were a perfectly random solution, the frequency distribution of the composition when measured many times in small blocks would be binomial[109]. Individual samples were divided into many blocks with $n \simeq 200$ atoms inside each to obtain the composition distribution. Regions containing edges of the sample and crystallographic poles, where the density of atoms is lower, are avoided to prevent distortion of the data statistics. The binomial distribution describes a probability density $P(c)$ at concentration c as

$$P(c) = \frac{1}{\sigma\sqrt{2\pi}} \exp\left(\frac{-(c - c_0)^2}{2\sigma^2}\right) \tag{9}$$

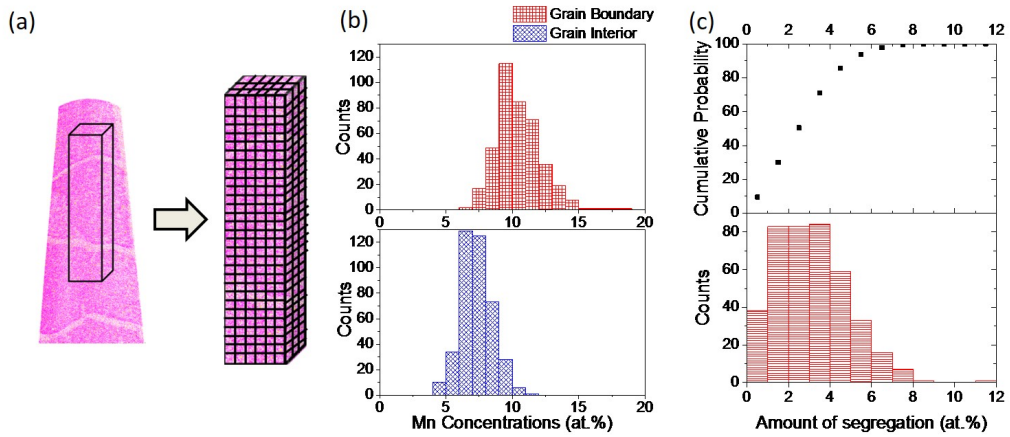

Figure 26: A schematic of how sample was divided was shown in (a), and the concentration distributions for regions in the grain boundary and grain interior of an APT sample are shown in (b). The average grain boundary concentration is 10.5 at.% Mn and the average concentration of the grain interior is 7.3 at.%. The degree of segregation (concentration difference between grain boundary and grain interior) is also plotted with a cumulative probability plot and histogram are shown in (c). The average degree of segregation is 3.1 at.% Mn for this grain boundary.

where c_0 is the average concentration of the whole sample, c is the concentration of individual blocks, and the width normalization is given by $\sigma^2 = c_0(1 - c_0)/n$. The binomial equation involves only a single fitting parameter, namely the average solute concentration. If the data show a deviation from the single-variable fitting curve suggests a non-random solute distribution. Equation9 can be fitted to the experimental data of Figure 27 as shown in red. The fit is significantly different from the shape of the data, which exhibits skew to higher concentrations. Such skew is what would be expected if there were a minority of sites of higher-than-average composition, i.e., if there were selective segregation of solute to some regions in the sample (grain boundaries).

Since the sample may therefore better be described as a combination of two different regions (grain interiors and grain boundaries), each of which is a random solution at its own composition, the data were fitted with a two-binomial distribution as

$$P(c) = \frac{f_{gi}}{\sigma\sqrt{2\pi}} \exp\left(\frac{-(c - c_{gi})^2}{2\sigma_{gi}^2}\right) + \frac{f_{gb}}{\sigma\sqrt{2\pi}} \exp\left(\frac{-(c - c_{gb})^2}{2\sigma_{gb}^2}\right) \quad (10)$$

in which the subscript gi denotes the grain interior and gb denotes the grain boundary regions, each present in their own volume fraction, f and at separate compositions, c.

The binomial-binomial fit of Equation 10 to the data of Figure 26 is also shown in Figure 27, along with the sub-distributions corresponding to each region. The fit reveals an average grain interior concentration of 7.5 at.% (dotted blue line) and an average grain boundary concentration of 12.6 at.% (dashed blue line). The grain interior concentration is within the error of the bulk Mn concentration measured by SEM-EDS, and the enhancement at the boundary of roughly 5 at.% is reasonably aligned with the results of Figure 26. The grain boundary fraction fitted in the binomial fitting is 12% of the total volume, which aligns reasonably well with a geometric estimate based on iso-concentration surfaces such as shown in Figure 28, which also suggests that grain boundaries comprise roughly 7 to 10 at.% of the sample. Note that in Figure 28, the anomalous region at the top of the analyzed volume is associated with Ga damage near an exposed crystallographic pole, however, this region represents less than 2 % of the total analysis volume. Interestingly, the distributions of grain boundary concentration and grain interior concentration in Figure 26 exhibit some overlap, which allows for the possibility of individual grain boundaries exhibiting little or no solute segregation. This aligns with the Cs-STEM observations described above, where some boundaries but not all exhibited compositional contrast. Since grain boundary segregation is known to depend on the misorientation and boundary plane indices[110], it is reasonable that a survey of a variety of boundaries would reveal a spectrum of responses.

3.3 DISCUSSION

The above characterizations are all consistent with one another, which not only confirm that the as-deposited Al-Mn alloy in this work is a single-phase FCC polycrystal solid solution with a fine grain structure, but also that single phase nanostructured Al-Mn alloy has a subtle but clear enhancement of Mn at the

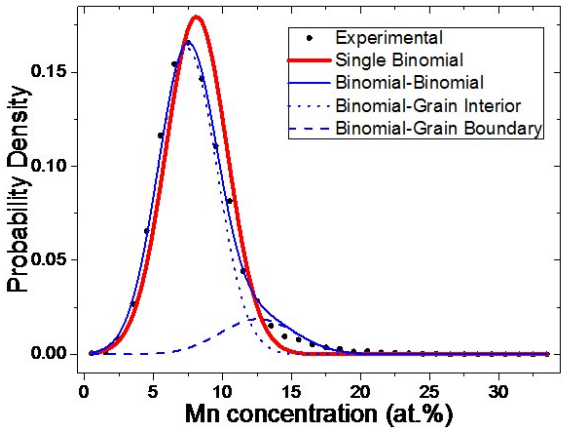

Figure 27: Frequency distribution for one of the atom probe samples with a volume of 36×16×234 nm^3, divided up into blocks containing n = 200 atoms each, and compared with single binomial fitting and binomial-binomial fitting. The black dots show the experimental data frequency distribution. The single binomial fitting (red) significantly deviates from the experimental data, which is broader; suggesting the distribution of solute is not random. The data is further fitted with a dual-binomial function (solid blue line), with sub-distributions shown with dashed lines

grain boundaries of 3 to 5 at.% as compared to the bulk concentration. While there are many different types of grain boundaries, among those examined, each has slightly different segregation behavior, and also different sites within any individual boundary, these results speak to the average, or effective grain boundary segregation behavior.

3.3.1 *Grain Boundary Segregation Energy Calculation*

Grain boundary segregation results from a positive heat of grain boundary segregation of the solute species, i.e., it is a reflection of an energetic preference for solute to occupy grain boundary sites. Were the system assumed to be a solid solution in equilibrium (a significant assumption for electrodeposition due to the driven characteristic of this technique, which we will test shortly), an effective heat of segregation (H_{seg}) can be estimated based on the quantitative STEM and APT composition measurements using the McLean segregation isotherm:

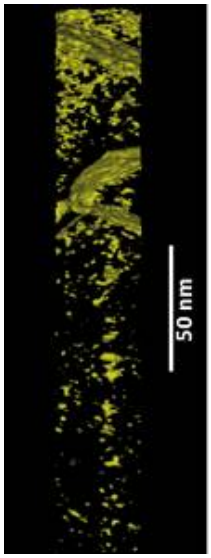

Figure 28: The corresponding iso-concentration surface at c = 10.5% Mn for the volume analyzed in Figure 27

$$\frac{c_{gb}}{1-c_{gb}} = \frac{c_{gi}}{1-c_{gi}} \exp\left(\frac{H_{seg}}{kT}\right) \tag{11}$$

The McLean segregation isotherm was first proposed in [111]. Here the composition subscript gi denotes the grain interior and gb denotes the grain boundary. Taking the relevant temperature to be the processing temperature T = 300K, the H_{seg} values obtained from the experimental results are shown in Table 3, and range from 900 to 1500 J/mol. Such values are very low, suggestive of a weak segregation tendency, which is of course in line with the subtle composition inflation measured.

3.3.2 *Segregation Energy from Thermodynamic-Based Model*

The McLean isotherm mentioned in section 3.3.1 is commonly used for systems at the dilute limit. Although the Al-Mn system under examination has a concentration of 6.7 at.% Mn, it is still in the solid solution form, and using the McLean isotherm to calculate segregation energy is not unreasonable. Reliable grain boundary segregation energies are not generally available for arbitrary alloy pairs, as a result, a Miedema-based thermodynamic model proposed by Murdoch

Table 3: Results of effective heat of segregation H_{seg} extracted from experimental data at room temperature using McLean isotherm analysis. Here, the grain boundary thickness used to calculate the heat of segregation using area density from STEM line scan is assumed as 1 nm.

Experimental Methods	H_{seg} (J/mol)
STEM (line scan)	1254
STEM (area density)	900
APT (line scan average)	1262
APT (binomial fitting)	1420

and Schuh[44] is used to simultaneously estimate the grain boundary segregation energy at the dilute limit to compare with. The segregation energy in the dilute limit ($\Delta H^{seg}_{0,M}$) is estimated using the following equation:

$$\Delta H^{seg}_{0,M} = -0.71 \times \frac{1}{3} \times \nu \times [-\Delta H^{int}_{B in A} - c_M \gamma^S_A V_A^{\frac{2}{3}} + c_M \gamma^S_B V_B^{\frac{2}{3}}] + \Delta E_{el} \quad (12)$$

in which the subscript B denotes solute and A solvent, $\Delta H^{int}_{B in A}$ is the interaction energy (i.e., the bond-level heat of mixing) for a B atom surrounded by A atoms, c_M is a dimensionless semi-empirical constant equal to 4.5×10^8, γ^S is the surface energy for the pure subscripted metal, V is the atomic volume, and $\nu = \frac{1}{2}$ describes the fraction of bonds lost at grain boundaries[112], and ΔE_{el} is the elastic energy term which accounts for the size misfit between the solute and solvent atoms.

The elastic term is based on an Eshelby-type continuum linear elastic formalism for the energy of substituting a misfitting solute atom inside the solvent matrix[113, 114, 115]:

$$\Delta E_{el} = \frac{24\pi K_B G_A r_B r_A (r_A - r_B)^2}{3k_B r_B + 4G_A r_A} \quad (13)$$

Here, K is the bulk modulus, G is the shear modulus, and r is the atomic radius. With this equation and numerical values from Miedema[116], de Boer[117] and James *et al.*[118] (which are all assembled in Table 9), the expected grain boundary segregation energy for Mn in Al can be calculated using Equation 12. In this

analysis, both Miedemaâs original estimate of the system heat of mixing for Mn dissolved in Al ($\Delta H^{int}_{BinA} = -106$ kJ/mol [116]) and the more sophisticated interaction energy from CALPHAD methods with $\Delta H^{int}_{BinA} = -70$ kJ/mol were both used. The calculated Mn grain boundary segregation energy is tabulated in Table 4.

Table 4: Results of effective heat of segregation H_{seg} calculated using Equation 12, the ΔH^{int}_{BinA} are from two different sources: Miedema data and CALPHAD data. The subscript 1 and 2 showing the different sources of the elastic term in Eqaution 13. The calculated values used here including the bulk and shear modulus are shown in Table 9

Enthalpy Data Sources	H_{seg} (J/mol)
ΔH^{int}_{BinA}, Miedema (-106 kJ/mol)[1]	1030
ΔH^{int}_{BinA}, CALPHAD (-70 kJ/mol)[1]	5280
ΔH^{int}_{BinA}, Miedema (-106 kJ/mol)[2]	-5214
ΔH^{int}_{BinA}, CALPHAD (-70 kJ/mol)[2]	-954

If the results in Table 4 are plotted along with the values calculated using the McLean isotherm in Table 3 based on the experimental results, we can see that both the experimental value and the calculated theoretical value have a slight positive segregation energy, suggesting a positive grain boundary segregation phenomenon. However, at the same time, the upper bond and lower bond of the Miedema-based calculated segregation energy has a huge fluctuation around zero between roughly +5 to -5 kJ/mol, which is shown in Figure 29. This might due to the wide difference between the interaction energy (30 kJ/mol for the Miedema calucaltion and the CALPHAD case) and the wide range of differences between the shear and bulk moduli of Mn. To give a better estimation using the model, a more sophisticated study on the thermal data as well as the mechanical property data is needed.

The other interpretation of the differences in the calculated and experimental segregation energies is that the deposition process used to make this alloy is sufficiently close to equilibrium growth that it is able to find a near-equilibrium condition and grow a grain structure with the preferred grain boundary solute content. This is at least somewhat plausible in light of the kinetic calculation of Ruan and

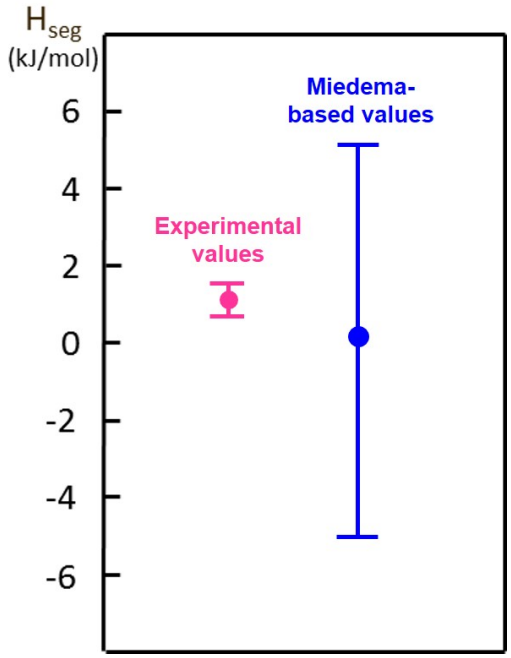

Figure 29: The average, maximum, and minimum segregation energy of the experimental values and the values calculated based on the Miedema segregation model. As is shown here, the averages in both cases are slightly postive, however, due to the variance in data sources, the calculated value has a range across +5 to -5 kJ/mol.

Schuh[119], who estimated that the average atom might diffuse around 20 nm over the surface before becoming buried in an Al-Mn electodeposit, and for our deposition conditions a somewhat larger diffusion length of perhaps 40 nm is kinetically reasonable. In this scenario, the majority of atoms would experience both bulk and grain boundary states as they traverse the surface during deposition, and might therefore preferentially assemble into a near-equilibrium grain boundary segregation state. In this scenario, the grain boundary segregated state is of lower energy than the competing solid solution, but it is an interesting question whether it would successfully compete with the equilibrium diagram that involves intermetallic Al_6Mn. In nanocrystalline materials, it has been suggested that grain boundary segregated polycrystals can energetically compete with second phases such as intermetallics in equilibrium[43]. In similar Al-Mn electrodeposits studied in the prior work, heating has been shown to lead to intermetallic

formation[5, 34, 46, 120, 121], which suggests that the polycrystalline state may be out of equilibrium, as discussed next.

Another possibility is that the deposit is not in equilibrium, but rather is in a kinetically trapped condition, and the grain boundary segregation we observe is therefore a signature of thermodynamic preference but is not equilibrated. If the polycrystalline state is already viewed as a metastable state excited above an intermetallic ground state, then incomplete grain boundary segregation would represent an even further degree of excitation (i.e., higher-energy metastable condition entrapped kinetically). In this case the true grain boundary segregation energy would be higher, and underestimated by the above model. There is some reason to expect such situation. For example, the Miedema heat of mixing for Mn in Al used above ($\Delta H^{int}_{BinA} = -106$ kJ/mol) is somewhat higher than one obtains from an analysis of CALPHAD-type free energy functions for the Al-Mn system which are used to generate the phase diagram[42]. Using such equations in the dilute limit of Mn concentration yields an alternative value of $\Delta H^{int}_{BinA} = -70$ kJ/mol. Using this value to correct the estimate of Equation 12 yields a somewhat higher grain boundary segregation energy of 5300 J/mol. If this value is more reflective of the true grain boundary segregation energy for Mn in Al, then the fact that it is four to five times higher than the effective value extracted from the experimental results would align with the electrodeposit being out of equilibrium, i.e. not fully segregated to the extent it could be. Future work examining changes in segregation state upon heating might prove helpful in more precisely determining the true value of the grain boundary segregation energy.

3.4 CONCLUSIONS

The grain boundary structure of electrodeposited Al-6.7 at.% Mn has been studied experimentally using aberration-corrected STEM and APT, and compared with a Miedema-based grain boundary segregation model. Both the STEM and APT results revealed that Mn is segregated to grain boundaries in the as-deposited condition, and showed reasonable quantitative agreement with one another. Using the McLean isotherm (and therefore assuming an equilibrium condition) gives a grain boundary segregation energy of order 1100-1500 J/mol. This very low energy level suggests that segregation is either very subtly favored thermodynam-

ically in this system, or the deposit is out of equilibrium and does not find as segregated a condition as it would like. Both of these possibility are supported by Miedema-type calculations, with the lower bound value (1000 J/mol) matches with the first measurement while the bulk phase diagram calculation with value of 5030 J/mol anticipate greater segregation if the sample were able to fully equilibrate. This segregation behavior has tremendous value for the enhanced stability of nanocrystalline Al-Mn alloys, for it not only provides solute drag at the grain boundary from a kinetic point of view, but at the same time, according to the calculation here, provides a lower grain boundary energy.

4

THERMAL STABILITY OF DUAL-PHASE AL-MN ELECTRODEPOSITS - MODEL DEVELOPMENT

The dual-phase Al-Mn alloys exhibit different characteristics with the addition of Mn solutes not only in their as-deposited structures, but also in the annealing behaviors. From the XRD results in Figure 30, a small Al FCC (111) peak is discovered for samples with lower Mn concentration; however, as the Mn concentration increases, the (111) peak is replaced with an embedded peak inside the amorphous hump at around 42° 2θ, which is an indication of transition from FCC embedded in an amorphous matrix to an icosahedral phase embedded in an amorphous matrix at a higher Mn concentration.

In preliminary annealing studies, the different annealing behaviors were also discovered within the same annealing history. For samples with Mn concentration ranges from 8.9 at.% Mn to 10.1 at.% Mn, shown in Figure 31, the DSC heat release curves show one single asymmetric peak while annealed from 50 to 550 °C. However, at higher concentration, with Mn concentration at 13.7 at.%, the DSC curve shows two distinct and well-separated peaks, where the first peak is significantly lower in the total heat released compared with the second peak. In between the concentration range, where the Mn concentration is 11.3 to 12.5 at.%, the DSC curves are complex and convoluted, with several peaks. This chapter focuses on discussing the simple case (one single asymmetric peak, lower Mn concentration); the other two cases will be discussed in the following chapters. The "low concentration dual-phase alloy" in this chapter thus refers to the samples with 8.9 and 10.1 at.% Mn.

4.1 EXPERIMENTAL PROCEDURES

The materials were plated as described in Section 2.1.1. In this chapter, the samples were chosen from the group with Mn concentration at 8.9 ± 0.4 at.% and 10.1 ± 0.4 at.%, which according to XRD, exhibit a small fraction of FCC crys-

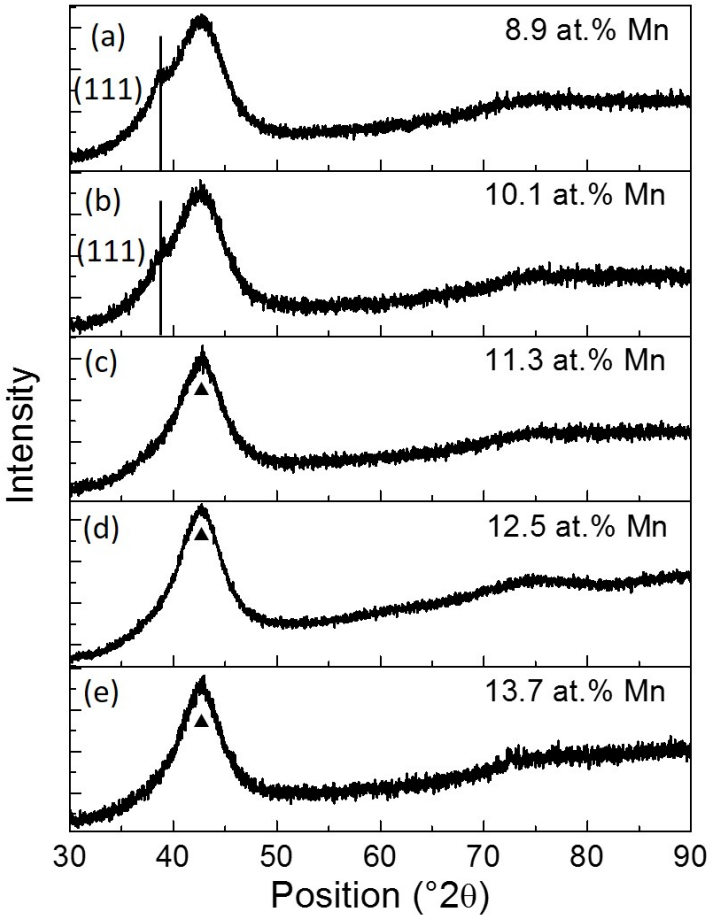

Figure 30: The as-deposited structures with different Mn concentration of Al-Mn alloys from chloraluminate ionic liquid bath under room temperature, with (a) 8.9 at.% Mn, which you can see a side peak at 38° 2θ embedded in the amorphous hump, which correspond to the Al (111) peak marked. Same for (b) with Mn concentration of 10.1 at.%. For higher concentration (c), (d) and (e), we see there is no Al (111) peak presented. There are some features emerging inside the amorphous hump (marked with upper triangle), which we believed is the indication of formation of icosahedral phase.

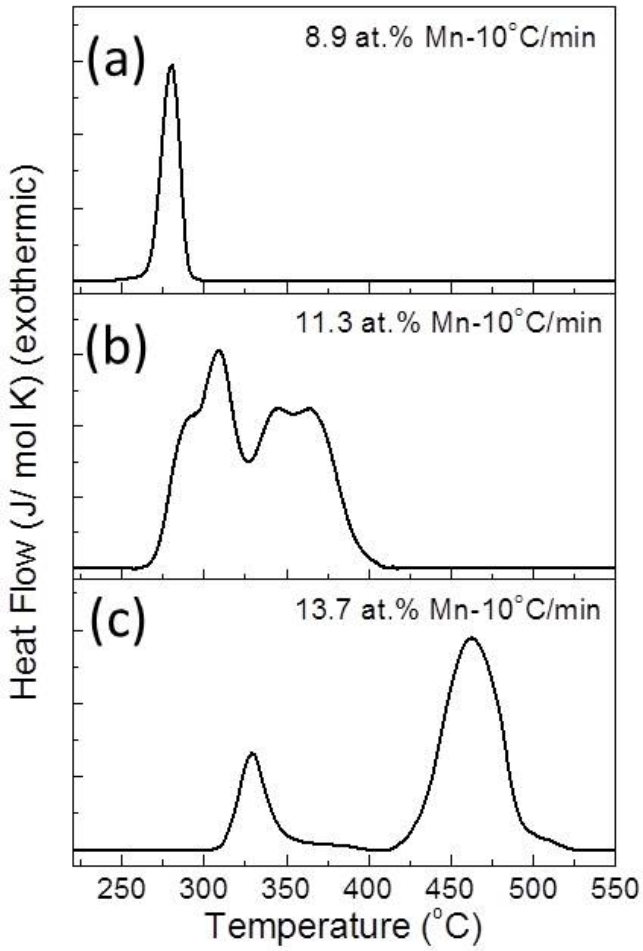

Figure 31: Three different kinds of DSC experimental results observed in Al-Mn alloy system with a ramping rate of 10 °C/min. The result shown in (a) shows a single asymmetric peak, and (b) shows a complex four-peak structure, and (c) shows a two-peak process. Besides the differences in the number of peaks, we can also see that as Mn increases, the transformation temperature increases.

talline phase embedded in an amorphous matrix. The samples were subjected to the same annealing procedures as described in 2.1.3. The pre-annealed and post-annealed samples were all studied with XRD and TEM for microstructural analysis as in Section 2.1.2.

4.2 PHASE TRANSFORMATION STUDY

The TEM results of the 8.9 at.% Mn sample are shown in Figure 32. Figure 32(a) shows the as-deposited state of the dual-phase 8.9 at.% Mn alloy with a small ordering crystal around 10 nm embedded within the amorphous matrix. The XRD for the as-deposited state shown in Figure 30(a) also shows a small (111) Al FCC peak embedded inside the amorphous hump. All of these suggest the existence of an FCC phase and are well aligned with the studies in Ref. [34]. (b) and (c) are samples annealed at 290°C for 1 hour. The annealed structure shows a region of Al FCC solid solution nanocrystalline diffraction rings in (b) and a mix of Al_6Mn orthorhombic structure and Al FCC rings in (c). This phase evolution is completely consistent with the phase diagram prediction[4].

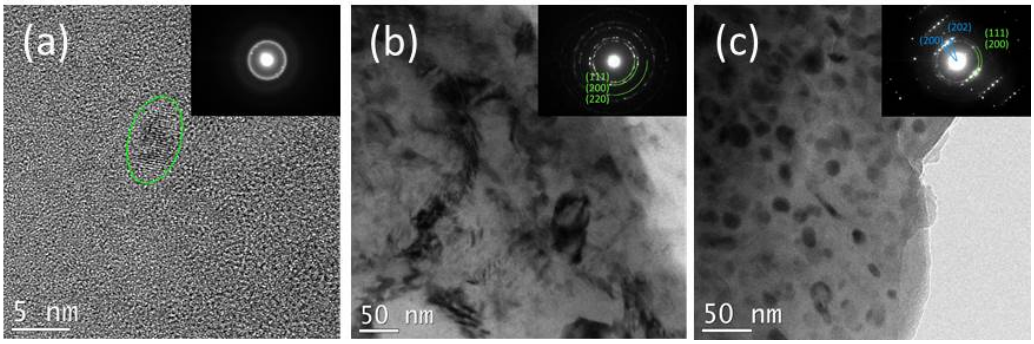

Figure 32: TEM micrographs of (a) as-deposited 8.9 at.% Mn Al-Mn alloys and (b) (c) alloys annealed at 290°C for 1 hour. The annealed structure shows a region of Al FCC solid solution nanocrystalline diffraction rings in (b) and a mix of Al_6Mn orthorhombic structure and Al FCC rings in (c). In (c), the blue index and arrow show the diffraction spots which belong to the Al_6Mn structure; the diffraction rings for the Al FCC structure are marked by the green arc in both (b) and (c).

To understand the time and temperature impact on the annealing results, different annealing studies were carried out. Figure 33 shows two different XRD patterns from different annealing conditions. Figure 33(a) shows a sample annealed isothermally at 290°C for 1 hour and (b) shows a sample annealed with a change in temperature from room temperature to 550°C with a heating rate of 5°C/min. The two XRD patterns were analyzed with Rietveld refinement for the volume percent of each phase, and then converted into weight percents based on

the weight of each phase. Note that the Al FCC solid solution phase is marked with a down triangle. For both structures in Figure 33, it is shown that for isothermally annealed samples, the post-annealed structure contains 46.6 wt.% of the Al FCC phase and 53.4 wt.% of the Al_6Mn phase, and that there was no amorphous hump in the sample, i.e., no untransformed amorphous phase. However, for the sample that went through a higher annealing temperature, i.e., in Figure 33(b), the fractions of the Al FCC and the Al_6Mn orthorhombic phases are 38.8 wt.% and 61.2 wt.% respectively, which are close to the equilibrium phase fractions calculated from the phase diagram (39.5 wt.% Al FCC and 60.5 wt.% Al_6Mn). Moreover, the lattice spacing of the FCC solid solution phase for the sample annealed at higher temperature is 4.057 Å and for the sample isothermally annealed at 290°C is 4.054 Å, which also suggests that for the FCC phase annealed at higher temperature, the Mn concentration is lower[122].

Aside from the structural data, DSC peaks were also analyzed. It was found that the DSC peaks are highly asymmetric, especially at higher ramping rates, which is shown in Figure 34. The peaks are further analyzed, as seen in Figure 35, which shows the ramping experiments for one of the 8.9 at.% sample and one of the 10.1 at.% sample and their corresponding first and second derivatives. The samples were both ramped from room temperature to 550°C with a ramp rate of 50 °C/min. The original experimental peaks both show asymmetry, and the first and second derivatives both suggest that there were two peaks overlapping together instead of one single peak, i.e., there were two reactions in the annealing process, which happened sequentially and at temperatures fairly close to one another.

It is worth noting that for the 10.1 at.% sample, the reactions are shifted to a higher temperature and the two reaction temperatures are closer; thus it is harder to distinguish the two peaks. However, we still found a trace peak signal in the second derivative in Figure 35(f), suggesting the two samples follow a similar reaction route.

All these phenomena suggest that the microstructure evolution process of the low-concentration dual-phase alloys is composed of two processes:

1. Crystallization of the amorphous phase into the FCC phase at a lower temperature.

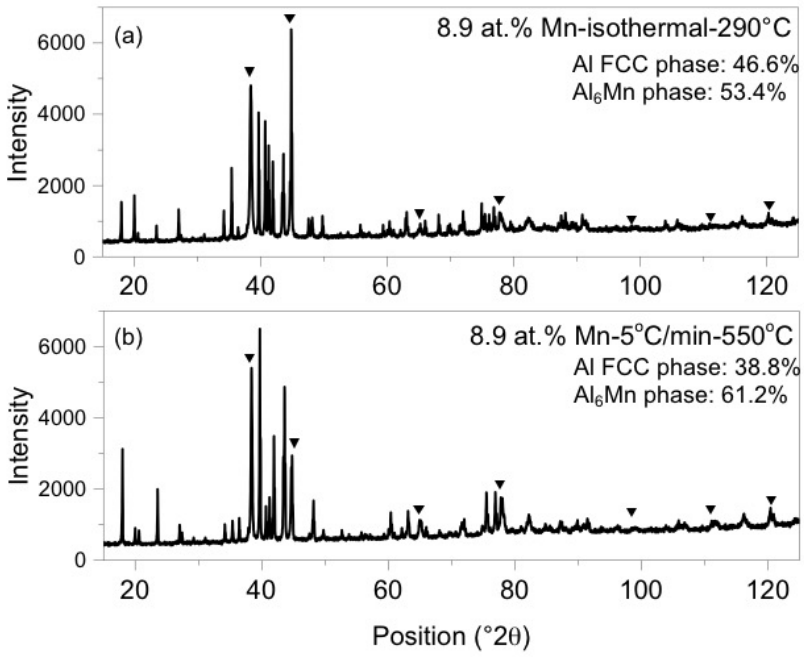

Figure 33: The XRD pattern of Mn 8.9 at.% sample (a) isothermally annealed at 290°C for 1 hour in DSC, which the DSC signal drops down to background suggesting the reaction process has completed. (b) shows the XRD of a sample ramped up to 550°C with a ramp rate of 5 °C/min. The Al FCC solid solution phase is marked with a down triangle. The fraction of Al FCC solid solution phase and Al_6Mn orthorhombic phase is acquired by Reitveld refinement. It is worth noting that neither phase has an amorphous hump, suggesting that at low temperature the Al_6Mn transformation is not completed. At high temperature, the Mn diffuses out from the Al-FCC solid solution sites to form Al_6Mn. The final fraction of the two phases in (b) is in good agreement with the value calculated from the phase diagram, which is 60.5% of Al_6Mn and 39.5% of Al FCC solid solution.

2. Precipitation of the orthorhombic Al_6Mn intermetallic phase at a slightly higher temperature.

The traditional JMAK model will not apply to this multi-reaction case; an adjusted kinetic model is needed. The schematics of the reaction process are shown in Figure 36.

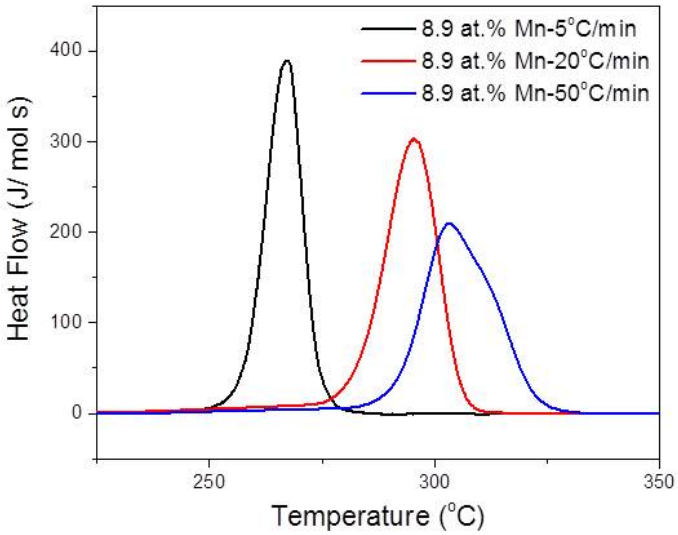

Figure 34: An example of the impact of different heating rates on the isochronal analysis process. The sample shown here were heated at 5, 20, and 50 °C/min. As heating rate increases, the peak becomes broader and the asymmetry becomes more significant.

4.3 MODIFICATION OF KINETIC MODELS

As mentioned in Chapter 3, for decades researchers have been trying to expand the traditional JMAK model into one that could include impingement and different phase transformation mechanisms. However, there is not yet any complete model that can be used to describe the sequential, multiple reaction process. As a result, adaptations are needed while using the phenomenological JMAK model for such multi-reaction processes. As mentioned in Section 2.4.1, Mittemeijer *et al.* have demonstrated a simple and systematic single-reaction JMAK analysis, which this thesis will adopt and then adapt to treat the multi-reaction process in the dual phase Al-Mn system.

To begin with, the total volume of the sample is V, the amorphous phase volume is V_A, and the final product volumes of the first and second reactions are denoted as V_F and V_O, respectively. The phases involved here are the amorphous phases (shown as A), the FCC phase (shown as F), and the intermetallic phase

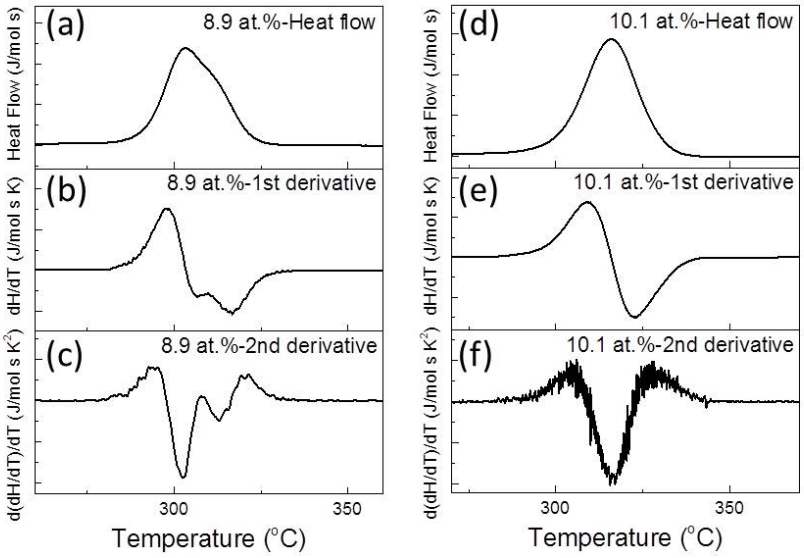

Figure 35: The DSC peaks for Mn 8.9 at.% (a) and 10.1 at.% (d) samples. (b) (c) and (e) (f) are its corresponding first and second derivatives. The samples were both ramped from room temperature to 550°C with a ramp rate of 50 °C/min. The peak shows asymmetry. The first derivative and second derivative combined with the XRD results shown in Figure 33 suggests that there were two reactions in the annealing process. It is worth noting that for 10.1 at.% sample, the reactions are shifted to higher temperature and the two reaction temperatures are closer, thus it is harder to distinguish the two peaks. However, we still found a slight peak at in the second derivative in (f), suggesting the two samples follow the similar reaction route.

(shown as O, since Al_6Mn is of orthorhombic structure). The proposed series reactions and corresponding volumes (shown in brackets) of each phase are as follows:

$$A(V_A) + F(V - V_A) \rightarrow F(V - V_A + V_{tF}) + A(V_A - V_{tF}) \tag{14}$$

in which V_{tF} is the volume of amorphous phase transformed into FCC phase. After the amorphous phase is crystallized, the Mn inside FCC solid solution diffuses to the grain boundary at higher temperature to form Al_6Mn precipitates. Assuming the reaction reached final equilibrium, the reaction can be shown as:

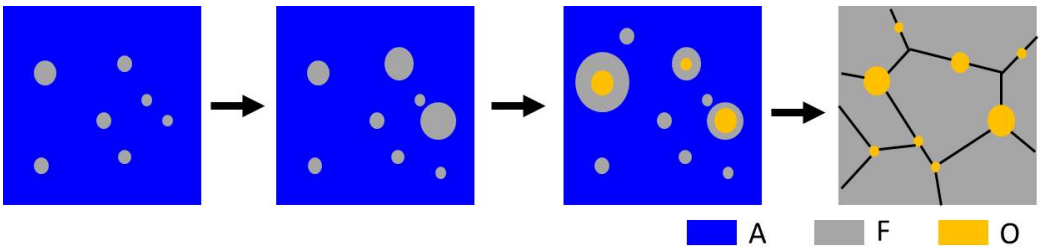

Figure 36: The schematics of transformation mechanism for the two reaction process. A stands for amorphous phase, F is for FCC, and O is for orthorhombic Al_6Mn. The reaction starts with nano-scale FCC crystals embedded in amorphous matrix, in which crystallization of amorphous phase started first and then eventually reached the equilibrium FCC-Al_6Mn mixture. The black lines are the grain boundaries.

$$F(V - V_A + V_{tF}) + A(V_A - V_{tF}) \rightarrow F(V_F) + O(V_O) \tag{15}$$

where V_O is the final volume of the Al_6Mn phase. The final volume fractions of the FCC and the Al_6Mn phases are governed by the phase diagram using a lever rule calculation. If one assumes that the pre-existing V_F is V_{Fi}, and the final fraction V_O in equilibrium in the whole sample is aV, where constant a can be calculated using the lever rule from the phase diagram, using the extensive volume concept introduced in Section 2.4.1, the relationship between the extensive volume and the transformed volume can be expressed as follows: For the first reaction,

$$\int_{V_{Fi}}^{V_F} dV_F = \int_{V_{Fi}}^{V_{eF}} \frac{V - V_{Fi} - V_F}{V - V_{Fi}} dV_{eF} \tag{16}$$

in which V_{eF} is the extensive volume for the final phase of reaction 1, i.e. the amorphous crystallization into FCC. Note that the lower bound is V_{Fi} instead of 0 here due to the fact that the transition volume doesn't start from zero, i.e., there is a pre-existing FCC phase.

The fraction transformed for the first reaction can be shown as

$$f_F = \frac{V_{tF}}{V - V_{Fi}} \tag{17}$$

In which f_F is the fraction transformed for the amorphous to FCC crystallization reaction. As a result, Equation 16 can be integrated and introduced into Equation 17, from which the following equation can be derived:

$$f_F = 1 - \exp\left(\frac{V}{V - V_{Fi}}\right) \times \exp\left(-\frac{V_{eF}}{V}\right) \tag{18}$$

For Equation 18, the analytical solution for isothermal process (equation 3) and isochronal process (equation 4) can both be applied. If isochronal process is considered, as is the experimental conditions in the experimental data here, the equation will be as follows:

$$f_F = 1 - \exp\left(\frac{V}{V - V_{Fi}}\right) \times \exp\left(-\left(\frac{RT^2}{b}\right)^{n_F} k_F \exp\left(-\frac{n_F Q_F}{RT}\right)\right) \tag{19}$$

For the second reaction, which is the precipitation of Al_6Mn reaction here, the final fraction for the transformed phase is constrained by the equilibrium concentration calculated from the phase diagram. The relationship between the extensive volume here with the transformed value can be expressed as follows:

$$\int_0^{V_O} dV_O = \int_0^{V_{eO}} \frac{V_F - V_O}{aV} dV_{eO} \tag{20}$$

The fraction transformed for the second reaction can then be described as

$$f_O = \frac{V_{tO}}{aV} \tag{21}$$

In which the fraction transformed for the second reaction f_O is simply the volume of the product of the second reaction V_{tO} over the total volume the reaction can transformed into, aV. As mentioned in the above context, a is a constant calculated from the phase diagram which depends on the global Mn concentration of the alloy.

Integration of Equation 20 and substitution into Equation 21 gives:

$$f_O = \frac{1}{a}\left(1 - \exp\left(\frac{V_{eO}}{aV}\right)\right)\left(1 - \left(1 - \frac{V_{eO}}{aV}\right)\exp\left(-\frac{V_eF}{V} \times \frac{V}{V - V_{Fi}}\right)\right) \tag{22}$$

Now, the analytical isochronal solution (equation 4) can be further substituted into equation 22.

$$f_O = \frac{1}{a}\left(1-\exp\left(-\frac{1}{a}\left(\frac{RT^2}{b}\right)^{n_O} k_o^{n_O} \exp\left(-\frac{n_O Q_O}{RT}\right)\right)\right) \times \left(1-\left(1-\frac{V_{Fi}}{V}\right)\exp\left(\frac{V}{V-V_{Fi}}\right)\exp\left(-\left(\frac{RT^2}{b}\right)^{n_F} k_F^{n_F} \exp\left(-\frac{n_F Q_F}{RT}\right)\right)\right) \quad (23)$$

With the analytical solution and the right volume representation, a multiple reaction process in a single DSC run can be determined using the physical parameters as described in Equation 19 and Equation 23.

For a solid state transformation and its measured physical quantity in the transformation process (here, heat released in the DSC measurement), the relationship of the measured physical quantity and the fraction transformed can be expressed as equation 5. Here, due to there being two reactions in a single DSC experiment, the reaction can be described as

$$\frac{dH}{dT} = \Delta H_F \frac{df_F}{dT} + \Delta H_O \frac{df_O}{dT} \quad (24)$$

in which ΔH_F and ΔH_O are the total heat released for the crystallization and precipitation reactions respectively.

Next, Equation 19 and Equation 23 can be substituted into Equation 24, in which the full equation is shown in Equation 45 and the detailed derivation is shown in Appendix A.

4.4 DATA FITTING AND TTT DIAGRAM CONSTRUCTION

With the full heat flow equations, the DSC dataset can be fitted. The samples examined here are 8.9 at.% and 10.1 at.% Mn, and the annealing procedure was conducted using 5, 10, 15, 20, 25, 30, 40, 50°C/min from room temperature to 550°C. As mentioned in Chapter 3, it is important that the background of DSC heat flow data is correctly subtracted and interpolated to make sure that each dataset has the same number of data points to prevent biased weighting in data fitting.

The two different sets of samples with two different concentrations were fitted simultaneously. For instance, because the reaction is the same, the activation energy for the reaction was set the same for both samples, i.e. in the fitting, there

were only two activation energy, one was for crystallization, the other was for precipitation regardless of the concentration of the samples. However, due to the differences in concentration, the final composition and the diffusion behavior might be different, as a result, factors such as total heat released, growth index (which is related to the density of pre-existing nuclei), reaction constant were set separately. For example, there were four reaction heats released in the fitting, one for the crystallization of 8.9 at.% Mn, one for crystallization of 10.1 at.% Mn, one for precipitation reaction in the 8.9 at.% Mn sample, and one for precipitation reaction in the 10.1 at.% Mn sample.

4.4.1 *Data Fitting Results*

The key reaction kinetic parameters acquired from the data fitting process using Equation 45 are listed in Table 5, with a fitting quality of $R^2 = 0.95$.

Table 5: The fitted values for 8.9 and 10.1 at.% Mn, as mentioned in the context, the activation energies fall within literature values and aligns well in the value found in Chapter 2. It is worth noting that the growth index n also changes in the fitting, due to the fact that if more pre-existing nuclei presented, the growth index will be larger.

Mn conc. (at.%)	8.9	10.1
$n_{crystallization}$	3.1	2.8
$Q_{crystallization}$ (kJ/mol)	157.8	
$n_{precipitation}$	3.1	2.8
$Q_{precipitation}$ (kJ/mol)	127.9	

The DSC curves for 8.9 at.% and 10.1 at.% Mn samples are shown in Figure 37 and Figure 38. Figure 37 shows fitting results for 8.9 at.% Mn Al-Mn alloy dual phase alloy. The dots show the experimental data and the line shows the corresponding fitting result. The reaction kinetics are assumed the same across different heating rates and remain the same during the annealing process (iso-kinetic process). The fitted curves capture the asymmetry in the experimental data. The activation energy for the crystallization process is 158 J/mol, which falls into the range of literature data from 134 to 184 kJ/mol[7, 9, 123, 124]. The growth index

n is close to 3, suggesting a three dimensional interface-controlled process. The precipitation for Al_6Mn is 128 kJ/mol, which also lies within literature values of 80 to 167 kJ/mol[7, 9, 123, 124], shown in Table 6. Moreover, this value aligns well with the activation energy found for precipitation reaction in Chapter 2, in which the activation energy was 127 kJ/mol. This suggested that the model developed here is capable of capturing the key kinetic factors in the reaction regardless of the solute content and initial structure, at the same time proving the assumption that the activation energy for the same reaction (here, precipitation of 8.9 and 10.1 at.% sample) is independent of Mn concentration. The growth index is 2.99, close to 3 as the crystallization reaction, also suggesting a three dimensional interface-controlled process. Note that this process is different from the precipitation reaction mechanism found in Chapter 2. In Chapter 2, the transformation mechanism for the precipitation reaction is of a diffusion-controlled process. Also, if one looks into the value closely in Table 5, it is not hard to see that the one with more pre-existing FCC nuclei (the 8.9 at.% sample) has a slightly larger growth index, which is consistent in the description of the model, where a larger index in this condition suggests more pre-existing nuclei.

Table 6: Upper and lower limit of literature values of activation energies from amorphous Al crystallization as well as Al_6Mn precipitation. The data is compared and collected with Reference [7, 8, 9, 10].

Literature Values (kJ/mol)	
Crystallization	Precipitation
134	80
184	167

Combining with the results here, we can see that

- Single phase nanocrystalline alloy (below 7.5 at.% Mn): The precipitation reaction is a diffusion-controlled process.

- Low concentration dual-phase alloy (8.9 to 10.1 at.%Mn): The precipitation reaction is an interface-controlled process, and so is the crystallization process.

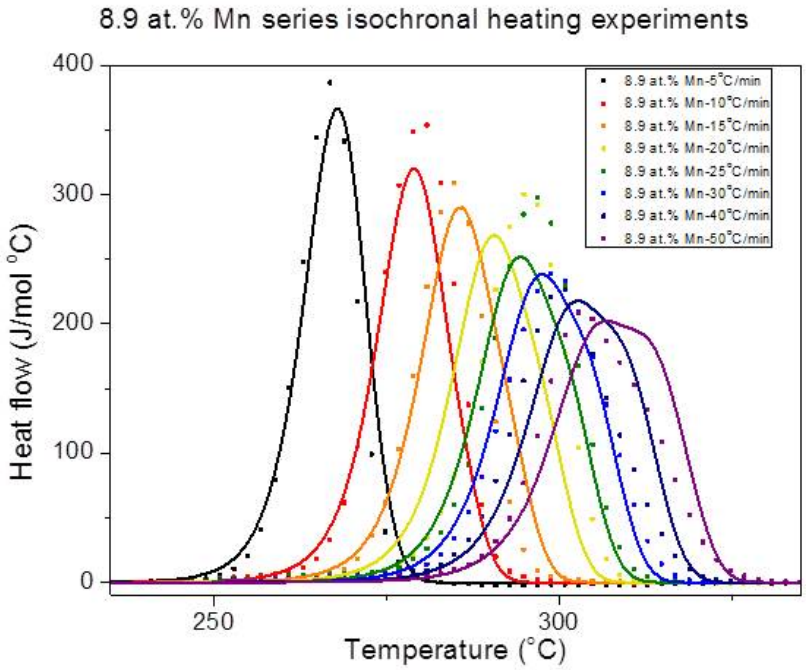

Figure 37: The experimental data (dots) and corresponding fitting results (lines) for 8.9 at.% Mn of Al-Mn alloys with DSC heating rates from 5 °C/min to 50 °C/min from room temperature to 550°C. The fitting was done with non-linear least square fit with 5000 iterations. The activation energy Q and the growth index n are set as equal across different heating rates. The fitted curves capture the asymmetric traits in the experimental data.

The change in reaction mechanism can be a direct result of the increase in Mn. The stoichiometry of Al_6Mn is roughly 14 at.% Mn. Moreover, the average grain boundary segregation is around 3 to 4 at.%[91], and it has also been reported that for the dual-phase alloy, the Mn preferentially occupies the amorphous phase, with concentration slightly higher than the average concentration by about 2 at.%[53]. These show that at lower Mn concentration, the lack of Mn inside the system is the rate determining step for the kinetic transformation, the system must have sufficient Mn locally to undergo the precipitation reaction. This is why the reaction mechanism studied using the kinetic model suggested that it's a diffusion-controlled process. For the dual-phase system, the activation energy is the same. However, the uneven distribution of Mn in the system makes some

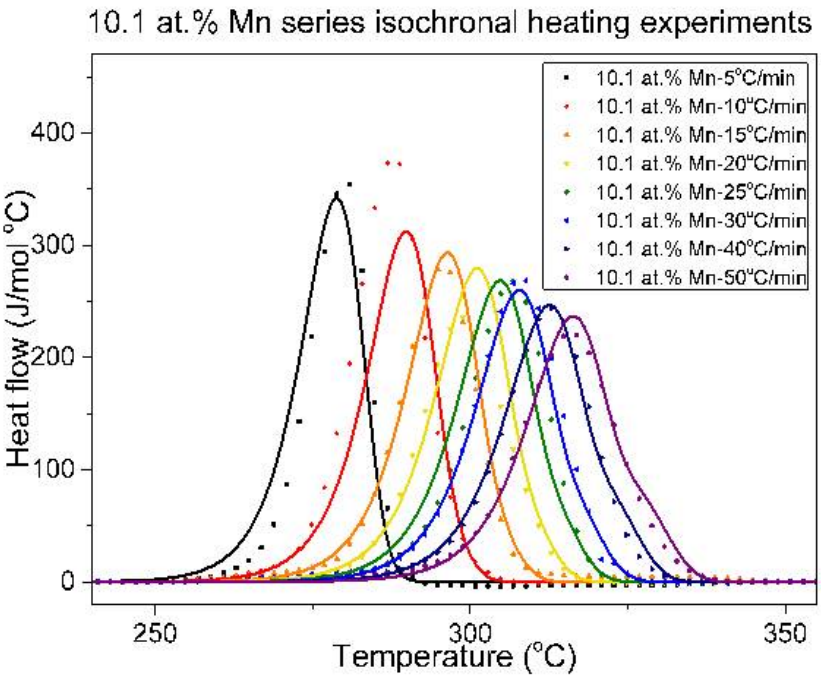

Figure 38: The same Q fitted for a 10.1 at.% Mn sample, the fittings was able to capture the temperature shift due to the concentration difference in Figure 37 and at the same time gives a reasonable fit, suggesting that the assumption that the activation Q for a reaction doesn't change with Mn concentration is reasonable.

areas closer to the stoichiometry of Al_6Mn compound, and thus more favorable for the precipitation reaction. Moreover, for the dual-phase sample, the FCC crystallites are embedded in the amorphous matrix, as a result, to create and move the interface becomes the limiting step for the system to evolve, making the transformation an interface-controlled reaction. The kinetic model developed here was able to capture this change of reaction mechanism.

4.4.2 *The Implication of Kinetic Parameters*

To sum up the features of the kinetic models as developed here as well as the experimental results:

- The model is capable of capturing the asymmetry in the DSC peaks, which arises due to the two reactions.

- The activation energy for the same reaction is the same regardless the bulk concentration of the system, however, the growth index and other parameters will change.
- The position of the peak is decided by the activation energy (Q) and the reaction constant (k).
- The height of the peak is decided by the total heat released (H) and the growth index (n).
- Holding all other conditions the same, the increase in heating rate will shift the peak to higher temperature, i.e. there will be a time lag if the heating rate is too high.

4.4.3 *TTT diagram*

With the above kinetic parameters, the TTT diagram of the complicated dual-phase structure evolution can be constructed. To do this, the fitted values are introduced into the isochronal form of modified JMAK equation, i.e. the isochronal heat flow equation in Equation 45. The TTT diagram is focused in a range between room temperature to 660°C, which is the melting point of pure Al. The fraction transformed is calculated by integrating the transformation peak and normalizing with the total heat released in the reaction. The time at 1% of total transformation and approximately 100% transformation at each temperature are marked as the reaction start point and finish point. The TTT diagram for the 8.9 at.% Mn and 10.1 at.% are shown in Figure 39. In general, the two TTT diagrams look quite similar. The low temperature crystallization reaction is shown in transition from blue to grey and the high temperature precipitation reaction is shown in transition from grey to orange. In the middle, the two reactions overlap together. This trend is especially clear in the lower temperature region, where the two reactions are highly overlapped and below a certain temperature, it is possible that the pre-existing FCC crystals can transform into Al_6Mn orthorhombic phase before the amorphous crystallization reaction occurs. At higher temperatures, the two reactions are further separated, which is in agreement with the prominent asymmetric peaks at higher heating rate. Comparing the two different sample sets, it is found that with higher Mn content, the as-deposited structure can retain the

amorphous phase for a longer time at the same temperature, i.e. the increase of Mn decreases the rate of interface motion during the annealing process, which increases the amorphous structure's thermal stability.

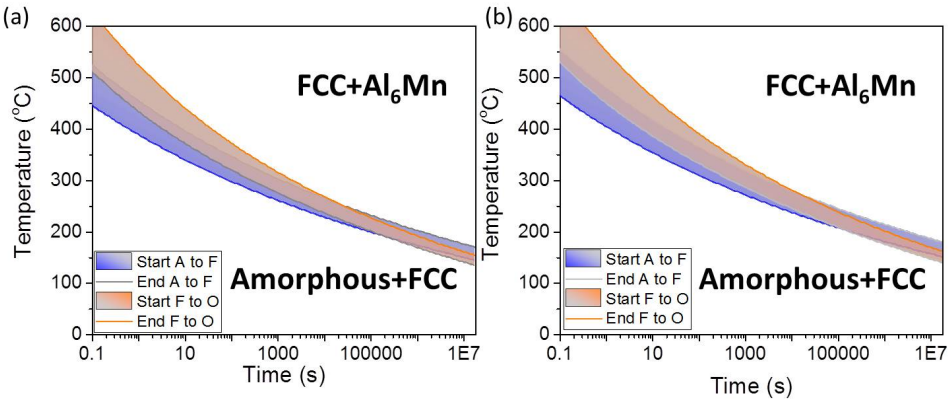

Figure 39: (a)The TTT digram constructed using parameters acquired in DSC data fitting in Figure 37. The region in red shows the time and temperature for amorphous to FCC crystallidzation process and blue shows the FCC crystallites futher transforms into Al_6Mn intermetallic. At higher temperature, the crystallization reaction is really fast and no overlap with the precipitation process, i.e. the reaction steps are distinct two steps process. However, at lower temperature, the two reactions overlap together, which agrees with the DSC data.(b)shows the TTT for 10.1 at.% Mn, which is nearly the same as in (a), but can retain the amorphous structure longer during annealing.

4.5 CONCLUSIONS

In this chapter, the thermal stability of low concentration dual-phase Al-Mn electrodeposits (8.9 at.% and 10.1 at.%) was examined. It was found that the alloy undergoes the crystallization reaction first, and at higher temperature, the Al_6Mn compound precipitates out from the crystalline FCC phase.

The JMAK kinetic equations were modified to provide a better description of this sequential microstructure evolution process. The modified JMAK model accurately described the microstructure evolution process. Unlike the monocrystalline structure shown in Chapter 2, which is a diffusion-controlled process due to the limited Mn content in the alloy, the dual-phase structure exhibited an interface-

controlled process for the precipitation reaction, with the same activation energy found in Chapter 2. This shows that the Mn content and distribution have a tremendous effect on the phase evolution mechanism of Al-Mn alloy but do not alter the activation energy of the transformation.

The modified JMAK kinetics also show that for the dual-phase alloys examined here (8.9 at.% and 10.1 at.%), the higher Mn content delays the crystallization and precipitation reactions, which is in line with experimental findings. This finding might be counter-intuitive since most people would expect the increase of Mn will move the system closer to stoichiometry, thus the reaction could normally happen faster. This is not the case because both the crystallization reaction and precipitation reactions are apparently interface controlled reactions[125, 126, 127]. The higher Mn content could impede the movement of interfaces because Mn has a higher diffusion activation energy[14].

5

CASE STUDY - THERMAL STABILITY OF DUAL-PHASE AL-MN ALLOYS

As mentioned in Chapter 4, the annealing behavior of the dual-phase alloy varies drastically depending on Mn concentration and an analytical model has been developed for multi-reaction transformation process. This chapter serves as a case study using the developed kinetic model on the higher Mn concentration systems, with the studies first on the two-peak system (13.7 at.%Mn) and then moving on to the multi-peak system (12.5 at.%Mn). Due to the complexity of amorphous Al alloys, the amorphous Al-Mn structure will also be discussed.

5.1 PHASE TRANSFORMATION OF AMORPHOUS AL-MN

In the past, it was hard to obtain bulk nanostructured Al-based alloys using direct solidification from the as-cast state, and as a result, researchers have been using amorphous Al-based alloys as precursors to prepare nanostructures with improving mechanical properties[124, 128]. The glassy phase can be formed using different classes of additive metals such as Al-rare-earth-transition metal, Al-rare-earth etc. using rapid solidification[124]. In this process, not only can the amorphous phase form, but also phases such as amorphous plus nanocrystalline FCC Al, and nano-quasicrysatlline plus FCC Al alloys. Among them, it is well-known that in the Al-transition metal alloy systems containing Mn[27], Cr[129], V[130, 131], Cu-Fe[132] or Pd-Mn[133], and Fe-W[134], Mackay icosahedral clusters containing 55 atoms can form, and some of the nanoquasicrystalline phases have been shown to be successful in achieving high tensile strength without sacrificing ductility[28].

The high temperature behaviors of the amorphous or amorphous-crystalline mixtures have always been complex in the Al-based systems. Aside from the primary crystallization[135] and grain growth of the primary crystalline phase[136, 137, 138], which are commonly seen in other systems as well, the precipitation of the metastable icosahedral phases and the growth of pre-existing icosahedral

nuclei are also possible in the Al-based system. For instance, $Al_{90}Fe_5Ce_5$ alloy prepared by rapid solidification has shown the icosahedral phase transformation under both isothermal and non-isothermal annealing conditions[139]. Melt-spun Al-Cu-V alloys were also found to have an icosahedral phase transformation[140]. Systems such as Al-Mn-Si and Al-Mn have also been studied extensively for the formation of the icosahedral phase during annealing[141, 142, 143, 144, 145].

Al-Mn was the first system to be found with icosahedral phase present after rapidly quenching [30] and after electron beam surface melting[146]. It has also been subsequently found to have amorphous to quasicrystalline transformation in the solid state during annealing at high concentration (≈12.5 to 25 at.%)[131, 144, 147, 148]. In molten salt electrodeposited Al-Mn, it has been shown that at 225 and 325°C, the icosahedral phase can be directly deposited[149]. The formation of icosahedral phase using electrohydrodynamic atomization has shown to be a homogeneous nucleation process[150], and structural quality of the icosahedral phase which grows from a non-equilibrium process is highly dependent on the diffusion of the atoms[69]. Consequently, the study of Al-Mn amorphous phase has always been a challenging task and the transition involving icosahedral phase should be taken into consideration in this study especially for the high Mn content amorphous alloys.

In this work, due to the composition similarity as well as the driven technique used here, aside from verifying the kinetic model developed in Chapter 4 using this high Mn concentration alloy, the phase transformation mechanism as well as the phase involved will also be discussed in detail.

5.2 PHASE TRANSFORMATION IN HIGH MN CONCENTRATION AL-MN ALLOYS

The heat flow from the DSC annealing process was found to be two separately peaks, which is different from the earlier studies. As mentioned in Chapter 5.1, the Al-13.7at.%Mn is highly likely to form the icosahedral Al-Mn. The TEM and DSC experiments conducted both confirm this hypothesis. Figure 40 shows the diffraction rings for as-deposited state and the state annealed for 1 hour at 350°C. In Figure 40(a), only a diffuse ring is shown, however, in (b), there are extra rings in the

diffraction pattern, which is the same as the results from reference[80, 122, 151] and also align with the icosahedral ring calculation based on the simulation[147].

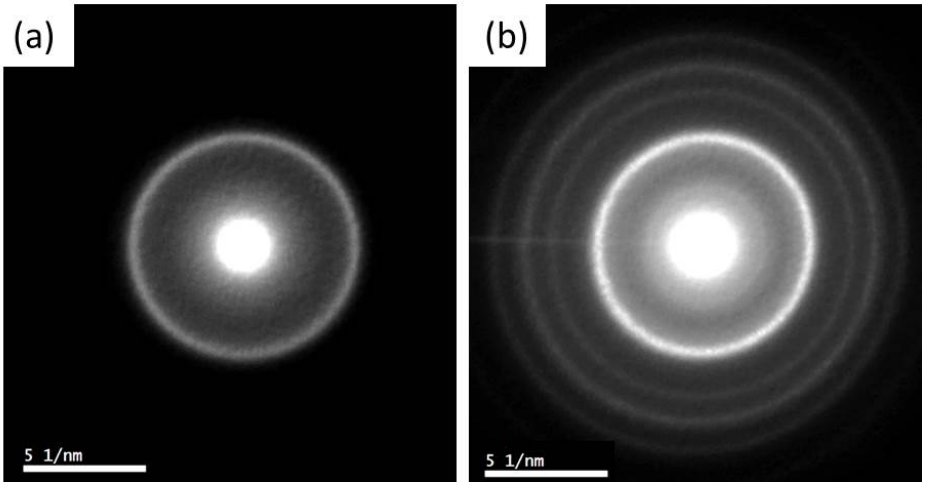

Figure 40: (a) Shows a diffraction ring for the as-deposited state and (b) After annealing at 350°C for 1 hour, the diffraction pattern shows extra diffraction rings, which is an indication of icosahedral phase formation.

To be more confident with the transformation mechanism, isothermal annealing was conducted to examine the heat flow and the transformation mechanism. The result of isothermal annealing is shown in Figure 41, in which a monotonically decreasing signal was shown, suggesting it was a growth process rather than that of a nucleation and growth process. This confirms the existence of pre-existing crystals inside the system[152] and is one of the unique characteristic of icosahedral phase transformation.

5.3 DATA FITTING AND TTT DIAGRAM CONSTRUCTION

The modified JMAK model developed in Chapter 4 can be applied to the two-peak system in this study since its also a sequential reaction process although the peaks here are well-separated. The DSC fitting result and the corresponding TTT diagram construction can be shown in Figure 42 and Figure 43. The fit quality here is $R^2 = 0.93$. The extracted activation energy for the first transformation was 202 kJ/mol and the second reaction is 255 kJ/mol, which are both quite different from the activation energies from the previous sections. Instead of being close to

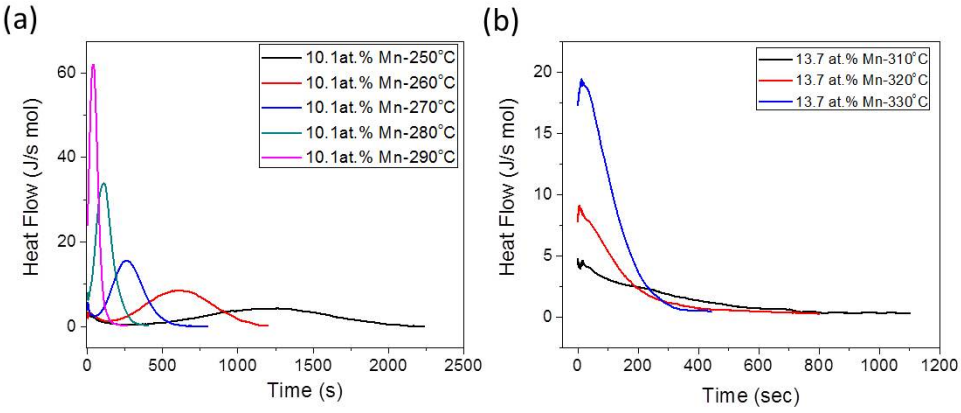

Figure 41: (a)The isothermal annealing for 10.1 at.% sample, showing a peak for a typical nucleation and growth process and (b) For 13.7 at.%, the monotonically decreasing signal suggests a growth process. The initial rise is from the instrument to reach equilibrium condition.

the activation energy for Al diffusion, both of them are more close to Mn diffusion activation energy. The diffusion activation energies for Mn are tabulated in Table 7. The growth index for both reactions indicate a growth mode of three dimensional diffusional controlled process (n=1.5), which is in agreement with the finding from Popescu *et al.*[153].

Table 7: Diffusion activation energy of Mn in Al[11, 12, 13, 14]

Activation Energy of Mn diffusion (kJ/mol)
217.1
211.3
228.7
189.1
198.0

The activation energy is in good agreement with Chen et al.[80], who showed that the activation energy for the icosahedral phase growth from a sputtered $Al_{0.83}Mn_{0.17}$ film ranges from 192 to 242 kJ/mol. In the microstructural study for the 13.7 at.% Mn sample, it was also observed that the changes in diffraction

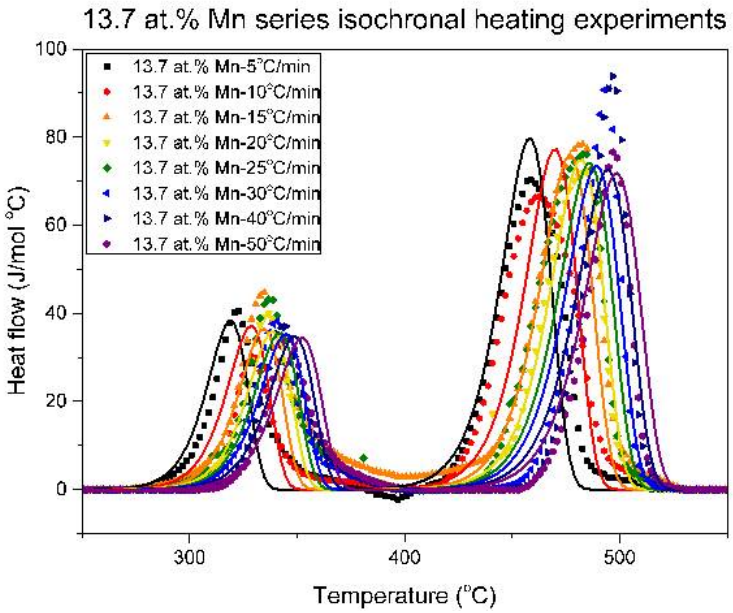

Figure 42: The dataset and fitting result of 13.7 at.% Mn sample, using the exact same fitting equation as the fitting for the low concentration dual-phase alloys.

rings pre- and post-annealing in Figure 40 is in agreement with the evidence of icosahedral phase transformation based on the calculation in Ref. [147].

In summary, when the room temperature ionic liquid electrodeposited Al-Mn alloy reached a higher concentration of 13.7 at.% Mn, the as-deposited structure is a dual-phase amorphous-quasicrystalline structure instead of FCC crystallites embedded in amorphous matrix, and it is different from the low Mn concentration dual-phase alloys described earlier. The high Mn concentration alloy undergoes the icosahedral phase transformation instead of the amorphous-FCC crystallization reaction. The kinetic model developed for two sequential reaction processes in Chapter 4 can capture these differences, showing different activation energies as well as different reaction mechanisms. Using the extracted kinetic data, the TTT diagram can be constructed, demonstrating a simple and efficient way to understand the usable range of the material.

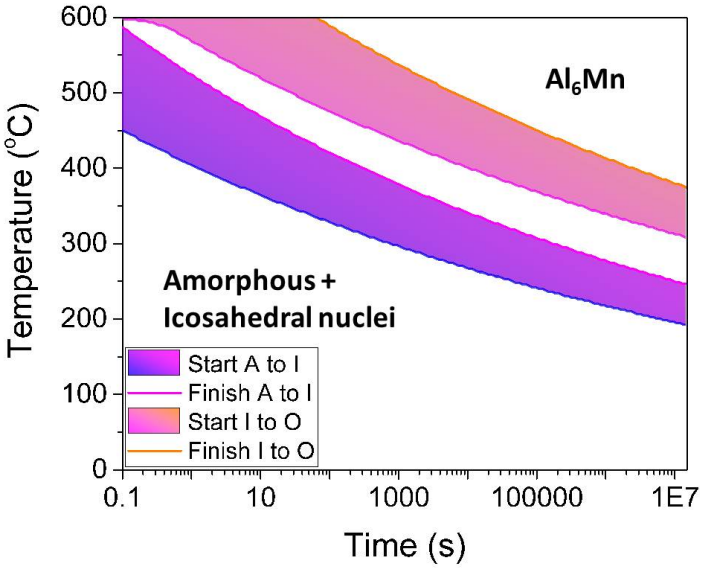

Figure 43: The corresponding TTT diagram for 13.7 at.% Mn sample, which shows the first transformation process finishes before the starting of the second reaction.

5.4 EXPANSION OF KINETIC MODELS

Moving to the range in between 8.9 at.% and 13.7 at.% Mn samples, as shown in Figure 31, the samples 11.3 at.% and 12.5 at.% Mn show an overlap of several peaks, which are hard to decouple using experimental methods. As a result, the potential of using the multi-reaction modified JMAK model to analyze these data set is explored.

5.4.1 *Kinetic Model Development*

To discuss the samples between 10.1 and 13.7 at.% Mn, in which the first reaction mechanism is crystallization of amorphous phase follows by the precipitation of Al_6Mn phase, and 13.7 at.% sample, which has amorphous to the icosahedral phase and icosahedral phase to Al_6Mn phase, assumptions need to be made to propose a new analytical model based on the JMAK kinetics:

- The reactions involved are a competition between these reaction sequences, i.e. the composition between crystallization of FCC phase and icosahedral phase transformation. The schematic can be seen in Figure 44.

- The two reaction routes do not interfere with one other, i.e. there is no change in activation energy of any of the reactions.

- The reaction heats are linearly additive.

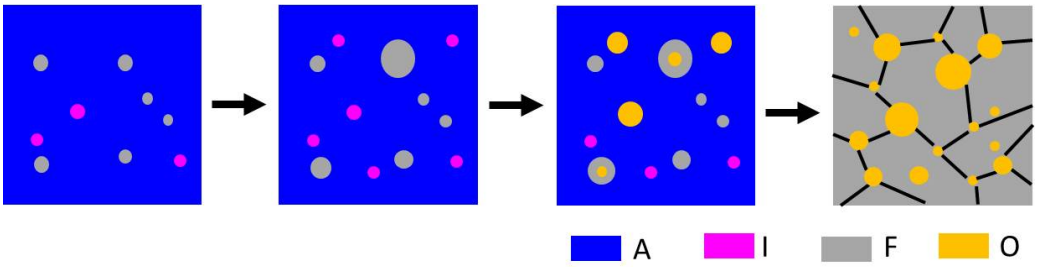

Figure 44: The schematics for the proposed reaction in the middle range concentration dual-phase system. In which the sample is originally composed of FCC, amorphous, and icosahedral phase. Following two different reaction routes A $\rightarrow$ F $\rightarrow$ O and I $\rightarrow$ O), the final structure is composed of FCC and Al_6Mn intermetallic phase.

As a result, the heat flow equation here can be considered as

$$\frac{dH}{dT} = \Delta H_1 \frac{df_1}{dT} + \Delta H_2 \frac{df_2}{dT} + \Delta H_3 \frac{df_3}{dT} + \Delta H_4 \frac{df_4}{dT} \tag{25}$$

in which the the subscript 1 denotes the amorphous to FCC crystallization process, subscript 2 denotes the FCC precipitation to Al_6Mn reaction, subscript 3 is the amorphous-icosahedral phase transformation, and subscript 4 is for icosahedral phase to Al_6Mn intermetallic.

The following boundary conditions are imposed in order to derive the proper fractions transformed from the extensive volume concept. The initial volumes of each phase have the following relationship:

$$v_a + v_f + v_i = 1 \tag{26}$$

in which ν_a is the initial volume fraction of amorphous phase, ν_i is the initial volume fraction of the icosahedral phase, and ν_f is the initial volume fraction of the FCC phase.

Since the icosahedral phase is a metastable phase and will not present to the final state, the final phase would still be FCC Al-Mn solid solution and Al_6Mn intermetallic at equilibrium. The fraction of Al_6Mn can be calculated as before using the lever rule from the phase diagram, however, there are two sources of Al_6Mn here, one is from the FCC crystallization route, the other is the icosahedral reaction route. As a result, it is set that

$$a_1 + a_2 = a \tag{27}$$

in which a is the final fraction calculated from the phase diagram, a_1 is the Al_6Mn that comes from the FCC crystallization reaction route, and a_2 comes from the icosahedral reaction route.

Consider the volumes for different reactions using the extensive volume concept in JMAK, for reaction 1 (FCC crystallization)

$$\int_{V_{\nu_f}}^{V_1} dV_1 = \int_{V_{\nu_f}}^{V_{e1}} \frac{V - V_{\nu_f} - V_1}{V - V_{\nu_f}} dV_{e1} \tag{28}$$

reaction 2 (Al_6Mn precipitates from FCC solid solution phase)

$$\int_{0}^{V_{a_1}} dV_2 = \int_{0}^{V_{e2}} \frac{V_1 - V_2}{a_1 V} dV_{e2} \tag{29}$$

reaction 3 (amorphous to icosahedral transformation)

$$\int_{V_{\nu_i}}^{V_3} dV_3 = \int_{V_{\nu_i}}^{V_{e3}} \frac{V - V_{\nu_i} - V_3}{V - V_{\nu_i}} dV_{e3} \tag{30}$$

and reaction 4 (icosahedral to Al_6Mn)

$$\int_{0}^{V_{a_2}} dV_4 = \int_{0}^{V_{e4}} \frac{V_3 - V_4}{a_2 V} dV_{e4} \tag{31}$$

With these extensive equations and the boundary conditions, the full heat flow equation can be expressed as equation 50.

5.4.2 *Data Fitting*

Due to the complexity of the reaction mechanism here, the activation energies are taken as known based on the prior results in this thesis. The input parameters now include the reaction conditions such as heating rate, temperature, the final Al_6Mn fraction, and the activation energy for each reaction. The values such as total heat released for each reaction, reaction constant, and growth mode will be fitted in this case.

The dataset for Al-12.5 at.% Mn with a heating rate of 15 °C/min and the corresponding fitted curve are shown in Figure 45. The growth index is 1.5 for the amorphous to FCC reaction, 1.6 for the FCC-Al_6Mn precipitation process, 1.5 for amorphous-icosahedral transformation, and 1.5 for icosahedral-Al_6Mn reaction process. Note that for the icosahedral reaction routes, the transformation mechanism remains the same. However, for the amorphous-FCC-Al_6Mn route, the process changes from an interface controlled process for the low-concentration dual-phase towards a diffusion-controlled process, suggesting that at higher Mn concentration level and high amorphous fraction, the diffusion of atoms becomes harder, this might be due to the dramatic decrease of diffusivity in the amorphous phase compared with crystalline phase[154].

In general, the model captures the reaction peaks in the two transformation processes, however, the position is not exact due to the complexity of the system. In reality, the different reactions probably interfere with each other and canât be considered as a linear combination. Thus it will be a challenge to acquire an exact solution for this kind of competing reaction process. Nevertheless, the reaction formula here does provide insight for the stability region of the different phases. Figure 46 shows the TTT diagram for 12.5 at.% Mn, suggesting that the four reactions have a very large overlapping range across temperature and time. However, in general, higher Mn concentration tends to retain the amorphous structure at higher temperature, suggesting Mn is a stabilizer for the Al amorphous structure.

5.4.3 *The Impact of Mn Concentration*

To understand the impact of Mn on the stability of Al-Mn alloy structure, it is important to compare the transformation temperatures with different Mn concentra-

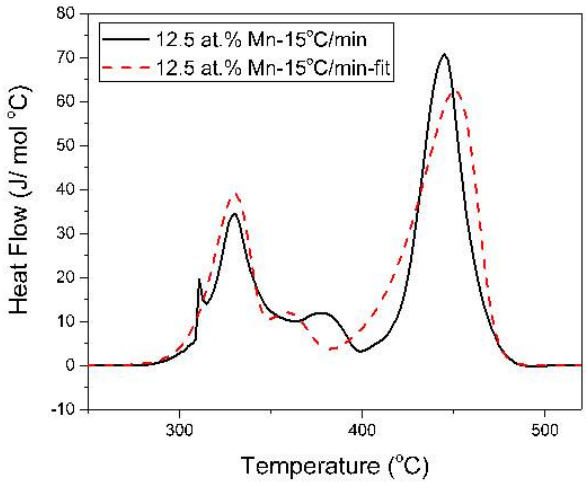

Figure 45: 12.5 at.% Mn DSC data with ramping rate of 15 °C/min with fitted curve, the model captures the middle peak in between the two major reactions, however, the position is not exact due to the complexity of the peak sets.

tions. Figure 47 shows the time and temperature relationship of the same reaction at different Mn concentrations. Figure 47(a) for example, shows the transformation start line of the FCC to Al_6Mn reaction for Mn concentration for 6.5 at.%Mn (nanocrystalline), 8.9 and 10.1 at.% Mn (low concentration dual-phase structure), and 12.5 at.% Mn (intermediate concentration dual-phase structure). In Figure 47(a), it is clear that the FCC to Al_6Mn reaction at 6.5 and 12.5 at.% Mn happens far more slowly than the 8.9 and 10.1 at.% Mn samples. This might seems not intuitive, however, the reaction modes are different for these two sets of samples, as the reaction modes are summarized in Table 8. As a result, these two set of data shouldn't be compared directly. If only the low-concentration dual-phase alloys are considered, the increase of Mn stabilizes the alloy against phase transformation. The same is true for the amorphous crystallization to FCC, amorphous to icosahedral, and icosahedral to Al_6Mn reactions. For the diffusion controlled precipitation reaction (FCC to orthorhombic Al_6Mn phase) in 6.5 and 12.5 at.% Mn samples, the mechanism for diffusion-controlled might be different. For the 6.5 at.% Mn sample, the bulk concentration is far from the stoichiometry of the product Al_6Mn phase, and as a result, diffusion becomes important because at this

concentration, precipitates cannot form. However, in the Al-12.5 at.% Mn case, the diffusion becomes more difficult due to the presence of amorphous phase, thus inhibiting the transformation. Comparing the TTT diagram of 12.5 at.% Mn and 6.5 at.% Mn, at temperature below 500°C, the 12.5 at.% Mn is slightly more stable compared to the 6.5 at.% sample, showing that Mn alloying and the increase of the amorphous phase both somewhat improve stability.

Table 8: Summary of reaction mechanisms at various concentrations at elevated temperature. "D" is a diffusion-controlled process, "I" is an interface-controlled process, and "/" is not applicable. A→F is for the amorphous crystallization, F→O is for the Al_6Mn precipitation in FCC, A→I is for the amorphous to icosahedral phase transformation, and I→O is the icosahedral to Al_6Mn phase transformation.

Mn (at.%)	A→F	F→O	A→I	I→O
6.5	/	D	/	/
8.9	I	I	/	/
10.1	I	I	/	/
12.5	D	D	D	D
13.7	/	/	D	D

5.5 CONCLUSIONS

In this chapter, the microstructure evolution and the annealing behaviors of high Mn concentration (13.7 at.%) Al-Mn dual-phase electrodeposits were discussed and the modified JMAK model was tested. It was found that unlike the low Mn concentration alloy (8.9 at.% and 10.1 at.%), which undergoes an amorphous crystallization and Al_6Mn precipitation process, the high 13.7 at.% Mn sample undergoes an icosahedral phase transformation process, in which the reaction is diffusion-controlled. The kinetic model developed in Chapter 4 was able to describe to this transformation process, showing activations that are different from the amorphous-FCC crystallization process and FCC-Al_6Mn precipitation process.

After validating the two-reaction kinetic model, evaluating the stability of the 13.7 at.% Mn sample, and confirming the phases involved in the high concentration dual-phase alloy, the middle range dual-phase alloys with concentration of 11.3 and 12.5 at.% were examined. It was proposed that the reaction mechanism here was composed of two different competing reaction routes: the amorphous-FCC-Al_6Mn route and the amorphous/quasicrystalline-icosahedral phase-Al_6Mn reaction route. The aforementioned modified JMAK model was adopted once again to extract kinetic data from these systems. The fitting was able to give a general picture of the time-temperature relationships between the phases, showing that the analytical JMAK model can be potentially expanded to different multi-reaction systems. However, further studies are needed to more accurately describe the competition between the two reactions, and to incorporating the inhomogeneity inside the sample.

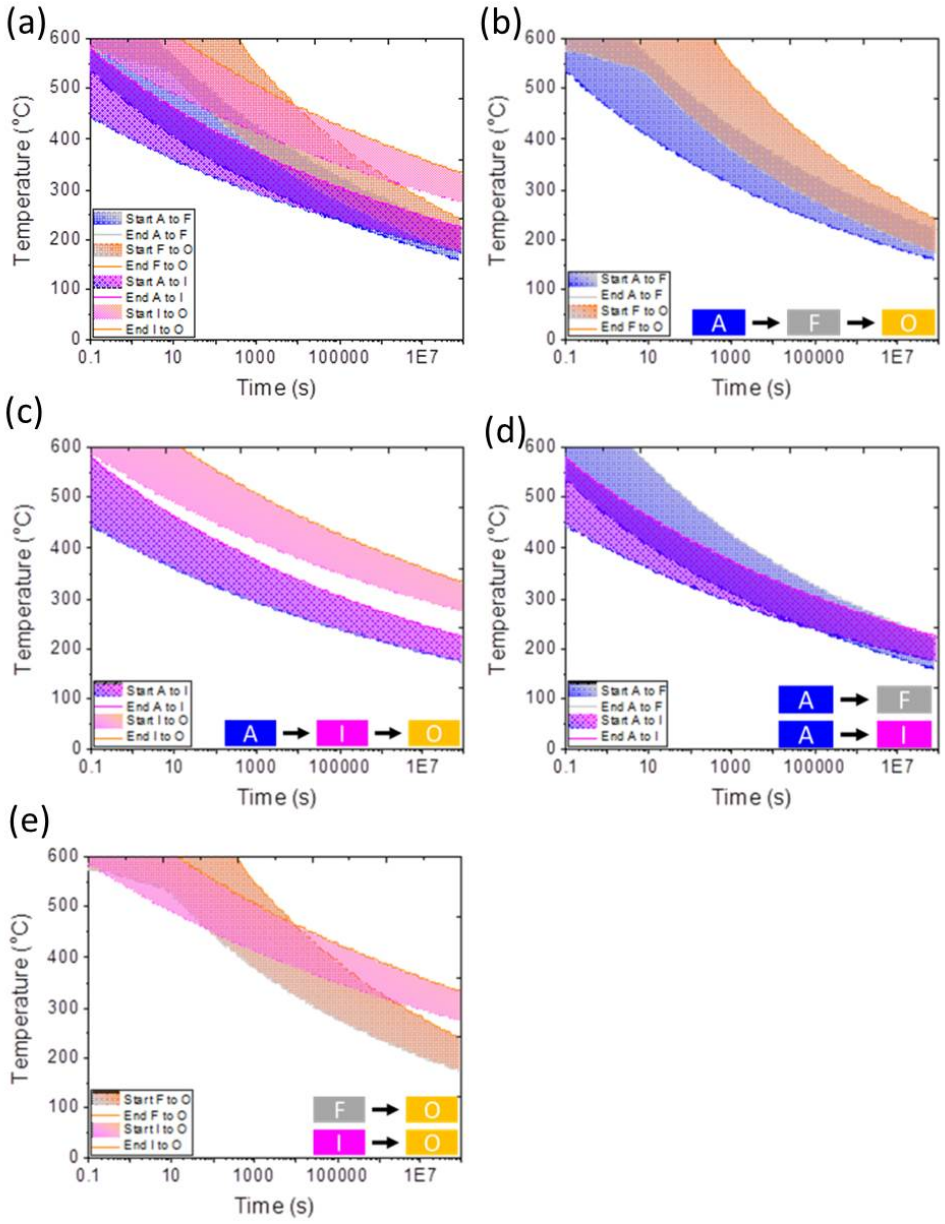

Figure 46: (a)The TTT diagram for the 12.5 at.% Mn sample, in which two reaction routes compete with each other. The first route is the A(amorphous) → F(FCC) → O(Al_6Mn) phase (isolated out to plot at (b)) and the second route is the A(amorphous) → I(icosahedral) → O(Al_6Mn) process (isolated out to plot at (c)). The reaction time and temperature for the low temperature (A to I or A to F) are also compared in (d) and high temperature reactions I to O and F to O are compared at (e). One can see that at lower temperature, the amorphous to FCC phase happens faster compared to the amorphous to icosahedral phase, the F to O reaction also happens faster than the I to O phase. However, at temperature above 400°C, it is easy for the icosahedral phase to rapidly transform into the intermetallic phase.

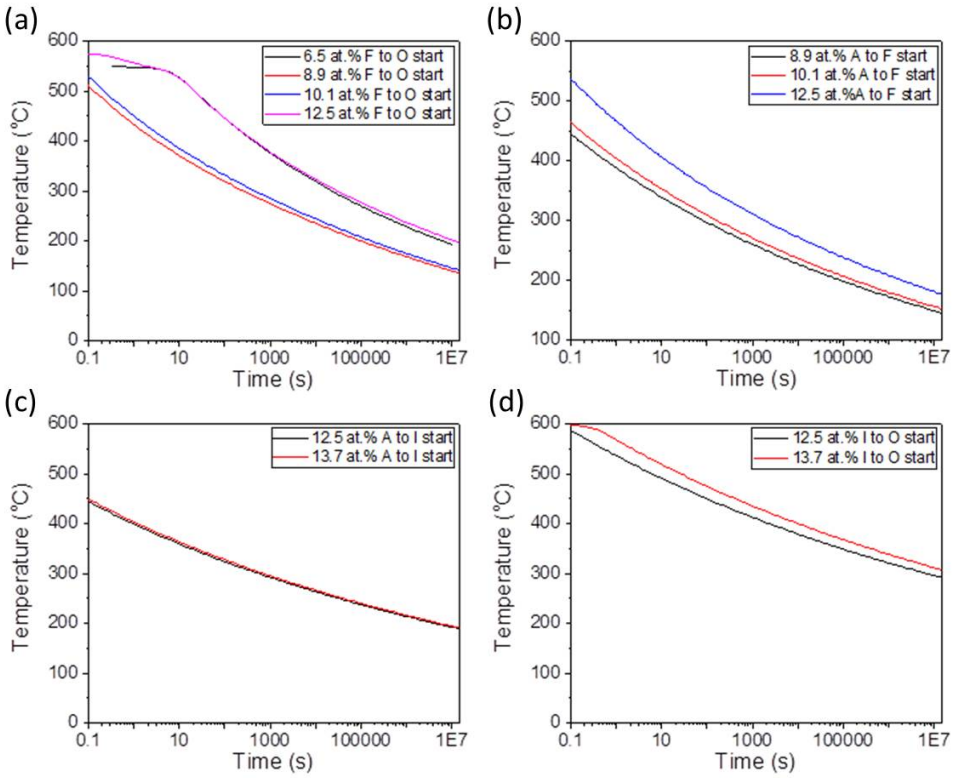

Figure 47: Time and temperature relationship for the starting reaction of (a) FCC(F) to Al_6Mn(O) (b) amorphous(A) to FCC(F) (c) amorphous(A) to icosahedral(I) and (d) icosahedral(I) to Al_6Mn(O) reaction compared at different Mn concentrations.

6

CONCLUSIONS

By employing experimental methods, thermodynamic calculations, and analytical JMAK kinetic models, the basic properties of electrodeposited Al-Mn alloys and their stability have been explored. Mn preferentially occupies the grain boundary sites as well as the amorphous phase, contributing to the stabilization of very fine scale nanostructures. The modified JMAK model has proven a useful tool to quickly construct the TTT diagram for the stability region of the different phases, which can efficiently and effectively evaluate the viability of the alloy and avoid catastrophic failures under certain time/temperature conditions. The important conclusions drawn from this thesis are summarized below.

In Chapter 2, the thermal stability including grain growth and phase separation of low-Mn content Al-Mn nanocrystalline alloys was studied. A simple JMAK analytical model was employed to extract kinetic data, and the kinetic data was further used to construct a quantitative TTT diagram. The precipitation reaction was identified as a diffusion-controlled process with an activation energy of 127 kJ/mol, falling into the range of literature values. The TTT diagram constructed was further verified with extended annealing experiments, which showed that the system can retain its nanostructure and experience limited phase transformation at 0.5 homologous temperature for one month, making the alloy viable for many engineering purposes. The calculated TTT diagram has also been demonstrated as a simple and effective way to evaluate the stability of the alloy.

In Chapter 3, in order to understand the stabilization mechanism, the grain boundary chemistry of the same low Mn-concentration single-phase nanocrystalline Al-Mn alloy was studied. Grain boundary segregation was demonstrated in this system in the as-deposited state for the first time. Comparing the experimentally acquired segregation energy with the segregation energies calculated using the thermodynamic-based model, both show that either the segregation is very subtly favored thermodynamically in this system or the deposit is out of equilibrium. In either case, some degree of nanostructure stability is provided by

this grain boundary segregation due to both kinetic solute drag as well as thermodynamic grain boundary energy reduction.

In Chapter 4, the low concentration dual-phase Al-Mn alloys (8.9 at.% and 10.1 at.%) were studied. The system undergoes a multi-reaction sequential process with amorphous-FCC crystallization and then Al_6Mn precipitation. The analytical JMAK model was adopted to model the sequential reaction process. The activation energy of precipitation was found to be 128 kJ/mol, which aligns well with the value found in single-phase nanostructured Al-Mn alloys, and the crystallization and precipitation process are interface-controlled processes. The multi-reaction sequential model developed based on JMAK kinetics has proven effective in the stability study of complex structures.

In Chapter 5, using the model developed in Chapter 4, the middle (11.3 and 12.5 at.%) and high (13.7 at.%) Mn concentration Al-Mn electrodeposits are examined as case studies. The high 13.7 at.% Al-Mn electrodeposits show a transformation mechanism that is different from the the low concentration dual-phase alloy; instead of an amorphous-FCC crystallization process followed by intermetallic precipitation, the high Mn concentration sample undergoes an icosahedral phase transformation that is diffusion-controlled. For the samples in between the high and low concentration range, the reaction mechanism is composed of two different reaction routes. The modified JMAK model was further expanded to accommodate this change, and the TTT diagram was able to map the phases at different times and temperatures. By comparing the TTT diagrams, it is found that Mn does indeed provide stability in both the nanocrystalline phase as well as the amorphous phase containing samples.

The findings in this thesis may provide detailed understanding of kinetic phase transformations in the Al-Mn system and its application as a stabilized nanostructure engineering material, in which not just a strong and tough alloy is presented, but also its viability across time and temperature space. The TTT diagram constructed here can guide the usage of the alloy to avoid the formation of brittle intermetallic phase. The nanostructured Al-Mn material here can retain nanostructure for months at $0.5T_H$, and its stabilization is supported by grain boundary segregation, which is first identied in this system. In dual-phase alloys, Mn also stabilizes the amorphous phase. The analytical model developed here is an effective way to construct the stability region of each phase, which can serve as

a quick tool to map the stability of different phases and thus to better control microstructure even for a complex 4 reaction process.

7

DIRECTIONS FOR FUTURE RESEARCH

Through the present experimental studies of electrodeposited Al-Mn alloys as well as the development of kinetic models for the annealing reactions, many interesting research questions have emerged, and future research efforts may be directed to explore the following topics:

- The relationship of grain size, Mn concentration, and the amount of segregation in the Al-Mn system: In this study, the grain boundary segregation of only a single concentration was studied. In order to have a better understanding of the segregation behavior closer to and further away from the dilute limit, as well to evaluate the stability provided by different Mn incorporation levels, a series concentrations could be explored.

- The amount of grain boundary segregation with respect to the annealing conditions: It has been shown that at extended annealing time, the grain size becomes apparently stabilized. This thesis also showed that the segregation state found here might not be equilibrated. As a result, it would be helpful to study the segregation level at different relaxation conditions to understand the change of segregation level with respect to different annealing conditions.

- Refinement of the kinetic model: It has been shown that due to the heterogeneous distribution of Mn solute, at higher temperatures, the precipitation reaction happens slightly before the TTT diagram prediction. As a result, developing a model that could have one single reaction but at the same time accounting for different diffusion and reaction rate based on concentration is crucial. This could further improve the prediction accuracy of transformation time and phase distribution.

- The interaction and competition between different reactions in a multi-reaction process: In the multi-reaction modified JMAK model, the assumption that the reactions don't interfere is used to simplify the model. However, the

experiments have shown this simplification is only good for basic understanding for the stability regions between the alloys. If the interaction between different reactions can be accounted for, a better description of the phase transformation process could be given.

- The effect of intermetallic on the mechanical properties: Precipitation hardening of Al-Mn alloy has been widely used in the 3000 series alloys. Nevertheless, brittle intermetallic formation at grain boundaries has been shown to compromise the mechanical properties of alloys. As a result, it is necessary to study the mechanical properties of the alloys developed here to optimize the microstructure and the mechanical behavior of the alloys.

A

EQUATIONS AND DERIVATIONS

This section covers the derivation from extensive volume concept to the fraction transformed. Besides the derivation, the full heat flow equation with the kinetic parameters plugged in are also shown here.

A.1 DERIVATIONS

The derivations from the extensive volume to the fraction transform equation are shown here, using the two reaction process as an example. As mentioned, there are two reaction in sequence and overlapping together. The reaction can be consider as in 14 and 4.3. For simplicity here, the full reaction can be shown as:

$$A + F \rightarrow F + O + A \rightarrow F + O \tag{32}$$

and reaction 1 is

$$A \rightarrow F \tag{33}$$

reaction 2 is

$$F \rightarrow O \tag{34}$$

Using the first reaction, due to we have an FCC phase embedded in the amorphous matrix, meaning that the starting volume for the resulting phase is not zero. Which means that in the extensive volume equation, it can be expressed as

$$\int_{V_{1i}}^{V_t} dV_{t1} = \int_{V_{1i}}^{V_{e1}} \frac{V - V_{t1}}{V} dV_e \tag{35}$$

Here, the V_{1i} are the volume for pre-existing nuclei for the first reaction, V_{t1} is the volume transformed in the first reaction, and V_{e1} is the extensive volume of the product of the first reaction. By rearranging the equation, the following format can be achieved.

$$\frac{V - V_{1i}}{V - V_{1i}} - \frac{V_{t1} - V_{1i}}{V - V_{1i}} = \exp(-\frac{V_{1i}}{V}) \times \exp(-\frac{V_{e1}}{V}) \tag{36}$$

Note that fraction transformed f_1 is defined as

$$f_1 = \frac{V_t - V_{1i}}{V - V_{1i}} \tag{37}$$

and $\exp(-\frac{V_{1i}}{V})$ can be defined as constant c due to it only relates to the concentration of the sample (the amount of pre-existing FCC phase). as a result

$$1 - f_1 = c \times \exp(-\frac{V_{e1}}{V}) \tag{38}$$

and

$$f_1 = 1 - c \times \exp(-\frac{V_{e1}}{V}) = 1 - c \exp\left(-(\frac{RT^2}{b})^{n_1} k_1^{n_1} \exp(-\frac{n_1 Q_1}{RT})\right) \tag{39}$$

Consider reaction two, it follows the form

$$\int_0^{V_{t2}} dV_{t2} = \int_0^{V_{e2}} \frac{V_1 - V_{t2}}{aV} dV_{e2} \tag{40}$$

in which V_1 is the volume of the crystalline phase, and a is the fraction of intermetallic phase calculated from the phase diagram. The other notations have the same meaning as for above except it is for the second reaction.

$$\frac{V_1 - V_{t2}}{V_1} = \exp(-\frac{V_{e2}}{aV}) \tag{41}$$

as a result,

$$\frac{V_{t2}}{V_1} = 1 - \exp(-\frac{V_{e2}}{aV}) \tag{42}$$

and

$$f_2 = \frac{V_{t2}}{V} = \frac{V_1}{V}\left(1 - \exp(-\frac{V_{e2}}{aV})\right) \tag{43}$$

and eventually,

$$f_2 = f_1\left(1 - \exp(-\frac{V_{e2}}{aV})\right) = f_1\left(1 - \exp\left(-\frac{1}{a}(\frac{RT^2}{b})^{n_2} k_2^{n_2} \exp(-\frac{n_2 Q_2}{RT})\right)\right) \tag{44}$$

Now, with the equations f_1 and f_2 in place, the heat flow equations can be solved based. The heat flow equations can then be represented with parameters with physical meanings.

A.2 HEAT FLOW EQUATION OF TWO REACTION PROCESS FOR AL-MN DUAL PHASE ALLOY

Here shows the full equations use in the isochronal DSC peak fitting process, in which the equation was first used to extract the kinetic data and then used for construction of TTT diagrams. For simplicity, the crystallization reaction (notation F in chapter 4) is referred as reaction 1 and the precipitation reaction (notation O in chapter 4) is refereed as reaction 2. b is the heating rate in a constant ramp rate experiment. In either case k is the reaction constant, n is the growth exponent, indicating the mode of reaction (diffusion controlled or interface controlled process), and Q is the activation energy. T is the temperature, for isochronal case, it is the temperature at that specific time point, as a result, b and T together contain the information of reaction time. R is the gas constant.

- Heat flow equation for isochronal two reaction process

Let the fraction of initial crystalline phase $\frac{V_{Fi}}{V} = c$, the equation can be simplified as

$$\begin{aligned}
\frac{dH}{dT} &= \left(\frac{n_1 k_1^{n_1}(Q_1 + 2RT)B^{n_1-1}}{b}\right)\left(\frac{H_1}{1-c} + \frac{H_2}{a}\right) \\
&\times \exp\left(-\frac{1}{(1-c)}k_1^{n_1}B^{n_1}\exp(-A_1) - A_1\right) \\
&+ \frac{1}{a^2 b}H_2 n_2 k_2^{n_2}(Q_2 + 2RT)B^{n_2-1}\exp\left(-\frac{1}{a}k_2^{n_2}B^{n_2}\exp(-A_2) - A_2\right) \\
&+ \frac{1-c}{a}H_2 n_1 k_1^{n_1}\exp\left(-\frac{1}{(1-c)}k_1^{n_1}B^{n_1}\exp(-A_1)\right. \\
&\left.- \frac{1}{a}k_2^{n_2}B^{n_2}\exp(-A_2)\right) \\
&\times \left(-\frac{2n_1 RTk_1^{n_1}B^{n_1-1}\exp(-A_1)}{b(1-c)} - \frac{2n_2 RTk_2^{n_2}B^{n_2-1}\exp(-A_2)}{ab}\right. \\
&\left.- \frac{n_1 Q_1 k_1^{n_1}B^{n_1}\exp(-A_1)}{(1-c)RT^2} - \frac{n_2 Q_2 k_2^{n_2}B^{n_2}\exp(-A_2)}{aRT^2}\right)
\end{aligned} \tag{45}$$

in which

$$B = \frac{RT^2}{b} \tag{46}$$

and

$$A_n = \frac{n_n Q_n}{RT} \tag{47}$$

and n = 1, 2 depending on which reaction it is. The total parameters which needed to be fitted here are $k_1, k_2, Q_1, Q_2, n_1, n_2, H_1, H_2$.

Note that while doing the fitting work, the sample group 8.9 at.% and sample group 10.1 at.% were fitted together. Both sample set show evidence of crystallization and then precipitation reactions. However, due to the difference in concentration, certain deviation is expected. As a result, while fitting these two dataset together, it is assumed that the reaction mechanisms don't change, i.e. they were fitted with the same activation energy Q_1 and Q_2 for the crystallization and precipitation reactions. However, the other kinetic related factors such as reaction constant (k_1 and k_2), as well as parameters relating to nucleation sites (n_1 and n_2)

were fitted individually for each concentrations. The total heat released, which related to the amount of Al_6Mn formed, was also different due to different Mn level inside the alloy. As a result, the heat released for each concentration was also fitted separately.

A.3 HEAT FLOW EQUATION OF FOUR REACTION PROCESS FOR AL-MN DUAL PHASE ALLOY

As described in chapter 5, the model for the two reaction process can be expended to four reactions as long as the correct reaction mechanism can be proposed. Here, as mentioned in previous sections, $B = \frac{RT^2}{b}$, and $A_n = \frac{n_n Q_n}{RT}$ in which $n = 1, 2, 3, 4$ depending on the reaction. Here, everything subscript with 1 is parameter for crystallization, 2 for precipitation, 3 for amorphous to icosahedral phase transformation, and 4 for icosahedral to intermetallic Al_6Mn reaction. ν_a is the initial amorphous volume fraction, ν_i is the initial icosahedral phase volume fraction, and ν_f is the initial volume fraction for FCC solid solution phase. α is the final Al_6Mn fraction calculated from the phase diagram. α_1 is the fraction of Al_6Mn formed by the reaction route with FCC as first transition. α_2 is the fraction of Al_6Mn formed by the reaction route with icosahedral phase. The aforementioned parameters follow the following relationships:

$$\nu_i + \nu_a + \nu_f = 1 \tag{48}$$

and

$$\alpha_1 + \alpha_2 = \alpha \tag{49}$$

With this relationship and the competing reactions routes proposed in 5, the following equations for the four reaction transformation can be derived. The resulting heat follow equations with competing reaction routes described based on the physical parameters are shown below.

- Heat flow equation for isochronal four reaction process for Al-Mn dual phase alloy

$$
\begin{aligned}
&\frac{dH}{dT} = \left(\frac{H_1}{\nu_a} + H_2\right)\left(\frac{n_1 k_1^{n_1}(Q_1 + 2RT)B^{n_1-1}}{b}\right) \\
&\times \exp\left(-\frac{1}{(\nu_a)} k_1^{n_1} B^{n_1} \exp(-A_1) - A_1\right) \\
&+ \frac{1-\nu_i}{a_1 b} H_2 n_2 k_2^{n_2}(Q_2 + 2RT)B^{n_2-1} \exp\left(-\frac{1}{a_1} k_2^{n_2} B^{n_2} \exp(-A_2) - A_2\right) \\
&\nu_a H_2\left(-\frac{2n_1 RT k_1^{n_1} B^{n_1-1} \exp(-A_1)}{b\nu_a} - \frac{2n_2 RT k_2^{n_2} B^{n_2-1} \exp(-A_2)}{b a_1}\right. \\
&\left.- \frac{n_1 Q k_1^{n_1} B^{n_1} \exp(-A_1)}{\nu_a RT^2} - \frac{n_2 Q k_2^{n_2} B^{n_2} \exp(-A_2)}{a_1 RT^2}\right) \\
&\times \exp\left(-\frac{1}{\nu_a} k_1^{n_1} B^{n_1} \exp(-A_1) - \frac{1}{a_1} k_2^{n_2} B^{n_2} \exp(-A_2)\right) \\
&\left(\frac{H_3}{\nu_a} + H_4\right)\left(\frac{n_3 k_3^{n_3}(Q_3 + 2RT)B^{n_3-1}}{b}\right) \\
&\times \exp\left(-\frac{1}{(\nu_a)} k_3^{n_3} B^{n_3} \exp(-A_3) - A_3\right) \\
&+ \frac{1-\nu_f}{a_2 b} H_4 n_4 k_4^{n_4}(Q_4 + 2RT)B^{n_4-1} \exp\left(-\frac{1}{a_2} k_4^{n_4} B^{n_4} \exp(-A_4) - A_4\right) \\
&\nu_a H_4\left(-\frac{2n_3 RT k_3^{n_3} B^{n_3-1} \exp(-A_3)}{b\nu_a} - \frac{2n_4 RT k_4^{n_4} B^{n_4-1} \exp(-A_4)}{b a_2}\right. \\
&\left.- \frac{n_3 Q_3 k_3^{n_3} B^{n_3} \exp(-A_3)}{\nu_a RT^2} - \frac{n_4 Q_4 k_4^{n_4} B^{n_4} \exp(-A_4)}{a_2 RT^2}\right) \\
&\times \exp\left(-\frac{1}{\nu_a} k_3^{n_3} B^{n_3} \exp(-A_3) - \frac{1}{a_2} k_4^{n_4} B^{n_4} \exp(-A_2)\right)
\end{aligned}
\tag{50}
$$

B

SUPPLEMENTAL MATERIALS AND OTHER REFERENCES

Here includes the supplemental materials as well as some data sources mentioned in the thesis.

Parameters	Value	Parameters	Value
V_A (A = Al) (10^{-6} m^3/mol)	10.00	K_B^1 (B=Mn) (GPa)	59.67
V_B (B = Mn) (10^{-6} m^3/mol)	7.35	G_A^1 (A=Al) (GPa)	26.59
γ_A^S (A=Al) (J/m^2)	1.16	K_B^2 (B=Mn) (GPa)	120.00
γ_B^S (B=Mn) (J/m^2)	1.60	G_A^2 (A=Al) (GPa)	26.59

Table 9: The data used for H_{seg} calculation using Equation 12. The subscript 1 and 2 showing the differenct sources of the elastic term in Equation 13. 1 is from the Miedema source and 2 is from online database.

[1] T. G. G. Nieh and J. Wadsworth. Hall-Petch Relation in Nanocrystalline solids. *scripta metallurgica et materialia*, 25(c):955–958, 1991.

[2] A. Inoue, F. Kong, S. Zhu, C. T. Liu, F. Al-marzouki, S. Arabia, and H. Kong. Development and Applications of Highly Functional Al-based Materials by Use of Metastable Phases. *Materials Research Bulletin*, 18(6):1414–1425, 2015. ISSN 15161439.

[3] M. Ames, J. Markmann, R. Karos, A. Michels, A. Tschöpe, and R. Birringer. Unraveling the nature of room temperature grain growth in nanocrystalline materials. *Acta Materialia*, 56 (16):4255–4266, 2008. ISSN 13596454.

[4] A. J. McAlister and J. L. Murray. The (Al-Mn) Aluminum-Manganese system. *Journal of Phase Equilibria*, 8(5):438–447, 1987. ISSN 10549714.

[5] B. Grushko and G. R. Stafford. Phase Formation in Electrodeposited and Thermally Annealed Al-Mn Alloys. *Metallurgical Transactions A*, 21(November):2869–2879, 1990.

[6] M. Pohl, O. Storz, and T. Glogowski. Effect of intermetallic precipitations on the properties of duplex stainless steel. *Materials Characterization*, 58(1):65–71, 2007. ISSN 10445803.

[7] N. Ciavaguera, J. A. Diego, M. T. Clavaguera-Mora, and A. Inoue. Nanocrystalline formation of AlNiNdCu materials: A kinetic study. *Nanostructured Materials*, 6(95):485–488, 1995.

[8] Z. Huang, Q. Li, J.F.and Rao, and Y. Zhou. Effects of La content on the glass transition and crystallization process of AlâNiâLa amorphous alloys. *Intermetallics*, 15(8):1139–1146, aug 2007. ISSN 09669795.

[9] N. J. Agreda and J. Luiggi. Isochronal study of Al-Mg, Al-Mn, and Al-Mn-Mg alloys using electrical resistivity and thermoelectric power. *Materials Research*, 2005.

[10] N. J. Luiggi. Isothermal precipitation of commercial 3003 Al alloys studied by thermoelectric power. *Metallurgical and Materials Transactions B*, 28(February), 1997.

[11] S. P. Chen, N. C. W. Kuijpers, and S. van der Zwaag. Effect of microsegregation and dislocations on the nucleation kinetics of precipitation in aluminium alloy AA3003. *Materials Science and Engineering: A*, 341(1-2):296–306, jan 2003. ISSN 09215093.

[12] G. M. Hood and R. J. Schultz. The diffusion of manganese in aluminium. *Philosophical Magazine*, 23(186):1479–1489, jun 1971. ISSN 0031-8086.

[13] D. L. Beke, I. Gödény, I. Móricz, and F. J. Kedves. Diffusion of Mn-54 in aluminium. *Philosophical Magazine Letters*, 60(5):219–224, nov 1989. ISSN 0950-0839.

[14] S. Fujikawa and K. Hirano. Impurity diffusion of manganese in aluminum. *Materials Science Forum*, 13(14):539–546, 1987. ISSN 07408188.

[15] J. Weertman. Hall-Petch strengthening in nanocrystalline metals. *Materials Science and Engineering: A*, 166(1-2):161–167, jul 1993. ISSN 09215093.

[16] K. S. Kumar, H. Van Swygenhoven, and S. Suresh. Mechanical behavior of nanocrystalline metals and alloys. *Acta Materialia*, 51(19):5743–5774, 2003. ISSN 13596454.

[17] C. A. Schuh, T. G. Nieh, and T. Yamasaki. HallâPetch breakdown manifested in abrasive wear resistance of nanocrystalline nickel. *Scripta Materialia*, 46(10):735–740, may 2002. ISSN 13596462.

[18] C. A. Schuh, T. G. Nieh, and H. Iwasaki. The effect of solid solution W additions on the mechanical properties of nanocrystalline Ni. *Acta Materialia*, 51(2):431–443, jan 2003. ISSN 13596454.

[19] C. A. Schuh and T. G. Nieh. Hardness and Abrasion Resistance of Nanocrystalline Nickel Alloys Near the Hall-Petch Breakdown Regime. In *Mat. Res. Soc. Symp. Proc. Vol. 740 Â© 2003 Materials Research Society I1.8.1*, volume 740, pages 1–6, 2003.

[20] G. H. Zahid, Y. Huang, and P. B. Prangnell. Microstructure and texture evolution during annealing a cryogenic-SPD processed Al-alloy with a nanoscale lamellar HAGB grain structure. *Acta Materialia*, 57(12):3509–3521, 2009. ISSN 13596454.

[21] M. E. McHenry, M. A. Willard, and D. E. Laughlin. Amorphous and nanocrystalline materials for applications as soft magnets. *Progress in Materials Science*, 44(4):291–433, nov 1999.

[22] K. H. Hou, M. C. Jeng, and M. D. Ger. A study on the wear resistance characteristics of pulse electroforming Ni-P alloy coatings as plated. *Wear*, 262(7-8):833–844, 2007. ISSN 00431648.

[23] Y. Kawamura, H. Mano, and A. Inoue. Nanocrystalline aluminum bulk alloys with a high strength of 1420 MPa produced by the consolidation of amorphous powders. *Scripta Materialia*, 44(8-9):1599–1604, 2001. ISSN 13596462.

[24] Y. Zhang, Y. Liu, Z. Gao, and D. Wang. Study on crystallization of nanocrystalline/amorphous Al-based alloy. *Journal of Alloys and Compounds*, 469(1-2):565–570, feb 2009. ISSN 09258388.

[25] M. Tavoosi, F. Karimzadeh, and M. H. Enayati. Formation and characterization of amorphousânanocrystalline Al80Fe10M10 [M=Fe, Nb, Ti, Ni, (Ni0.5Ti0.5)] alloys. *Journal of Alloys and Compounds*, 551:584–590, feb 2013. ISSN 09258388.

[26] T. Yamasaki, P. Schlobmacher, K. Ehrlich, and Y. Ogino. Foramtion of amorphous electrodeposited Ni-W alloys and their nanocrystallization. *Nanostructured Materials*, 10(3):375–388, 1998.

[27] D. Shechtman, I. Blech, D. Gratias, and J. W. Cahn. Metallic phase with long-range orientational order and no translational symmetry. *Physical Review Letters*, 53(20):1951–1953, 1984. ISSN 00319007.

[28] A. Inoue, H. M. Kimura, and T. Zhang. High-strength aluminum- and zirconium-based alloys containing nanoquasicrystalline particles. *Materials Science and Engineering A*, 294-296: 727–735, 2000. ISSN 09215093.

[29] Y. Du, J. Wang, J. Zhao, J. C. Schuster, F. Weitzer, R. Schmid-Fetzer, M. Ohno, H. Xu, Z. K. Liu, S. Shang, and W. Zhang. Reassessment of the Al-Mn system and a thermodynamic description of the Al-Mg-Mn system. *International Journal of Materials Research*, 98(9):855–871, 2007. ISSN 18625282.

[30] D. Shechtman, I. Blech, D. Gratias, and J. W. Cahn. Metallic phase with long-range orientational order and no translational symmetry. *Physical Review Letters*, 53(20):1951–1953, 1984. ISSN 00319007.

[31] N. S. Qu, D. Zhu, K. C. Chan, and W. N. Lei. Pulse electrodeposition of nanocrystalline nickel using ultra narrow pulse width and high peak current density. *Surface and Coatings Technology*, 168(2-3):123–128, may 2003. ISSN 02578972.

[32] H. Natter and R. Hempelmann. Nanocrystalline Metals Prepared by Electrodeposition, 2008. ISSN 0942-9352.

[33] L. P. Bicelli, B. Bozzini, C. Mele, and L. D'Urzo. A review of nanostructural aspects of metal electrodeposition. *International Journal of Electrochemical Science*, 3:356–408, 2008. ISSN 14523981.

[34] S. Ruan and C. A. Schuh. Electrodeposited AlâMn alloys with microcrystalline, nanocrystalline, amorphous and nano-quasicrystalline structures. *Acta Materialia*, 57(13):3810–3822, aug 2009. ISSN 1359-6454.

[35] G. R. Stafford. The Electrodeposition of an Aluminum-Manganese Metallic Glass from Molten Salts. *Journal of The Electrochemical Society*, 136(3):635, 1989. ISSN 00134651.

[36] T. Nakanishi, M. Ozaki, H.-S. Nam, T. Yokoshima, and T. Osaka. Pulsed Electrodeposition of Nanocrystalline CoNiFe Soft Magnetic Thin Films. *Journal of The Electrochemical Society*, 148 (9):C627, 2001. ISSN 00134651.

[37] T. Tsuda, C. L. Hussey, and G. R. Stafford. Electrodeposition of Al-Mo-Mn Ternary Alloys from the Lewis Acidic AlCl[sub 3]-EtMeImCl Molten Salt. *Journal of The Electrochemical Society*, 152(9):C620, 2005. ISSN 00134651.

[38] A. C. Mishra, A. K. Thakur, and V. Srinivas. Effect of deposition parameters on microstructure of electrodeposited nickel thin films. *Journal of Materials Science*, 44(13):3520–3527, apr 2009. ISSN 0022-2461.

[39] J. Yahalom and O. Zadok. Formation of composition-modulated alloys by electrodeposition. *Journal of Materials Science*, 22(2):499–503, 1987. ISSN 00222461.

[40] C. C. Koch, R. O. Scattergood, K. a. Darling, and J. E. Semones. Stabilization of nanocrystalline grain sizes by solute additions. *Journal of Materials Science*, 43(23-24):7264–7272, jul 2008. ISSN 0022-2461.

[41] J. Weissmuller, W. Krauss, T. Haubold, R. Birringer, and H. Gleiter. Atmoic structure and thermal stability of nanostructured Y-Fe alloys. *Nanostructured Materials*, 1:439–447, 1992.

[42] F. Liu, F. Sommer, and E. J. Mittemeijer. Determination of nucleation and growth mechanisms of the crystallization of amorphous alloys; application to calorimetric data. *Acta Materialia*, 52(11):3207–3216, jun 2004. ISSN 13596454.

[43] T. Chookajorn, H. A. Murdoch, and C. A. Schuh. Design of stable nanocrystalline alloys. *Science (New York, N.Y.)*, 337(6097):951–4, aug 2012. ISSN 1095-9203.

[44] H. A. Murdoch and C. A. Schuh. Estimation of grain boundary segregation enthalpy and its role in stable nanocrystalline alloy design. *Journal of Materials Research*, 28(16):2154–2163, aug 2013. ISSN 0884-2914.

[45] B. Grushko and G. Stafford. The effect of Mn content on the microstructure of Al-Mn alloys electrodeposited at 150C. *Israel Journal of Technology*, 24:523–527, 1988. ISSN 00212202.

[46] G. R. Stafford, B. Grushko, and R. D. McMichael. The electrodeposition of Al-Mn ferromagnetic phase from molten salt electrolyte, 1993. ISSN 09258388.

[47] W. Cai and C. A. Schuh. Tuning nanoscale grain size distribution in multilayered AlâMn alloys. *Scripta Materialia*, 66(3-4):194–197, feb 2012. ISSN 13596462.

[48] S. Ruan and C. A. Schuh. Towards electroformed nanostructured aluminum alloys with high strength and ductility. *Journal of Materials Research*, 27(12):1638–1651, apr 2012. ISSN 0884-2914.

[49] W. Simka, D. Puszczyk, and G. Nawrat. Electrodeposition of metals from non-aqueous solutions. *Electrochimica Acta*, 54(23):5307–5319, sep 2009. ISSN 00134686.

[50] T. Jiang, M. J. Chollier Brym, G. Dubé, a. Lasia, and G. M. Brisard. Electrodeposition of aluminium from ionic liquids: Part Iâelectrodeposition and surface morphology of aluminium from aluminium chloride (AlCl3)â1-ethyl-3-methylimidazolium chloride ([EMIm]Cl) ionic liquids. *Surface and Coatings Technology*, 201(1-2):1–9, sep 2006. ISSN 02578972.

[51] F. Endres, M. Bukowski, R. Hempelmann, and H. Natter. Electrodeposition of nanocrystalline metals and alloys from ionic liquids. *Angewandte Chemie (International ed. in English)*, 42(29):3428–30, jul 2003. ISSN 1433-7851.

[52] T. Tsuda and C. L. Hussey. Electrochemical Applications of Room-Temperature Ionic Liquids. *Electrochemical Society Interface*, 2007. ISSN 01730835.

[53] S. Ruan, K. L. Torres, G. B. Thompson, and C. A. Schuh. Gallium-enhanced phase contrast in atom probe tomography of nanocrystalline and amorphous Al-Mn alloys. *Ultramicroscopy*, 111(8):1062–72, jul 2011. ISSN 1879-2723.

[54] M. da Silva, C. Wille, U. Klement, P. Choi, and T. Al-Kassab. Electrodeposited nanocrystalline CoâP alloys: Microstructural characterization and thermal stability. *Materials Science and Engineering: A*, 445-446:31–39, feb 2007. ISSN 09215093.

[55] A. Talin, E. Marquis, S. Goods, J. Kelly, and M. Miller. Thermal stability of NiâMn electrodeposits. *Acta Materialia*, 54(7):1935–1947, apr 2006. ISSN 13596454.

[56] T. H. Hentschel, D. Isheim, and R. Kirchheim. Nanocrystalline Niâ3.6 at.% P and its transformation sequence studied by atom-probe field-ion microscopy. *Acta materialia*, 48:933–941, 2000.

[57] S. C. Mehta, D. A. Smith, and U. Erb. Study of grain growth in electrodeposited nanocrystalline nickel-1.2 wt.% phosphorus alloy. *Materials Science and Engineering A*, 204(1-2):227–232, 1995. ISSN 09215093.

[58] A. El-Sherik, U. Erb, G. Palumbo, and K. T. Aust. Grain growth behaviour of nanocrystalline Nickel. *Mat. Res. Soc. Symp. Proc.*, 238:727–732, 1992.

[59] K. Boylan, D. Ostrander, U. Erb, G. Palumbo, and K. T. Aust. An in-situ TEM study of the thermal stability of nanocrystalline Ni-P. *Scripta metallurgica et materialia*, 25(c):2711–2716, 1991.

[60] H. E. Kissinger. Reaction Kinetics in Differential Thermal Analysis. *Analytical Chemistry*, 29 (11):1702–1706, 1957. ISSN 0003-2700.

[61] H. E. Kissinger. Variation of peak temperature with heating rate in differential thermal analysis. *Journal of Research of the National Bureau of ...*, 57(4):217–221, 1956.

[62] H. A. Murdoch and C. A. Schuh. Stability of binary nanocrystalline alloys against grain growth and phase separation. *Acta Materialia*, 61(6):2121–2132, apr 2013. ISSN 13596454.

[63] S. Ruan and C. A. Schuh. Mesoscale structure and segregation in electrodeposited nanocrystalline alloys. *Scripta Materialia*, 59(11):1218–1221, dec 2008. ISSN 13596462.

[64] E. Chassaing, M. I. Roumegas, and M. F. Trichet. Electrodeposition of N i - M o alloys with pulse reverse potentials. *Journal of Applied Electrochemistry*, 25:667–670, 1995.

[65] J.-Y. Fei and G. D. Wilcox. Electrodeposition of ZnâCo alloys with pulse containing reverse current. *Electrochimica Acta*, 50(13):2693–2698, apr 2005. ISSN 00134686.

[66] A. J. Detor and C. A. Schuh. Tailoring and patterning the grain size of nanocrystalline alloys. *Acta Materialia*, 55(1):371–379, jan 2007. ISSN 13596454.

[67] P. Roura and J. Farjas. Analytical solution for the Kissinger equation. *Journal of Materials Research*, 24(10), 2009.

[68] G. Ruitenberg. Applying Kissinger analysis to the glass transition peak in amorphous metals. *Thermochimica acta*, pages 207–211, 2003.

[69] K. Matusita, T. Komatsu, and R. Yokota. Kinetics of non-isothermal crystallization process and activation energy for crystal growth in amorphous materials. *Journal of Materials Science*, 19(1):291–296, jan 1984. ISSN 0022-2461.

[70] I. M. Lifshitz and V. V. Slyozov. The kinetics of precipitation from supersaturated solid solutions. *Journal of Physics and Chemistry of Solids*, 19(1):35–50, 1961.

[71] M. Avrami. Kinetics of Phase Change. I General Theory. *The Journal of Chemical Physics*, 7(12): 1103, 1939. ISSN 00219606.

[72] M. Avrami. Kinetics of Phase Change. II Transformation-Time Relations for Random Distribution of Nuclei. *The Journal of Chemical Physics*, 8(2):212, 1940. ISSN 00219606.

[73] M. Avrami. Granulation, Phase Change, and Microstructure Kinetics of Phase Change. III. *The Journal of Chemical Physics*, 9(2):177, 1941. ISSN 00219606.

[74] M. Avrami. Geometry and dynamics of populations. *Philosophy of Science*, 8(1):115–132, 1941.

[75] G. Ruitenberg, a. K. Petford-Long, and R. C. Doole. Determination of the isothermal nucleation and growth parameters for the crystallization of thin Ge[sub 2]Sb[sub 2]Te[sub 5] films. *Journal of Applied Physics*, 92(6):3116, 2002. ISSN 00218979.

[76] B. Rheingans and E. J. Mittemeijer. Phase Transformation Kinetics: Advanced Modeling Strategies. *Jom*, 65(9):1145–1154, jul 2013. ISSN 1047-4838.

[77] D. Z. Hu, X. M. Lu, J. S. Zhu, and F. Yan. Study on the crystallization by an electrical resistance measurement in Ge[sub 2]Sb[sub 2]Te[sub 5] and N-doped Ge[sub 2]Sb[sub 2]Te[sub 5] films. *Journal of Applied Physics*, 102(11):113507, 2007. ISSN 00218979.

[78] K. Kelton, T. Croat, A. Gangopadhyay, L.-Q. Xing, A. Greer, M. Weyland, X. Li, and K. Rajan. Mechanisms for nanocrystal formation in metallic glasses. *Journal of Non-Crystalline Solids*, 317(1-2):71–77, mar 2003. ISSN 00223093.

[79] A. L. Greer. Crystallization of metallic glasses. *Materials Science and Engineering: A*, 179-180: 41–45, may 1994. ISSN 09215093.

[80] L. C. Chen and F. Spaepen. Analysis of calorimetric measurements of grain growth. *Journal of applied physics*, 69(January):679–688, 1991. ISSN 00218979.

[81] M. J. Starink. On the meaning of the impingement parameter in kinetic equations for nucleation and. *Journal of Materials Science*, 6(3):4433–4441, 2001.

[82] M. J. Starink and A. M. Zahra. An analysis method for nucleation and growth controlled reactions at constant heating rate. *Thermochimica acta*, 292:159–168, 1997.

[83] M. J. Starink. Kinetic equations for diffusion-controlled precipitation reactions. *Journal of materials science*, 2:4061–4070, 1997.

[84] M. J. Starink and a.-M. M. Zahra. Kinetics of isothermal and non-isothermal precipitation in an Al-6 at.% Si alloy. *Philosophical Magazine A*, 77(1):187–199, jan 1998. ISSN 0141-8610.

[85] A. T. W. Kempen, F. Sommer, and E. J. Mittemeijer. The isothermal and isochronal kinetics of the crystallisation of bulk amorphous Pd40Cu30P20Ni10. *Acta Materialia*, 50(6):1319–1329, 2002. ISSN 13596454.

[86] E. Woldt. The relationship between isothermal and non-isothermal description of Johnson-Mehl-Avrami-Kolmogorov kinetics. *Journal of Physics and Chemistry of Solids*, I, 1992.

[87] M. Starink. Analysis of aluminium based alloys by calorimetry: quantitative analysis of reactions and reaction kinetics. *International Materials Reviews*, 49(3):191–226, jun 2004. ISSN 09506608.

[88] F. Liu, Z. Chen, W. Yang, C. L. Yang, H. F. Wang, and G. C. Yang. Thermodynamics of nanoscale grain growth. *Materials Science and Engineering: A*, 457(1-2):13–17, 2007. ISSN 09215093.

[89] F. Liu, F. Sommer, and E. J. Mittemeijer. An analytical model for isothermal and isochronal transformation kinetics. *Journal of materials science*, 9:1621–1634, 2004.

[90] E. J. Mittemeijer. Analysis of the kinetics of phase transformations. *Journal of Materials science*, 27:3977–3987, 1992.

[91] T.-Y. Huang, C. J. Marvel, P. R. Cantwell, M. P. Harmer, and C. A. Schuh. Grain boundary segregation in AlâMn electrodeposits prepared from ionic liquid. *Journal of Materials Science*, 51(1):438–488, 2016. ISSN 0022-2461.

[92] M. K. Miller and R. G. Forbes. Atom probe tomography. *Materials Characterization*, 60(6): 461–469, jun 2009. ISSN 10445803.

[93] B. Gault, M. P. Moddy, J. M. Cairney, and S. P. Ringer. *Atom Probe Microscopy*. Springer, 2012. ISBN 9781461434351.

[94] D. N. Seidman. Three-Dimensional Atom-Probe Tomography: Advances and Applications. *Annual Review of Materials Research*, 37(1):127–158, aug 2007. ISSN 1531-7331.

[95] P. Choi, M. Dasilva, U. Klement, T. Alkassab, and R. Kirchheim. Thermal stability of electrodeposited nanocrystalline Co-1.1at.%P. *Acta Materialia*, 53(16):4473–4481, sep 2005. ISSN 13596454.

[96] B. Färber, E. Cadel, A. Menand, G. Schmitz, and R. Kirchheim. Phosphorus segregation in nanocrystalline Ni-3.6 at.% P alloy investigated with the tomographic atom probe (TAP). *Acta materialia*, 48:789–796, 2000.

[97] R. Rachbauer, S. Massl, E. Stergar, P. Felfer, and P. H. Mayrhofer. Atom probe specimen preparation and 3D interfacial study of TiâAlâN thin films. *Surface and Coatings Technology*, 204(11):1811–1816, feb 2010. ISSN 02578972.

[98] P. J. Felfer, C. R. Killmore, J. G. Williams, K. R. Carpenter, S. P. Ringer, and J. M. Cairney. A quantitative atom probe study of the Nb excess at prior austenite grain boundaries in a Nb microalloyed strip-cast steel. *Acta Materialia*, 60(13-14):5049–5055, aug 2012. ISSN 13596454.

[99] P. J. Felfer, T. Alam, S. P. Ringer, and J. M. Cairney. A reproducible method for damage-free site-specific preparation of atom probe tips from interfaces. *Microscopy research and technique*, 75(4):484–91, apr 2012. ISSN 1097-0029.

[100] P. J. Felfer, B. Gault, G. Sha, L. Stephenson, S. P. Ringer, and J. M. Cairney. A New Approach to the Determination of Concentration Profiles in Atom Probe Tomography. *Microscopy and Microanalysis*, 18:359–364, 2012. ISSN 1431-9276.

[101] P. Felfer. Atom probe sample preparation using FIB: ref-guide/case studies, 2012.

[102] M. K. Miller and K. F. Russell. Atom probe specimen preparation with a dual beam SEM/FIB miller. *Ultramicroscopy*, 107(9):761–6, oct 2007. ISSN 0304-3991.

[103] M. K. Miller, K. F. Russell, K. Thompson, R. Alvis, and D. J. Larson. Review of atom probe FIB-based specimen preparation methods. *Microscopy and microanalysis : the official journal of Microscopy Society of America, Microbeam Analysis Society, Microscopical Society of Canada*, 13(6): 428–436, dec 2007. ISSN 1431-9276.

[104] G. Cliff and G. W. Lorimer. The quantitative analysis of thing specimens. *Journal of Microscopy*, 103(2):203–207, 1975.

[105] M. Watanabe and D. B. Williams. The quantitative analysis of thin specimens: A review of progress from the Cliff-Lorimer to the new ζ-factor methods. *Journal of Microscopy*, 221(2): 89–109, 2006. ISSN 00222720.

[106] U. Alber, H. Müllejans, and M. Rühle. Improved quantification of grain boundary segregation by EDS in a dedicated STEM. *Ultramicroscopy*, 69:105–116, 1997.

[107] A. J. Detor, M. K. Miller, and C. A. Schuh. Measuring grain-boundary segregation in nanocrystalline alloys: direct validation of statistical techniques using atom probe tomography. *Philosophical Magazine Letters*, 87(8):581–587, aug 2007. ISSN 0950-0839.

[108] A. Mottura, M. K. Miller, and R. C. Reed. Atom probe tomography analysis of possible rhenium clustering in nickel-based superalloys. *Superalloys 2008*, pages 891–900, 2008.

[109] G. Cowan. *Statistical Data Analysis*. Oxford University Press, 1998.

[110] M. Herbig, D. Raabe, Y. J. Li, P. Choi, S. Zaefferer, and S. Goto. Atomic-Scale Quantification of Grain Boundary Segregation in Nanocrystalline Material. *Physical Review Letters*, 112(12): 126103, mar 2014. ISSN 0031-9007.

[111] D. McLean. Grain boundaries in metals, 1957.

[112] J. Trelewicz and C. Schuh. Grain boundary segregation and thermodynamically stable binary nanocrystalline alloys. *Physical Review B*, 79(9):1–13, mar 2009. ISSN 1098-0121.

[113] J. D. Eshelby. The determination of the elastic field of an ellipsoidal inclusion, and related problems. *Proceedings of the Royal Society of physical sciences research journal*, 1957.

[114] J. D. Eshelby. The elastic interaction of point defects. *Acta metallurgica*, 9:487–490, 1955.

[115] J. D. Eshelby. Distortion of a Crystal by Point Imperfections. *Journal of Applied Physics*, 25(2): 255, 1954. ISSN 00218979.

[116] H. Bakker. *Enthalpies in alloys- Miedema's semi-empirical model*. Trans Tech Publications Ltd, 1998.

[117] F. de Boer, R. Boom, W. Mattens, A. Miedema, and A. Niessen. *Cohesion in metals: transition metal alloys*. North Holland, 1988.

[118] A. M. James and M. P. Loard. *Macmillan's Chemical and Physical Data*. Macmillan, London, UK, 1992.

[119] S. Ruan and C. A. Schuh. Kinetic Monte Carlo simulations of nanocrystalline film deposition. *Journal of Applied Physics*, 107(7):073512, 2010. ISSN 00218979.

[120] B. Grushko and G. R. Stafford. A structural study of a metastable phase in Al-Mn alloys electrodeposited from molten salts. *Scripta metallurgica et materialiacripta metallurgica et materialia*, 23(c):557–562, 1989.

[121] B. Grushko and G. R. Stafford. Structural Study of Electrodeposited Aluminum-Manganese Alloys. *Metallurgical Transactions A*, 20(August):1351–1359, 1989.

[122] S. Ruan. *Hard and tough electrodeposited aluminum-manganese alloys with tailored nanostructures*. PhD thesis, Massachusetts Institute and Technology, 2010.

[123] Z. Huang, J. Li, Q. L. Rao, and Y. Zhou. Primary crystallization of AlâNiâRE amorphous alloys with different type and content of RE. *Materials Science and Engineering: A*, 489(1-2): 380–388, aug 2008. ISSN 09215093.

[124] A. Inoue. Amorphous, nanoquasicrystalline and nanocrystalline alloys in Al-based systems. *Progress in Materials Science*, 43(5):365–520, dec 1998. ISSN 00796425.

[125] U. Koster and U. Herold. *Glassy Metals I*. Springer Berlin Heidelberg, 1981. ISBN 978-3-540-10440-7.

[126] P. G. Boswell. Crystallisation of A (Ni5Pd5)82P18 amorphous alloy. *Scripta Metallurgica*, 11: 701–707, 1977.

[127] H. Schmidt, W. Gruber, G. Borchardt, M. Bruns, M. Rudolphi, and H. Baumann. Thermal stability and crystallization kinetics of sputtered amorphous Si3N4 films. *Thin Solid Films*, 450(2):346–351, 2004. ISSN 00406090.

[128] G. Herzer, B. Idzikowski, P. Svec, and M. Miglierini. Properties and applications of nanocrystalline alloys from amorphous precursors. *NATO Science Series*, 2005.

[129] A. Inoue, H. Kimura, and T. Masumoto. Formation, thermal stability and electrical resistivity of quasicrystalline phase in rapidly quenched Al-Cr alloys. *Journal of Materials Science*, 22(5): 1758–1768, 1987. ISSN 00222461.

[130] K. V. Rao, J. Fidler, and H. S. Chen. Melt-Spun Al84V16: A New Icosahedral Crystal. *Europhysics Letters*, 1(12):647–653, 1986.

[131] A. Inoue, L. Arnberg, B. Lehtinen, M. Oguchi, and T. Masumoto. Compositional Analysis of the Icosahedral Phase in Rapidly Quenched Al-Mn and Al-V Alloys. *Metallurgical Transactions A*, 17(October):1657–1664, 1986.

[132] A.-P. Tsai, A. Inoue, and T. Masumoto. A Stable Quasicrystal in Al-Cu-Fe System. *Japanese Journal of Applied Physics*, 26(Part 2, No. 9):L1505—-L1507, 1987. ISSN 0021-4922.

[133] A. P. Tsai, A. Inoues, Y. Yokoyama, and T. Masumoto. New icosahedral alloys with superlattice order in the AlâPdâMn system prepared by rapid solidification. *Philosophical Magazine Letters*, 61(1):9–14, 1990. ISSN 0950-0839.

[134] N. K. Mukhopadhyay, G. C. Weatherly, D. J. Lloyd, and J. D. Embury. Diffraction studies of icosahedral phases in the Al - Fe - W system. *Journal of Non-Crystalline solids*, 154:63–67, 1993.

[135] T. Wilson, J. Bai, and H. Choo. Enhanced thermal stability of amorphous aluminum alloys through microalloying. *Materials Letters*, 62(23):3790–3792, 2008. ISSN 0167577X.

[136] H. P. Longworth and C. V. Thompson. Abnormal grain growth in aluminum alloy thin films. *Journal of Applied Physics*, 69(7):3929, 1991. ISSN 00218979.

[137] F. Zhou, X. Z. Liao, Y. T. Zhu, S. Dallek, and E. J. Lavernia. Microstructural evolution during recovery and recrystallization of a nanocrystalline Al-Mg alloy prepared by cryogenic ball milling. *Acta Materialia*, 51(10):2777–2791, 2003. ISSN 13596454.

[138] M. Jin, A. M. Minor, E. A. Stach, and J. W. Morris. Direct observation of deformation-induced grain growth during the nanoindentation of ultrafine-grained Al at room temperature. *Acta Materialia*, 52(18):5381–5387, 2004. ISSN 13596454.

[139] C. Zhang, Y. Wu, X. Cai, and G. Zhou. Precipitation of an icosahedral phase in amorphous Al90Fe5Ce5 alloy. *Journal of Physics*, 647, 2001.

[140] J. C. Holzer and K. F. Kelton. Kinetics of the amorphous to icosahedral phase transformation in Al-Cu-V alloys. *Acta Metallurgica materilia*, 39(8):1833–1843, 1991.

[141] A. P. Tsai, A. Inoue, Y. Bizen, T. Masumoto, A. P. Tsai, A. Inoue, Y. Bizen, and T. Masumoto. Kinetics of the amorphous to icosahedral structure transition in Al-Cu-V and Al-Mn-Si alloys. *Acta Metallurgica*, 37(5):1443–1449, may 1989. ISSN 00016160.

[142] J. L. Robertson, S. C. Moss, and K. G. Kreider. Comparison of amorphous and quasicrystalline films of sputtered Al0.72Mn0.22Si0.06. *Physical review letters*, 60(20):2062–2065, 1988.

[143] A. Inoue, Y. Bizen, and T. Masumoto. Quasicrystalline phase in Al-Si-Mn system prepared by annealing of amorphous phase. *Metallurgical Transactions A*, 19(2):383–385, 1988. ISSN 03602133.

[144] M. J. Kaufman, F. S. Biancaniello, and K. G. Kreider. The annealing behavior of sputter-deposited AlâMn and AlâMnâSi films. *Journal of Materials Research...*, 3(6):1342–1348, 1988.

[145] D. M. Follstaedt and J. A. Knapp. Icosahedral-Phase Formation by Solid-State Interdiffusion. *Physical review letters*, 56(17), 1986.

[146] R. J. Schaefer, L. A. Bendersky, D. Shechtman, W. J. Boettinger, and F. S. Biancaniello. Icosahedral and decagonal phase formation in Al-Mn alloys. *Metallurgical Transactions A*, 17(12): 2117–2125, 1986. ISSN 0360-2133.

[147] D. A. Lilienfeld, M. Nastasi, H. H. Johnson, D. G. Ast, and J. W. Mayer. Amorphous to Quasicrystalline Transformation in the Solid State. *Physical Review Letters*, 1, 1985.

[148] P. B. Barna, A. Csanády, G. Radnoczi, K. Urban, and U. Timmer. Quasi-crystalline structure formation in thin films. *Thin Solid Films*, 193-194(PART 1):1–12, 1990. ISSN 00406090.

[149] B. Grushko and G. R. Stafford. Formation of the Al-Mn icosahedral phase by electrodeposition. *Scripta Metallurgica et Materialia*, 23(c):1043–1048, 1989.

[150] L. A. Bendersky and S. D. Ridder. Nucleation behavior of Al-Mn icosahedral phase. *Journal of Materials Research*, 20899(February):405–414, 1986.

[151] J. A. Knapp and D. M. Follstaedt. Formation of Icosahedral Al(Mn) by Directed Energy Processes. *Physical review letters*, 55(15):1591–1595, 1985.

[152] L. C. Chen and F. Spaepen. Calorimetric evidence for the micro-quasicrystalline structure of 'amorphous' Al/transition metal alloys. *Nature*, 336(24):366–369, 1988.

[153] R. Popescu, P. B. Barna, M. Constantin, a. Devenyi, and R. Manaila. Icosahedral AlâMn phases grown in diffusion-limited conditions. *Thin Solid Films*, 360(1-2):46–51, feb 2000. ISSN 00406090.

[154] D. Gupta, K. N. Tu, and K. W. Asai. Diffusion in the amorphous phase of Pd-19-at.{%}-Si metallic alloy. *Physical Review Letters*, 35(12):796–799, 1975. ISSN 00319007.